



Title	Development of Nano-scale Direct Observation Method for Hydrogel Network Structure and Study on Fracture Mechanism of Hydrogel
Author(s)	木山, 竜二
Citation	北海道大学. 博士(生命科学) 甲第14825号
Issue Date	2022-03-24
DOI	10.14943/doctoral.k14825
Doc URL	<a href="http://hdl.handle.net/2115/89183">http://hdl.handle.net/2115/89183</a>
Type	theses (doctoral)
File Information	Ryuji_Kiyama.pdf



[Instructions for use](#)

**Doctoral Dissertation**

**Development of Nano-scale Direct Observation Method for  
Hydrogel Network Structure and  
Study on Fracture Mechanism of Hydrogel**

(ハイドロゲル網目直接観察法の開発及び  
ハイドロゲル破壊メカニズム究明に関する研究)

*By*

***Ryuji Kiyama***

Supervisor: Jian Ping Gong



Laboratory of Soft & Wet Matter,

Graduate School of Life Science, Hokkaido University

Sapporo 001-0021, Japan

2022, March

# Contents

<b>CHAPTER 1</b> .....	<b>6</b>
General introduction	
1.1 Overview.....	6
1.2 Outline of this dissertation .....	7
1.3 References.....	10
<b>CHAPTER 2</b> .....	<b>13</b>
Background	
2.1 Hydrogel structure measurement methods .....	13
2.2 Fracture mechanics of hydrogel .....	17
2.3 References .....	19
<b>CHAPTER 3</b> .....	<b>22</b>
Micro Patterning of Hydroxyapatite on Hydrogels for Selective Osteoconduction	
3.1 Introduction.....	22
3.2 Experiments .....	25
3.2.1 Materials.....	25
3.2.2 Gel synthesis.....	26
3.2.3 HAp mineralization .....	27
3.2.4 Acid gel stamping .....	27
3.2.5 Ultraviolet-visible absorption spectroscopy (UV-Vis).....	28
3.2.6 Microindentation .....	28
3.2.7 Transmittance electron microscopic (TEM) observation .....	29
3.2.8 X-ray diffraction (XRD).....	29
3.2.9 Contact angle of water .....	29
3.2.10 Fourier transform infrared spectroscopy (FT-IR) .....	30

3.2.11 Scanning electron microscopy and energy dispersive X-ray spectroscopy (SEM-EDX) .....	30
3.2.12 3D laser microscope .....	30
3.2.13 Cell culture on HAp/DN gels .....	31
3.2.14 Animals .....	32
3.2.15 90° peeling test of HAp-patterned DN gel sheet bonded to bone .....	32
3.2.16 Demonstration of selective bonding to bone <i>in vivo</i> .....	33
3.2.17 Statistical Analysis .....	34
3.3 Results & Discussion.....	34
3.3.1 Micro patterning of hydroxyapatite by soft lithography on hydrogels	34
3.3.2 <i>In vitro</i> cell culture test .....	39
3.3.3 <i>In vivo</i> osteoconduction test .....	41
3.4 Conclusion .....	45
3.5 References.....	46
<b>CHAPTER 4 .....</b>	<b>49</b>
Nano Scale Direct Imaging of a Rubber Elastic Hydrogel Network	
4.1 Introduction.....	49
4.2 Experiments .....	50
4.2.1 Materials.....	50
4.2.2 Network sample synthesis .....	51
4.2.3 Average mesh size estimation .....	52
4.2.4 Mineral staining and transmission electron microscopy observation	53
4.2.5 Data analysis .....	55
4.3 Results & Discussion.....	56
4.3.1 Strategy to Prepare TEM Samples of Network Polymers .....	56
4.3.2 Nanoscale TEM observation of the network .....	59

4.3.3 Surface structure of network .....	66
4.3.4 Heterogeneity of the network .....	70
4.4 Conclusion .....	72
4.5 References.....	72
<b>CHAPTER 5 .....</b>	<b>76</b>
Fractographic Analysis on Non-linear Elastic Hydrogels	
5.1 Introduction.....	76
5.2 Experiments .....	78
5.2.1 Materials.....	78
5.2.2 Gel synthesis.....	79
5.2.3 Tensile test.....	80
5.2.4 Roughness observation by 3D laser microscope .....	81
5.2.5 Roughness observation by transmission electron microscopy (TEM)...	81
5.3 Results & Discussion.....	82
5.3.1 Mirror region formed by crack branching .....	82
5.3.2 Relationship between mirror radius and fracture stress .....	85
5.4 Conclusion .....	91
5.5 References.....	91
<b>CHAPTER 6 .....</b>	<b>94</b>
Fracture mechanism of pure elastic gel	
6.1 Introduction.....	94
6.2 Experiments .....	95
6.2.1 Materials.....	96
6.2.2 Gel synthesis.....	96
6.2.3 Tensile test.....	96

6.2.4 Roughness observation by transmission electron microscopy (TEM) .	97
6.2.5 Roughness observation by 3D laser microscopy .....	98
6.2.6 Roughness observation by atomic force microscopy (AFM) .....	98
6.2.7 Power spectrum density (PSD) analysis .....	99
6.3 Results & Discussion.....	100
6.3.1 Inter-microgel fracture of pure elastic gel .....	100
6.3.2 Microscale fracture mechanism of pure elastic gel .....	108
6.4 Conclusion .....	112
6.5 References.....	113
<b>CHAPTER 7 .....</b>	<b>115</b>
Summary of dissertation .....	115
7.1 Original papers.....	117
7.2 Other papers.....	118
7.3 Presentation in scientific meetings .....	121
<b>Acknowledgement .....</b>	<b>126</b>

# CHAPTER 1

## General Introduction

### 1.1 Overview

Hydrogels are widely using soft materials, such as food, cell culture substrate, artificial biomaterials, and wearable device.<sup>[1-6]</sup> Their attractive nature, flexibility and reversibility, comes from entropic elasticity from polymer network thermal motion. However, state-of-the-art understanding about network structure are still limited at the average structure level derived from bulk measurements.<sup>[7]</sup> Polymer science has not reached to completely link physical property with structure. There are still several unsolved problems especially with the local structure like chain distribution and surface morphology. The main limitation is lack of suitable method to directly observe nano scale network structure. Despite of many challenges, it has not been achieved to capture individual polymer chain by microscopy from among polymers fluctuated by Brownian motion.

Because of such situation, the fracture mechanism of hydrogel is also not well understood. Since gel research ignores how gel breaks on a microscale, it is very difficult to understand the origin of the toughness of the gel. This problem also exist with some strong gels developed in recent years.<sup>[8-10]</sup> On the other hand, the fracture mechanism of hard materials such as metals and ceramics has been clarified in detail, through the direct observation results of the fracture surface feature.<sup>[11]</sup> Therefore, to establish true fracture mechanics of hydrogel via direct observation is promising way to understand and to

design tough hydrogels.

As described above, there are two main goals in this dissertation. 1) To develop the novel direct observation method for nanoscale hydrogel network structure. 2) To elucidate fracture mechanism of hydrogel. This dissertation comprises seven chapters including this general introduction as **Chapter 1**.

## **1.2 Outline of this dissertation**

A general background of conventional hydrogel observation method and conventional knowledge about hydrogel fracture has been discussed **in Chapter 2**. Also I explain major difficulties on observing nanoscale structure of hydrogel.

**In Chapter 3**, we report a novel lithography technique to make mineral nanoparticle patterned hydrogel.<sup>[12]</sup> This work gave a big hint for developing the hydrogel network direct observation method **in Chapter 4**. In this study, we selectively patterned osteoconductive Hydroxyapatite (HAp) mineral nano particle on the Double Network (DN) hydrogel surface. This kind mechanically tough hydrogels are a promising biomaterial as artificial soft tissue such as cartilage, tendon and ligament. However, their practical application in human body has been limited, because of high water content and low friction nature of hydrogel makes difficult to fix in the body. Thus, hybridization with osteoconductive HAp, which induces spontaneous bonding with bone in the body, is promising way.<sup>[13-15]</sup> First, we



mineralized HAp at DN gel surface by using alternative dipping method. After that, we selectively dissolve HAp with acidic gel stamp. As the result, we achieved simple and fast HAp patterning on DN gel surface. Furthermore, we confirmed selective bone bonding at HAp coated area in the living body. In addition, during this study, it was confirmed that HAp inorganic crystals were not uniformly precipitated inside the gel, but that there were some HAp non-exist area. This result suggest that mineral particles selectively mineralized on the hydrogel network.

**In Chapter 4**, we report the novel nanoscale direct observation method for hydrogel networks by applying inhomogeneous mineralization of inorganic nano-particles on the gel network, as suggested by **Chapter 3**. HAp forms a huge polycrystals of several hundred nm, which is not suitable for observing a gel network mesh with size of several tens of nm. Therefore, we decided to use iron oxide that forms nanoparticles with a size of several nm. We select polyelectrolyte gel having sulfonic acid groups as observation target, because they can act as nucleation point and induce selective iron oxide mineralization on the polymer network. Since iron oxide nanoparticles have a sufficiently high electron density, the mineral composite gel network can be observed with a transmission electron microscope (TEM). In addition, the problem of inter-polymer agglomeration during mineral precipitation process was solved by introducing a neutral gel network that does not interact with the mineral. Physical entanglement with neutral network can keep the unperturbed structure of polyelectrolyte gel network.<sup>[16]</sup> The observed nanoscale gel network structure was well agreed with

the network structure predicted from rubber elastic theory. We also checked that distribution of sulfur element (from target gel network) and iron element (from iron oxide nanoparticle) were overlapped by STEM elemental mapping. This result proved hydrogel network structure was successfully stained by iron oxide particles. Furthermore, using this method, we observed various phenomena in which the local structure has an important role (e.g. surface dangling chain, internal voids, gel interface, gel fracture surface).

**In Chapter 5**, we focused on the fracture of hydrogel among the phenomena observed **in Chapter 4**. Brittle fracture is a fracture processes in which a material has almost no plasticity or viscosity and fracture starts instantly from a small initial crack. It is known that the brittle fracture surface has a two characteristic feature: 1) Circular smooth region (mirror surface) starting from the initial crack and 2) uneven region (hackle surface) around smooth region. For hard brittle materials such as glass, it has been reported that there is a correlation between the size of this mirror surface and the fracture stress. In this chapter, by using the hydrogel direct observation method described **in Chapter 4**, it was confirmed that brittle hydrogel also forms mirror-hackle area, but that hydrogel shows different mirror size-fracture stress correlation compared with glass.

**In Chapter 6**, we attempted to clarify the crack propagate mechanism in hydrogels on micro scale by using a pure elastic gel without viscous component. It is known that when the brittle materials (e.g. ceramics and thermosetting plastics) fracture, cracks propagate on the weakest path in the

material on a microscale. Unfortunately, no studies have been conducted on hydrogels to investigate how cracks grow on a microscale. In this study, we clarified how crack proceed in the hydrogel by combining various observation methods. As the result, we confirmed the inter-microgel fracture is the fracture mechanism for pure elastic gel. Furthermore, by calculating the Hurst index, which represents fractal property of fracture surface roughness, it was suggested that the crosslink density dominated the fracture mechanism on a microscale.

**In Chapter 7**, concluding remarks of these works are summarized.

### 1.3 References

- [1] O. Erol, A. Pantula, W. Liu, D. H. Gracias, *Adv. Mater. Technol.* **2019**, *4*, 1.
- [2] J. P. Gong, *Soft Matter* **2006**, *2*, 544.
- [3] R. A. Green, S. Baek, L. A. Poole-Warren, P. J. Martens, *Sci. Technol. Adv. Mater.* **2010**, *11*, DOI 10.1088/1468-6996/11/1/014107.
- [4] A. S. Hoffman, *Adv. Drug Deliv. Rev.* **2012**, *64*, 18.
- [5] K. Y. Lee, D. J. Mooney, *Chem. Rev.* **2001**, *101*, 1869.
- [6] K. Yasuda, N. Kitamura, J. P. Gong, K. Arakaki, H. J. Kwon, S. Onodera, Y. M. Chen, T. Kurokawa, F. Kanaya, Y. Ohmiya, Y. Osada, *Macromol. Biosci.* **2009**, *9*, 307.

- [7] K. Fukao, T. Nakajima, T. Nonoyama, T. Kurokawa, T. Kawai, J. P. Gong, *Macromolecules* **2020**, *53*, 1154.
- [8] J. P. Gong, *Soft Matter* **2010**, *6*, 2583.
- [9] J. Gong, Y. Katsuyama, T. Kurokawa, Y. Osada, *Adv. Mater.* **2003**, *15*, 1155.
- [10] T. Sakai, T. Matsunaga, Y. Yamamoto, C. Ito, R. Yoshida, S. Suzuki, N. Sasaki, M. Shibayama, U. Chung, *Macromolecules* **2008**, *41*, 5379.
- [11] T. L. Anderson, *Fracture Mechanics, Third Edition Fundamentals and Applications*, Taylor&Francis Group, LLC., **2005**.
- [12] R. Kiyama, T. Nonoyama, S. Wada, S. Semba, N. Kitamura, T. Nakajima, T. Kurokawa, K. Yasuda, S. Tanaka, J. P. Gong, *Acta Biomater.* **2018**, *81*, 60.
- [13] T. Nonoyama, S. Wada, R. Kiyama, N. Kitamura, M. T. I. Mredha, X. Zhang, T. Kurokawa, T. Nakajima, Y. Takagi, K. Yasuda, J. P. Gong, *Adv. Mater.* **2016**, *28*, 6740.
- [14] T. Nonoyama, L. Wang, M. Tsuda, Y. Suzuki, R. Kiyama, K. Yasuda, S. Tanaka, K. Nagata, R. Fujita, N. Sakamoto, N. Kawasaki, H. Yurimoto, J. P. Gong, *Adv. Healthc. Mater.* **2021**, *10*, 1.
- [15] S. Wada, N. Kitamura, T. Nonoyama, R. Kiyama, T. Kurokawa, J. P. Gong, K. Yasuda, *Acta Biomater.* **2016**, *44*, 125.
- [16] T. Nakajima, T. Nakajima, T. Nakajima, T. Chida, K. Mito, T. Kurokawa, T. Kurokawa, J. P.

Gong, J. P. Gong, J. P. Gong, *Soft Matter* **2020**, *16*, 5487.

## CHAPTER 2

### Background

#### 2.1 Hydrogel structure measurement methods

Hydrogel structure measurement methods describing in this section includes both scattering methods and direct observation methods. Each methods has its own strengths and weaknesses. I will outline below how each method applied to gel observation.

- **Scattering method**

The scattering methods are most commonly used method for structural analysis of hydrogels.<sup>[1-</sup>

<sup>5]</sup> By irradiating the sample with visible light, X-ray, and neutron, the scattered signal is obtained on the detector. The change in intensity of the signal with respect to the angle reflects the internal structure of the sample. By changing irradiating species, it can observe the structure of Å to mm. In addition, since both liquid and bulk solid can be observed in real time, scattering methods are used not only for static gel structural analysis but also for dynamic gel synthesis and deformation process analysis. The only weakness of the scattering methods is that they can only obtain the average information of a wide sample area but not obtain local information such as, internal defect, chain length distribution and so on.

- **Optical microscopy (OM)**

The method using visible light is one of the simplest structural observation methods. However,

Optical microscopy has a low resolution of 0.2  $\mu\text{m}$ , so it cannot be used for observing the network structure of gels, which consisted from  $\text{\AA}$  to nm diameter thin chains. As an exception, physical gels formed by aggregated structure such as biopolymer gels and PNIPAAm gel have been observed by dyeing with fluorescent microscopy or confocal microscopy.<sup>[6,7]</sup> Basically, it can't use for common chemical gels like PAAm gel, PAMPS gel, DN gel, etc.

- **Atomic force microscopy (AFM)**

Unlike other measurement methods, the atomic force microscopy scans the sample surface with a fine probe and measures the surface morphology from probe strain.<sup>[8]</sup> This technique provides atomic-level resolution for hard materials such as metals, ceramics and plastics. In addition, it can be measured in various environments such as in the air or in solvents, so AFM is sometimes used to observe hydrogel structure. However, it is not common to use AFM for hydrogels due to two major limitations. 1) AFM can only observe the surface of the material. Since hydrogel is a three-dimensional network material, this limitation greatly narrows the observation target. 2) AFM cannot measure soft materials. Hydrogel's polymer network, which is constantly fluctuating due to Brownian motion, rarely exhibits the hardness enough to distort the AFM probe. Therefore, only some special hard phase-separated gels can be observed with AFM.<sup>[9-11]</sup>

- **Electron microscopy (SEM and TEM)**

Despite being the most widely used for hydrogel, electron microscopy is a measurement method

that has created many misunderstandings. Electron microscopy can be classified into scanning electron microscopy (SEM) and transmission electron microscopy (TEM). SEM scans the surface of the sample with an electron beam and observes the reflected electrons. TEM irradiates electron beam to sample and measures the intensity of transmitted electrons, which depend on the electron density in the sample.<sup>[12-16]</sup> Both methods use electron beam that is easily scattered by air, so measurements must be performed under vacuum condition. Especially in the case of hydrogel, drying process to remove water is necessary, but the structure change at that time often creates artifacts on the electron microscopy image. Therefore, except for some special physical gels whose structure is stable against drying, no studies have observed the unperturbed structure of common chemical hydrogels by electron microscopy.<sup>[17]</sup> Many papers include the results of SEM observations of chemical gel network, but be aware that in most cases they are erroneously observing artifacts.



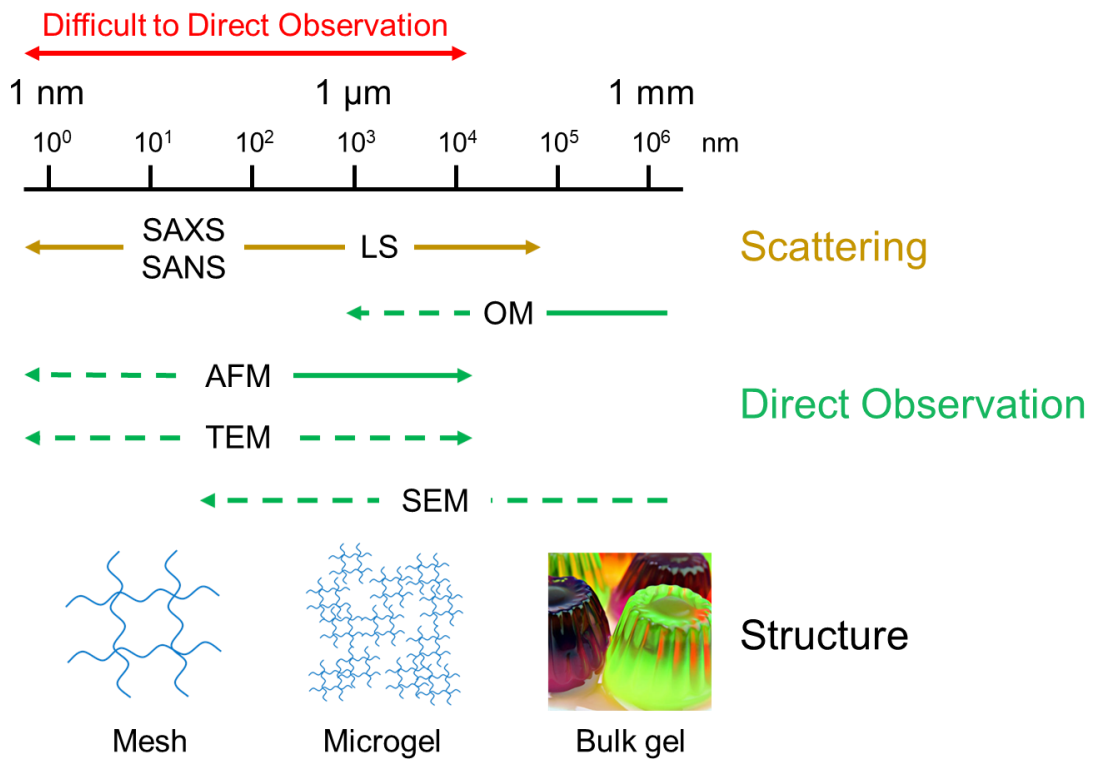


**Figure 2.1** Conventional hydrogel structure measurement methods. The solid lines represent the observable area for any gels. Dotted lines represent observable areas on some special phase-separated gels.

I summarized common hydrogel structure measurement methods and their observation region (**Figure 2.1**). Each method have specific strong point, but unfortunately nm to μm direct observation of soft chemical gels remains as the last challenge.

## 2.2 Fracture mechanics of hydrogel

To understand fracture mechanics is essential to build a strong building. Therefore, there are long history about fracture study.<sup>[18-21]</sup> It is said that Leonardo da Vinci was also interested in the fracture of materials. The study of modern fracture mechanics began in 1920 by Griffith's paper. Griffith found that a simple equilibrium between the released strain energy and the newly generated surface energy can explain whether fracture occurs or not. His model successfully explained the relationship between fracture stress and sample size for the glass. Fracture mechanics, which initially applied only with completely brittle elastic materials, gradually expanded its scope to ductile materials such as metals and plastics. However, little research has been done on hydrogels because of its unique problem, extremely low modulus. As mentioned in the previous section, there has never been observation method for the local structure of  $\mu\text{m}$  from  $\text{nm}$  in soft chemical gels. As a result, many hydrogel researchers ignore the details of the fracture process. Recently, J. Finberg group have been conducting some advanced research, but most of them are related to  $\text{mm}$ -scale crack branching or crack velocity and so on<sup>[22-24]</sup>. We lack the research that link the  $\text{nm}$  to  $\mu\text{m}$  structures with fracture mechanics. For example, in ceramics, fracture are classified into some types (inter-crystal fracture, cleavage fracture, ductile fracture, etc.) depending on how the material breaks on microscale, and their detailed mechanism were investigated. While the fracture mechanics of metals and ceramics had made great progress by direct observation by TEM, research on hydrogels has been delayed significantly.

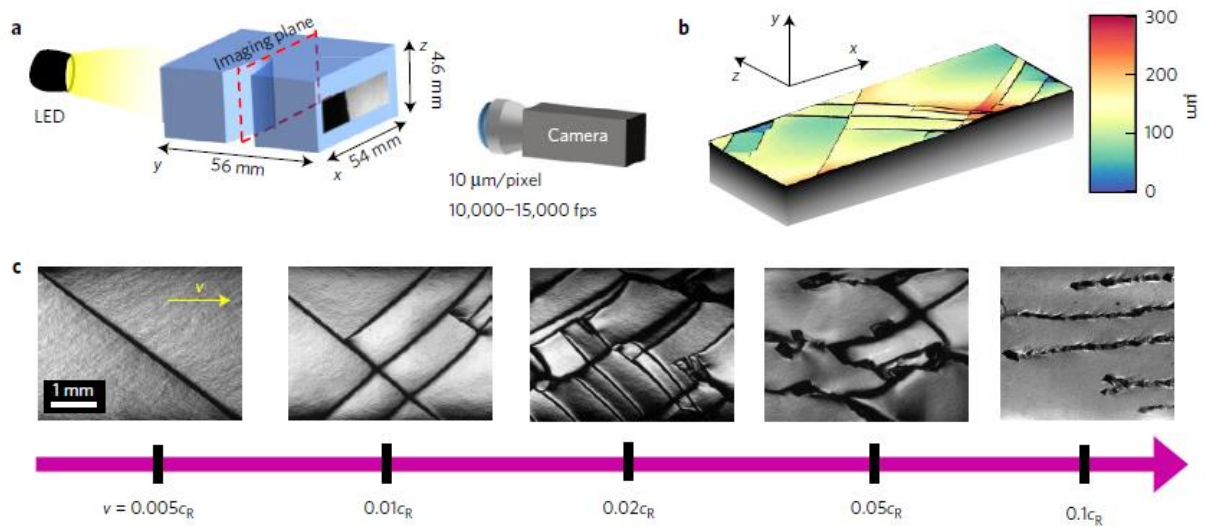


**Figure 2.2** Fracture surface observation of highly crosslinked PAAm.<sup>[25]</sup> Crack branching behavior changes with fracture velocity.

In fact, some study have been shown that microscale fracture mechanisms are also important in the hydrogel. The Fig 2.2 is the fracture surface of PAAm gel with different velocity.<sup>[25]</sup> In this study researchers focuses on millimeter-sized crack branching, but we can clearly see the roughness of the  $\mu\text{m}$  scale on the fracture surface at low velocity ( $v = 0.005c_R$ ). However, since there is no method to observe the fine structure, detailed research on how this kind of structure formed during fracture has not been conducted. Therefore, there is a need to develop a nanoscale direct observation method for the construction of “true” gel fracture mechanics.

## 2.3 References

- [1] H. Furukawa, K. Horie, *Phys. Rev. E* **2003**, *68*, 1.
- [2] K. Fukao, T. Nakajima, T. Nonoyama, T. Kurokawa, T. Kawai, J. P. Gong, *Macromolecules* **2020**, *53*, 1154.
- [3] T. Tominaga, V. R. Tirumala, E. K. Lin, J. Ping, H. Furukawa, Y. Osada, W. Wu, *Polymer (Guildf)*. **2007**, *48*, 7449.
- [4] M. Shibayama, A. M. Shibayama, T. Norisuye, *Bull. Chem. Soc. Jpn* **2002**, *75*, 641.
- [5] M. Shibayama, *Bull. Chem. Soc. Jpn*. **2006**, *79*, 1799.
- [6] Y. Hirokawa, H. Jinnai, Y. Nishikawa, T. Okamoto, T. Hashimoto, *Macromolecules* **1999**, *32*, 7093.
- [7] S. Onogi, H. Shigemitsu, T. Yoshii, T. Tanida, M. Ikeda, R. Kubota, I. Hamachi, *Nat. Chem.* **2016**, *8*, 743.
- [8] A. C. Anderson, M. E. Malinowski, P. Rev, E. J. Cotts, D. M. Miliotis, G. A. Northrop, G. A. Kneezel, A. V Granato, P. B. Bev, G. Binning, H. Rohrer, C. Gerber, E. Weibel, *Phys. Rev* **1975**, *49*, 6196.
- [9] A. Suzuki, M. Yamazaki, Y. Kobiki, H. Suzuki, *Macromolecules* **1997**, *30*, 2350.
- [10] J. Wiedemair, M. J. Serpe, J. Kim, J. F. Masson, L. A. Lyon, B. Mizaikoff, C. Kranz, *Langmuir* **2007**, *23*, 130.

- [11] M. Iijima, M. Shinozaki, T. Hatakeyama, M. Takahashi, H. Hatakeyama, *Carbohydr. Polym.* **2007**, *68*, 701.
- [12] M. Tosaka, R. Danev, K. Nagayama, *Macromolecules* **2005**, *38*, 7884.
- [13] H. Jinnai, R. J. Spontak, T. Nishi, *Macromolecules* **2010**, *43*, 1675.
- [14] N. A. Ranson, P. G. Stockley, *Emerg. Top. Phys. Virol.* **2010**, 1.
- [15] R. Aso, H. Kurata, T. Namikoshi, T. Hashimoto, S. W. Kuo, F. C. Chang, H. Hasegawa, M. Tsujimoto, M. Takano, S. Isoda, *Macromolecules* **2013**, *46*, 8589.
- [16] H. Jinnai, R. J. Spontak, *Polymer (Guildf)*. **2009**, *50*, 1067.
- [17] F. Gentile, M. Moretti, T. Limongi, A. Falqui, G. Bertoni, A. Scarpellini, S. Santoriello, L. Maragliano, R. P. Zaccaria, E. Fabrizio, **2012**, 10.
- [18] R. Danzer, T. Lube, P. Supancic, R. Damani, *Adv. Eng. Mater.* **2008**, *10*, 275.
- [19] P. Du, B. Xue, Y. Song, S. Lu, J. Yu, Q. Zheng, *Polym. Bull.* **2010**, *64*, 185.
- [20] J. Fineberg, E. Bouchbinder, *Int. J. Fract.* **2015**, *196*, 33.
- [21] T. L. Anderson, *Fracture Mechanics, Third Edition Fundamentals and Applications*, Taylor&Francis Group, LLC., **2005**.
- [22] T. Goldman, A. Livne, J. Fineberg, *Phys. Rev. Lett.* **2010**, *104*, 5.
- [23] I. Kolvin, J. M. Kolinski, J. P. Gong, J. Fineberg, *Phys. Rev. Lett.* **2018**, *121*, 135501.
- [24] E. Bouchbinder, T. Goldman, J. Fineberg, *Reports Prog. Phys.* **2014**, *77*, DOI 10.1088/0034-

4885/77/4/046501.

[25] I. Kolvin, G. Cohen, J. Fineberg, *Nat. Mater.* **2018**, *17*, 140.

## CHAPTER 3

### Micro Patterning of Hydroxyapatite on Hydrogels for Selective Osteoconduction<sup>[1]</sup>

#### 3.1 Introduction

Hydrogel is a material containing a large amount of water inside its polymer network. Because of its similarities to living tissue including high-water content, flexibility, softness, and permeability, hydrogels are promising biomaterials for next-generation soft scaffolds and artificial soft tissues <sup>[2-5]</sup>. In particular, mechanically robust hydrogels invented in the 2000s overcome the limitations of weak and brittle conventional hydrogels, and provide the potential for use as artificial load-bearing supportive tissue such as cartilage, tendon, and ligament <sup>[6-9]</sup>. For example, double network (DN) gels show low friction, high mechanical strength, and toughness similar to natural cartilage, and have been intensively studied as artificial cartilage and meniscus tissue <sup>[10-12]</sup>. In addition, recently, because the DN hydrogel can induce *in vivo* cartilage regeneration <sup>[13]</sup>, the DN gel has been applied to develop a special sheet-type implant, which is implanted at the bottom of an osteochondral defect in the joint to induce spontaneous cartilage regeneration. Hydrogel research provides a novel remedy for cartilage disease treatment <sup>[13-15]</sup>. However, one of the greatest problems for the clinical application of the DN gels is that hydrogels contain an abundant amount of water and are usually non-adhesive to the bone tissue, and the artificial cartilage and meniscus can function in the joint only if it is rigidly bonded to the anatomical positions on the femur or tibia.

Calcium-phosphate-hydroxide salt hydroxyapatite (HAp) is the main inorganic component of bone and teeth, and possesses osteoconductivity and good cell adhesive properties<sup>[16]</sup>. To solve the above-described problem, we previously reported a method of fixing tough DN hydrogels to bones *in vivo* by mineralizing HAp nanoparticles in the surface layer of the hydrogels<sup>[14,15,17]</sup>. In this immobilization method, osteoconduction was induced by HAp in the hydrogel surface, and a strong bond between the gel and bone was achieved by forming a gradient structure in which bone tissue penetrates into the interior of the gel surface layer. As a result, the adhesive strength of the gel to the bone exceeded that of previous bone and metal/ceramics bonding<sup>[14,18-21]</sup>.

HAp nanoparticles, having low crystallinity, were mineralized in hydrogels by the alternative dipping method in precursor solution in an ambient environment<sup>[22]</sup>. This method gives a uniform HAp nanoparticle layer on the surface of a DN hydrogel with controlled thickness and HAp particle density. The HAp-mineralized DN gel changed from a bio-inert surface to osteoconductive while its softness and flexibility were well maintained. For practical medical use, tailor-made bone bonding is required for complicated defect shapes and individual differences. In this chapter, we aimed to develop a general method to fabricate a patterned HAp layer on the hydrogel surface for selective bonding to bones. Our strategy was first hybridizing a uniform HAp nanoparticle layer on the surface of a DN hydrogel via the alternative dipping method and then fabricating a pre-designed HAp pattern on the HAp layer by using soft lithography.



Soft lithography is a simple and low cost lithographic technique using an elastic stamp as a patterning structure instead of photolithography<sup>[23]</sup>. Hydrogels are non-fluidic solids that possess solution properties such as diffusion, evaporation, and acidity/basicity. Owing to these properties, hydrogels have been used as stamps in soft lithography<sup>[24-26]</sup>. Herein, we etched the mineralized HAp nanoparticles inside the semipermeable DN hydrogel using the soft lithography technique (**Fig. 3.1A**). Since HAp is easily dissolved in an acidic environment<sup>[27]</sup>, we used a gel stamp containing acidic small molecules. Owing to the semi-permeable character of the gel, the acid molecules in the gel stamp diffuse into the substrate DN gel to dissolve the HAp nanoparticles in the surface layer of the gel. As a result, we obtained a HAp pattern that is controlled by the contact pattern of the gel stamp. This is the first study to apply the soft lithography technique for in depth etching of semi-permeable hydrogel. To characterize the selective cell adhesion and bone bonding of the HAp-patterned DN gels, we performed *in vitro* and *in vivo* experiments. Bonding strength of the DN gel to the bone was quantitatively measured by using the selectively bonded sample.

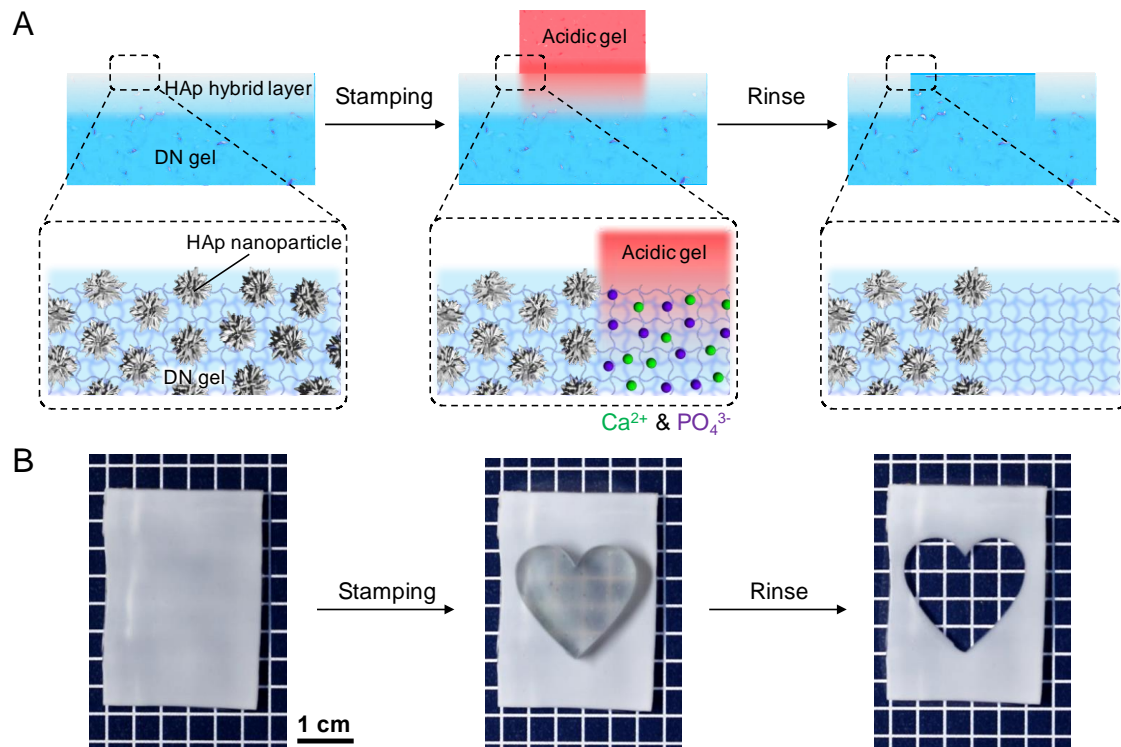


**Fig. 3.1** HAp pattern formation on the DN gel surface by the soft lithography method. (A) Schematic illustration of acid stamping method. (B) Photograph of HAp lithography process on a HAp/DN gel.

## 3.2. Experiments

### 3.2.1. Materials

2-Acrylamido-2-methyl propanesulfonic acid (AMPS) and *N,N'*-ethylenebisacrylamide (EBAM) were provided from Toagosei Co. Ltd, Japan. Dimethylacrylamide (DMAAm), *N,N'*-methylenebisacrylamide (MBAA), 2-oxoglutaric acid ( $\alpha$ -keto), calcium chloride ( $CaCl_2$ ), dipotassium hydrogen phosphate ( $K_2HPO_4$ ), tris(hydroxymethyl)aminomethane, and 35 wt% hydrochloric acid (HCl) were purchased from Wako Pure Chemical Industries, Ltd., Japan. DMAAm monomer was

purified by reduced-pressure distillation before use, and other chemicals were used as received.

### 3.2.2. *Gel synthesis*

The PAMPS/PDMAAm DN gel was synthesized, following our previously reported protocol [6]. First, PAMPS gel was synthesized by UV radical polymerization. The composition of precursor solution was 1 mol/L AMPS as monomer, 4 mol% MBAA as a cross-linker, and 0.1 mol%  $\alpha$ -keto as an initiator. The solution was injected into a cell consisting of a pair of glass plates separated by a silicone spacer. The PAMPS gel was synthesized by UV irradiation (wavelength: 365 nm, 4 mW/cm<sup>2</sup>) for around 6 h in an argon atmosphere. The obtained PAMPS hydrogel was then immersed in an aqueous solution containing 2 mol/L DMAAm, 0.1 mol% MBAA, and 0.1 mol%  $\alpha$ -keto for one day. The soaked PAMPS gel was sandwiched between two glass plates and the 2<sup>nd</sup> network (PDMAAm) was subsequently polymerized in the presence of the PAMPS hydrogel by irradiating with UV light for around 8 h under Ar. After polymerization, the PAMPS/PDMAAm DN gel was immersed in pure water for 1 week, and the water was changed twice daily to remove any un-reacted chemicals. The gel for the acidic stamp was also synthesized as described above, and it was composed of: 1 mol/L AMPS, 6.6 mol% EBAM, and 0.1 mol%  $\alpha$ -keto as the 1<sup>st</sup> network and 2 mol/L DMAAm, 0.06 mol% EBAM, and 0.1 mol%  $\alpha$ -keto as the 2<sup>nd</sup> network.

### ***3.2.3. HAp mineralization***

To form the HAp layer at the outermost surface of the PAMPS/PDMAAm DN gel, the DN gel was first immersed in 1 mol/L Tris buffer (pH 9.0) to adjust the pH inside the hydrogel because a pH of around 9 in an aqueous environment is most suited to HAp<sup>[27]</sup>. The DN gel was dipped in 300 mmol/L K<sub>2</sub>HPO<sub>4</sub> for 110 s, pure water for 10 s, 500 mmol/L CaCl<sub>2</sub> for 110 s, and pure water for 10 s, in this order. This alternative dipping process was repeated for five cycles to mineralize HAp. After the alternative dipping, the hydrogels were dipped in 500 mmol/L CaCl<sub>2</sub> aq solution (pH 11.0) at body temperature for 24 h to ripen the mineralized amorphous calcium phosphate to HAp. Subsequently, a hybridized HAp/DN layer was formed on the surface of the DN gel. Then, the solvent of HAp/DN gel was changed to purified water for removing excess CaCl<sub>2</sub>.

### ***3.2.4. Acid gel stamping***

HAp soft lithography was performed by acid gel stamping. The surface pattern of the stamp DN gel was made by using a programmed laser cutter (ULR-60, Universal Laser Systems, US). The gels were immersed in HCl solutions of various concentrations until equilibrium. Both surfaces of HAp-coated scaffold gel and acid stamp gel were wiped with cellulose wiper to remove excess solution, and the stamp gel was in contact with the scaffold gel for a few seconds. Then, HAp-coated gel was immediately washed with a large amount of pure water.

### 3.2.5. Ultraviolet-visible absorption spectroscopy (UV-Vis)

Temporal HAp dissolution was evaluated by an UV-Vis spectrometer (UV-1800, Shimadzu, Japan). The 2-mm thick HAp/DN gel attached to the acidic gel stamp was fixed in a quartz cell, and the spectra of absorbance at 360 nm vs. time were measured.

### 3.2.6. Microindentation

Local surface moduli of pristine, HAp-coated, and acid-stamped DN gels were evaluated by microindentation. The tip geometry of the brass hammer indenter was a 0.25 mm radius hemisphere. We measured the force-displacement curves of the gel surfaces at 0.25 mm/min test speed on the mechanical tester (Precision Universal/Tensile Tester AG-X, Shimadzu, Japan). According to the Hertz model <sup>[28]</sup> of contact between hemisphere indenter and planar sample, the relation of force ( $F$ ) and displacement ( $d$ ) is described as:

$$d = \left[ \frac{3}{4} \left( \frac{1 - \nu_s^2}{E_s} + \frac{1 - \nu_i^2}{E_i} \right) \right]^{2/3} \cdot F^{2/3} \cdot R^{-1/3}$$

where  $E_s$  ( $i$ ),  $\nu_s$  ( $i$ ), and  $R$  are sample (indenter) modulus, sample (indenter) Poisson's ratio, and radius of indenter tip, respectively. When  $E_s \ll E_i$ ,  $1 - \nu_i^2/E_i$  is regarded as zero. The above equation can transform to:

$$F^{2/3} = \left[ \frac{3}{4} \left( \frac{1 - \nu_s^2}{E_s} \right) \right]^{-2/3} \cdot R^{1/3} \cdot d$$

To calculate  $E_s$ , sample Poisson's ratio  $\nu_s$  was set at 0.5 because of incompressibility and isotropy of the DN gel.

### ***3.2.7. Transmittance electron microscopic (TEM) observation***

To observe the morphology of HAp in DN gel, we carried out TEM observation (H-7650, Hitachi, Japan). Samples were frozen in liquid nitrogen, and the water of the hydrogel was exchanged to acrylic resin (London Resin white) in a chamber of an automatic freeze substitution system (EM AFS2, Leica Microsystems, Germany). Then, 100-nm thick sections of the resin-cured samples were cut using an ultra-microtome (EM UC7i, Leica Microsystems, Germany) and placed on a copper mesh TEM grid. The acceleration voltage of the electron gun for observation was 100 kV.

### ***3.2.8. X-ray diffraction (XRD)***

The crystal phase of mineralized calcium phosphate was evaluated by XRD spectrometer (Ultima IV, Rigaku, Japan). The extraction wavelength and output power of the X-ray generated by the Cu cube were 1.5406 Å and 0.8 kW (40 kV and 20 mA), respectively. The range of diffraction angle  $2\theta$  was from 10° to 60° at 3 degree/min scanning rate.

### ***3.2.9. Contact angle of water***

Wettability of the sample surface was evaluated by contact angle recorder (Dropmaster300, Kyowa Interface Science Co., Ltd., Japan). The hydrogel surface was gently wiped using a cellulose wiper. A droplet of distilled water (2.0  $\mu\text{L}$ ) was made at the tip of the syringe and was attached to the sample.

#### ***3.2.10. Fourier transform infrared spectroscopy (FT-IR)***

Dissolution of HAp was evaluated by Fourier transform infrared spectroscopy (IRT-3000N, Jasco, Japan). Samples were in contact with a zinc selenide prism and were observed by the attenuated total reflection (ATR) method. The range of wavelength and cumulated number were from 900 to 1200  $\text{cm}^{-1}$  and 128 times, respectively.

#### ***3.2.11. Scanning electron microscopy and energy dispersive X-ray spectroscopy (SEM-EDX)***

The surface HAp pattern of HAp/DN gel and element distribution were observed by SEM-EDX (JSM-6010A, JEOL, Japan). Non-dried samples were fixed on the brass hammer base by carbon tape and observed under low vacuum conditions (66 Pa). The acceleration voltage was 20 kV.

#### ***3.2.12. 3D laser microscope***

The width of the surface of the HAp pattern was observed by 3D laser microscopy (VK-

9710, KEYENCE, Japan). Surface water was wiped by a cellulose wiper, and then a reflection image was obtained. The wavelength of the laser light source was 408 nm.

### **3.2.13. Cell culture on HAp/DN gels**

The C3H10T1/2 cell line was obtained from the RIKEN cell bank (Tsukuba, Japan). Cells were maintained in Dulbecco's modified Eagle's medium (GIBCO Invitrogen, Carlsbad, CA), supplemented with 10% fetal bovine serum (GIBCO), in polystyrene tissue culture dishes at 37°C under 5% CO<sub>2</sub>. For cell culturing on HAp/DN gels, gel disks were punched out of the gel plate with a hole punch having an appropriate diameter, and immersed in 0.9% (w/v) NaCl overnight. The sterilization of the gels was performed by autoclave (2 atm, 120 °C, 20 min.). Compared Young's moduli and volumes of gel before and after sterilization, the degradation of the samples by autoclave sterilization was negligible ( $E_{before} = 0.55 \pm 0.01$ ,  $E_{after} = 0.53 \pm 0.03$  MPa  $V_{after}/V_{before} = 1.0$ ). After the sterilization, the gel disks were placed in polystyrene tissue culture dishes and immersed in culture medium overnight to reach equilibrium. The cells were seeded on gels at a cell density of  $1 \times 10^4$  cells/cm<sup>2</sup>. The media was replaced every two days. To visualize cells on HAp/DN gels, F-actin staining was performed. Cells were fixed with 4% paraformaldehyde in phosphate-buffered saline (PBS), and permeabilized with 0.1% Triton X-100 in PBS. Then, cells were incubated with rhodamine-phalloidin (Thermo Fisher Scientific, USA) for 1 hour. After rinsing with PBS, the gel was placed on a glass slide



so that the cell-adhered surface faced downward. Fluorescent images were obtained with a fluorescence microscope (Eclipse TE 300, Nikon, Japan).

### ***In vivo test***

#### ***3.2.14. Animals***

Animal experiments were carried out at the Institute of Animal Experimentation according to the Rules and Regulations of the University's Animal Care and Use Committee. Twenty-five of 6-month old female Japanese White rabbits were used in the *in vivo* study.

#### ***3.2.15. 90° peeling test of HAp-patterned DN gel sheet bonded to bone***

We conducted a 90° peeling test to quantitatively evaluate the adhesive strength between HAp-patterned DN gel and bone tissue using a rabbit calvarial defect model. The DN gel sheet ( $20 \times 5 \times 1 \text{ mm}^3$ ) with a partial HAp-coated layer ( $7 \times 5 \text{ mm}^2$ ) was prepared by the acid stamping technique for *in vivo* implantation. A sagittal incision was made along the midline from the frontal bone to the occipital bone, and the periosteum was incised and elevated to expose the cranial bone. The underlying bone was carved to a depth of 1 mm with a high-speed bur to create a rectangular flat defect. The HAp-coated DN gel sheet was then placed in the defect and covered with the hand-made silicone rubber protector with four plastic pegs at its corner. The protector was stabilized by inserting the pegs

into the small holes created at the four corners of the defect. We implanted one sheet-like sample per a rabbit. After the DN gel sheet implantation, the wound was sutured to cover the bone securely. The rabbits were sacrificed by injecting a lethal dose of pentobarbital at 2, 4, and 6 weeks after implantation, and their skulls with the DN gel sheet were carefully harvested. The specimen was horizontally fixed on a plastic base plate by using polymethylmethacrylate resin, and the HAp uncoated part of the DN gel sheet was clamped by the upper jig connected to a 50 N load cell. The test was performed at 50 mm/min velocity on the mechanical tester (Precision Universal/Tensile Tester AG-X, Shimadzu, Japan). Eight specimens were examined at each period. The peeling energy was defined as maximum peeling force divided by the width of the gel sheet.

### ***3.2.16. Demonstration of selective bonding to bone in vivo***

We created a DN gel cord ( $1 \times 2 \times 36 \text{ mm}^3$ ) in which each end ( $1 \times 2 \times 8 \text{ mm}^3$ ) was mineralized with a 500- $\mu\text{m}$ -thick HAp layer by acid stamping. Two 2-mm drill holes were created at the lateral aspect of the rabbit femoral diaphysis to implant the HAp/DN gel ligament parallel to the femoral axis. The distal hole was drilled 20 mm proximal from the distal end of the femur, and the proximal hole was drilled 15 mm proximal to the distal hole at  $30^\circ$  to the bone surface. Both ends of the HAp/DN gel portion of the sample were then implanted inside the bony hole, being careful to leave the 20-mm DN gel portion outside the bone. Two animals were sacrificed by injection of a lethal dose

of pentobarbital at 4 weeks after surgery and used for biomechanical evaluations. The two ends of the harvested femoral bone were fixed by upper and lower jigs of the mechanical tester (Tensilon RTC-1310A, Orientec, Japan), and then the femoral bone was sectioned at the center to elongate the bridged DN gel cord. The elongation velocity was 20 mm/min.

### ***3.2.17. Statistical Analysis***

Results are presented as mean standard deviation (SD). Comparisons of data on the young's modulus were performed with the use of analysis of *t*-test. Statistical significance was set at  $p < 0.0001$ .

## **3.3 Results and discussion**

### ***3.3.1 Micro patterning of hydroxyapatite by soft lithography on hydrogels***

First, we synthesized conventional DN gel consisting of AMPS as the 1<sup>st</sup> network and DMAAm as the 2<sup>nd</sup> network by two-step UV polymerization according to a previous report [6]. Next, we mineralized HAp particles, which are a spiny spherical shape and 600 nm in diameter, at the outermost layer of the DN gel by the alternative dipping method [22]. The mineralized HAp layer was 500  $\mu\text{m}$  in thickness from the surface and the HAp particles were tightly entrapped in the double network gel, incorporating the polymer network of the DN gel. This HAp/DN gel maintained the

original DN gel's mechanical properties, including softness, flexibility, and toughness.

To prepare the acid gel stamp, we synthesized a DN gel with 5-mm thickness using EBAM as a crosslinker. This gel was immersed in 35 wt% HCl solution for 1 day to reach equilibrium. Next, we placed the acid gel stamp on the HAp-coated DN gel for 10 s. Immediately HCl diffused into the HAp-coated DN gel and HAp nanoparticles dissolved at the contact region (**Supplementary Movie 1**)<sup>[1]</sup>. Then, the HAp-coated DN gel was immediately immersed in a large volume of water to remove excess HCl completely. **Fig. 3.1B** shows the images of HAp/DN gel before, during, and after stamping using a heart-shaped acid gel stamp. The turbid gel became transparent at the contact region, suggesting that the HAp in the gel was removed successfully.

To confirm the HAp etching, we performed x-ray diffraction (XRD) and infrared (IR) measurements. XRD profiles showed that the peaks characteristic to crystalline HAp disappeared completely after acid stamping (**Fig. 3.2A**). Moreover, the IR peaks of phosphoric acid that originated from HAp (P=O stretching) also disappeared (**Fig. 3.2B**). Additionally, we measured the surface property of the DN gel by contact angle of water (CAW). Although the HAp/DN gel showed high CAW due to the presence of HAp nanoparticles on its surface, the CAW of the stamped HAp/DN gel was equal to that of the pristine DN gel (**Fig. 3.2C**). These results indicated that HAp was completely dissolved by HCl, and calcium and phosphate ions of the HAp component were washed out of the DN gel. To check if the acid gel stamping caused any structural damage to the DN gel, the Young's

modulus of the stamped region was evaluated by the micro-indentation test with Hertz equation. The stamped sample showed the same value as the neat DN gel, and it was slightly lower than that of the HAp-coated one (**Fig. 3.2D**). This indicated that this method is non-destructive to the DN hydrogel.

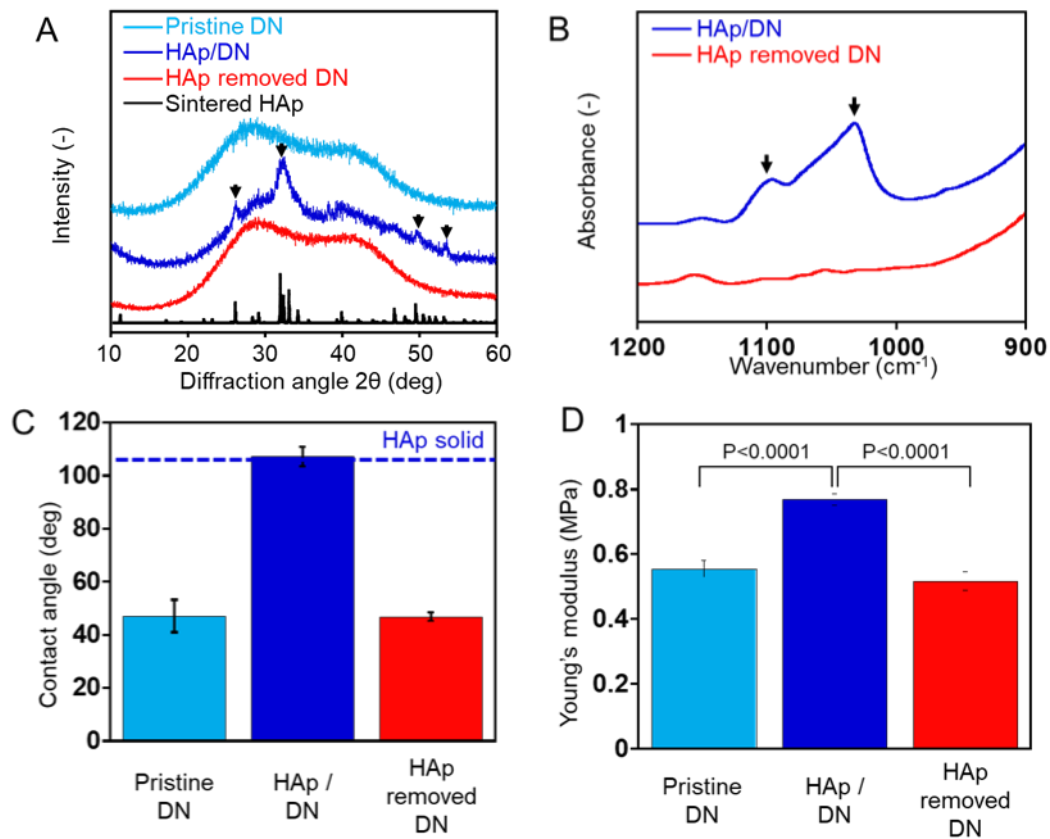


**Fig. 3.2** Characterization of HAp etching. (A) X-ray diffraction patterns of various DN gels. X-ray diffraction peaks at the bottom are the result of sintered HAp. Arrows indicate HAp crystalline peaks. (B) IR spectra of HAp/DN gel and HAp-removed DN gel. Phosphate peaks from HAp are indicated by arrows. (C) Surface wettability measured by contact angle of water. Dotted line in the histogram is the result of sintered HAp. (D) Young's modulus of pristine DN gel, HAp/DN gel, and HAp-removed DN gel measured by indentation test.

The etching rate of HAp inside the DN gel depended on the HCl concentration of the pre-soaking solution (**Fig. 3.3A**). The turbidity of the HAp/DN gel, which is related to the amount of HAp nanoparticles in the DN gel, was measured as a function of stamp contact time by UV-visible light spectroscopy. The absorbance decreased with the contact time, and the decreasing rate became faster with increasing HCl concentration. For the condition of 35 wt% HCl aq., HAp completely dissolved within 5 s, which lead to a high resolution of wet lithography. Moreover, for practical use, just the outermost HAp should be effective for *in vitro* cell adhesion and *in vivo* osteoconduction. Thus, we tried the outermost HAp wet lithography by short time stamping with a low concentration of HCl aq. (5 s, 3.5 wt%). To observe the distribution of HAp, TEM observation was performed. **Fig. 3.3B** shows the TEM images of cross-sectional HAp distribution near the surface layer of the pristine and stamped HAp/DN gel. HAp nanoparticles located at the outermost layer of DN gel were completely dissolved after stamping, but HCl did not affect HAp over 40  $\mu\text{m}$  inside the gel surface. This result indicates that a very short stamping time (5 s) is enough for patterning the outermost layer of HAp. The short stamping time should also lead to high resolution due to less lateral-direction diffusion of HCl.

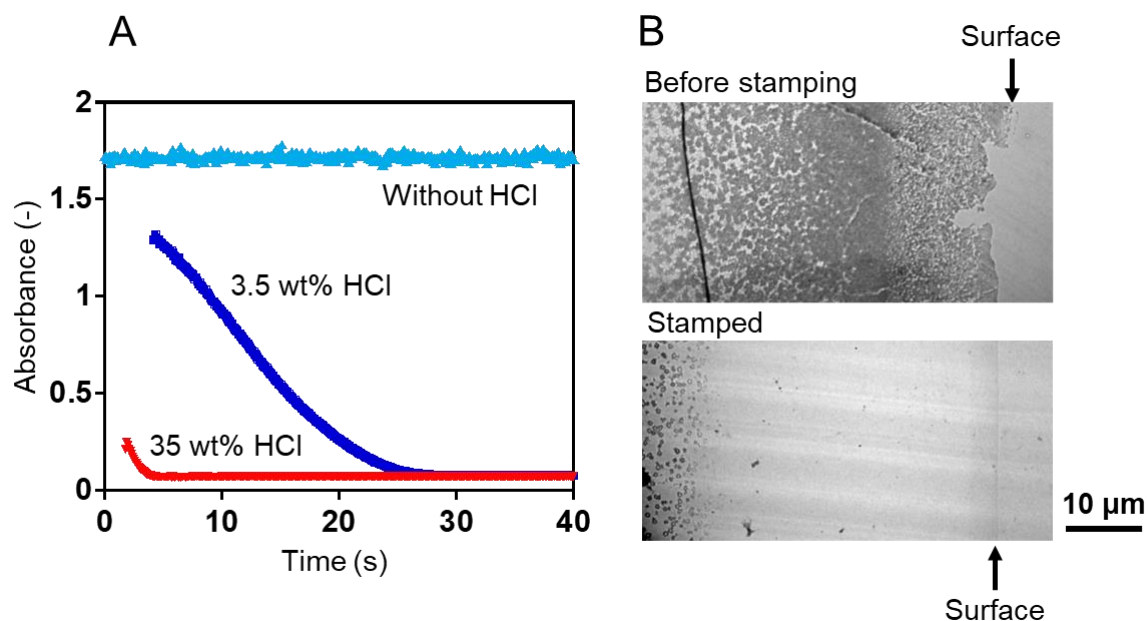


**Fig. 3.3** Surface HAp etching by acid gel stamping. (A) HAp etching rate with different HCl concentration measured by turbidity at 360 nm. (B) Transmission electron micrograph images of pristine HAp/DN gel and etched HAp/DN gel (3.5 wt% HCl, 5 s). The depth of the dissolved HAp layer is about 40  $\mu\text{m}$  from the surface of the gel.

To clarify the relationship between HCl concentration and pattern resolution, we induced grooves of varied width on the surface of the gel stamp by using a programmed laser cutter, and investigated the relationship between the groove width on the stamp and the remaining HAp pattern width on the HAp/DN gel by 3D laser microscopy for different HCl concentrations (**Fig. 3.4A, B**). The stamp time was kept at 15 s. At low HCl concentrations of 3.5 wt% and 10 wt%, the HAp pattern width was almost the same as that of the stamp, and we could achieve patterning on the scale of

hundreds of microns, while the width of the stamp in this study was limited by the resolution of the laser cutter (~100  $\mu\text{m}$ ). However, at high HCl concentration of 35 wt%, HCl diffusion in the lateral direction was very fast and the width of the HAp pattern was much smaller than the width of the groove and was difficult to control.

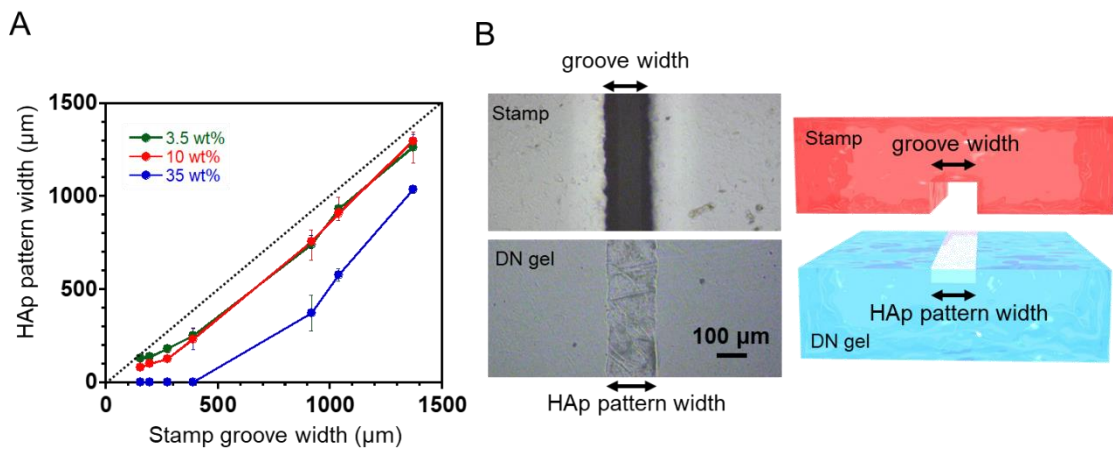


**Fig. 3.4** Effect of HCl concentration of the stamp on the etching resolution. (A) Correlation between the stamp groove width and HAp pattern width for varied HCl concentrations. (B) Microscopic image of surfaces of 3.5 wt% acidic stamp and stamped HAp/DN gel with a schematic illustration. The groove depth was 1 mm. The stamp time was kept at 15 s for all the experiments.

### 3.3.2 *In vitro* cell culture test

To confirm selective adhesion of cells on HAp-patterned DN gel, we performed an *in vitro* cell culture experiment. First, HAp-patterned gel with a honeycomb feature was prepared and the HAp location on the honeycomb skeleton was observed by microscope, scanning electron microscope, and



elemental mapping (**Fig. 3.5A, B, C**). HAp lithography was successfully completed, and there was no residual HAp on the patterned area. We next examined the adhesion and proliferation of cells cultured on patterned HAp/DN gels. For the cell culture test, we used mouse multipotent stem cells C3H10T1/2, which are known to differentiate into osteoblasts. Since HAp/DN gel does not have optical transparency, we performed F-actin staining using rhodamine-phalloidin to visualize cells. As shown in **Fig. 3.5D**, C3H10T1/2 cells did not adhere to areas without HAp coating. In contrast, cells attached to the surface-retained HAp coating and proliferated to form a nearly confluent monolayer after 3 days of culture, which suggests that HAp nano-crystals allow for cell adhesion and proliferation. The cells showed fibroblast-like morphology with long cytoplasmic processes. Cells at the periphery of the HAp coating showed elongated morphology oriented along the edge (**Fig. 3.5E**). Thus, we succeeded in introducing HAp nanoparticles as anchorage for cells at the surface of the hydrogel.

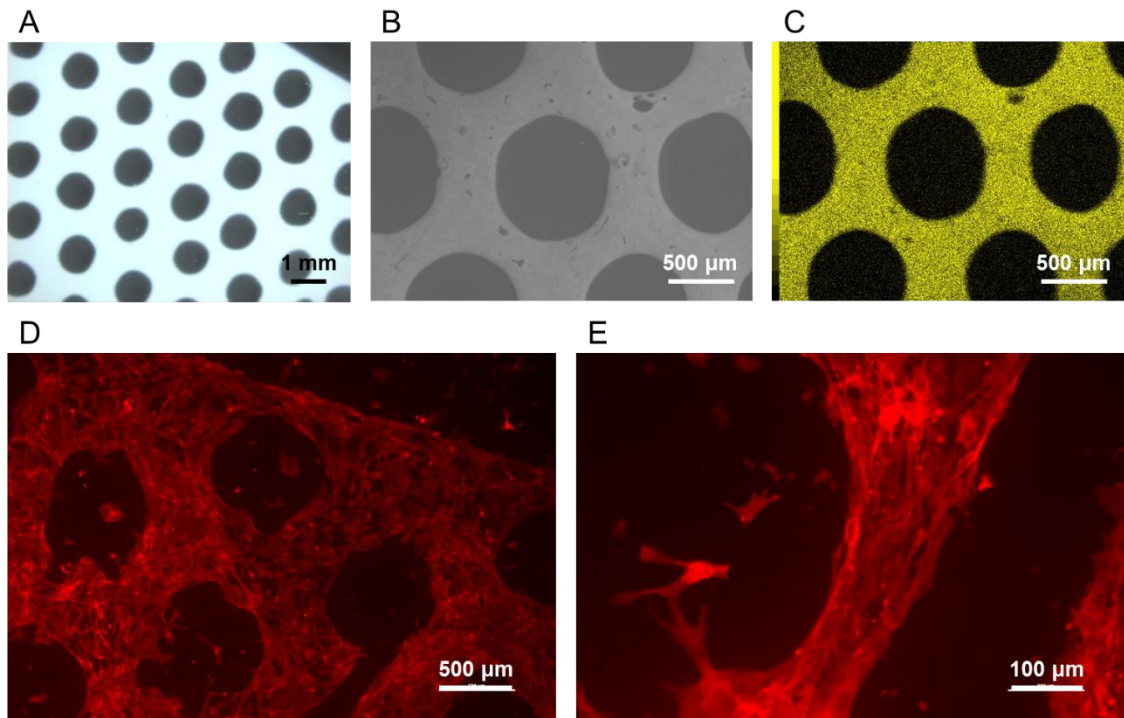


**Fig. 3.5** Cell culture test on HAp-patterned DN gel. (A) Microscopy image of honeycomb-pattern DN gel. (B) High magnification image by scanning electron microscope. (C) Calcium mapping of image (B). Calcium is main component of HAp. (D) and (E) Effect of HAp coating on cell adhesion and proliferation. C3H10T1/2 cells were seeded on patterned HAp/DN gel and cultured for 3 days. The cell morphology was observed after rhodamine-phalloidin staining.

### 3.3. *In vivo* osteoconduction test

Next, we conducted *in vivo* selective bonding of HAp-patterned DN gel to bone tissue. We prepared a DN gel sheet of  $20 \times 5 \times 1 \text{ mm}^3$  in dimension, and patterned one-third of its surface area with a HAp layer. The gel sheet was implanted in a rabbit calvarial defect. After 2, 4, and 6 weeks

implantation, we harvested the skull with the DN gel sheet and performed a 90° peeling test to measure the bonding strength, as shown in **Fig. 3.6A**. **Fig. 3.6B** shows the image of a 4-week implanted DN gel sheet in the calvarial defect. Even though the bone regenerative capability of the skull was relatively weak, the HAp-coated region of the DN gel strongly bonded to the bone tissue. On the other hand, the HAp-removed region did not show any bonding even though the whole gel surface was in contact with the bone defect. This selective bonding allowed us to quantitatively evaluate adhesion strength from the peeling test (**Fig. 3.6C**, **Supplementary Movie 2<sup>[1]</sup>**). In this peeling test, we observed three events: non-adhesion, peeling off, and gel fracture due to the individual differences. The peeling off occurs when adhesion strength is lower than the strength of the bulk gel, while the gel fracture is observed in the opposite condition. **Fig. 3.6D** shows the event probabilities calculated from a population of eight specimens. As the implantation period increased, the probability of non-adhesion decreased, and the adhesion event became dominant. Moreover, the probability of fracture of gel body among the adhesion event increased with implantation period indicating that the strength of adhesion exceeded that of bulk gel for long implantation time. **Fig. 3.6E** shows the representative peeling force-displacement curve of the gel sheets implanted for 2, 4, and 6 weeks. By increasing the implantation period, the maximum peeling force was increased. Some yielding points were observed in the profile curves because the adhesion to bone tissue was not homogeneous at the HAp-coated region. As shown in **Supplementary Movie 2<sup>[1]</sup>**, fast peeling off phenomena owing to the existence of robust adhesive

points were confirmed. Peeling energy calculated from **Fig. 3.6E** increased with increasing implantation period and reached up to around  $150 \text{ J/m}^2$ , equal to the strength of the bulk gel (**Fig. 3.6F**). Therefore, the HAp-coated gel with acid stamp patterning can selectively form sufficiently strong bonding to targeted regions of bone tissue even with complex geometry.

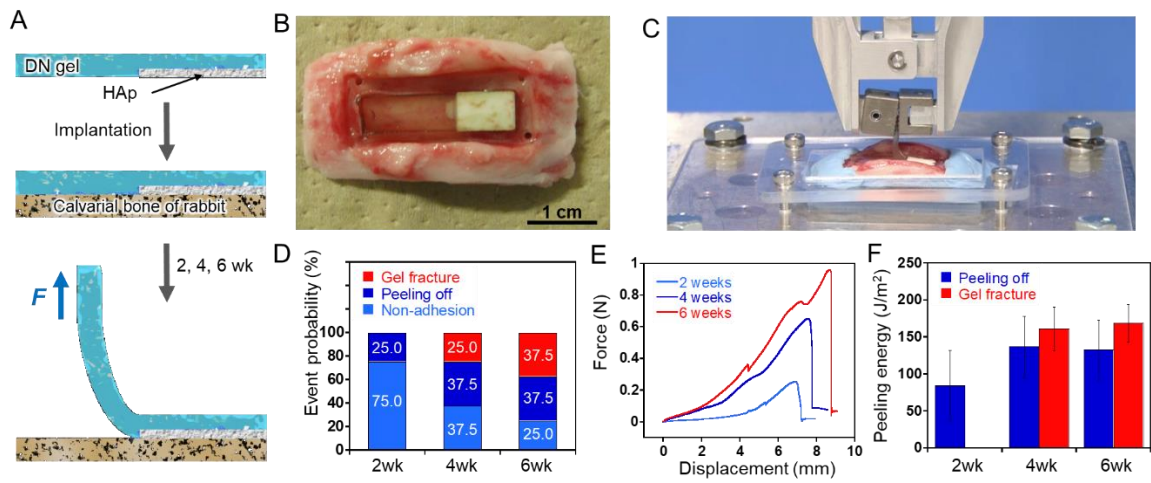


**Fig. 3.6** Peeling test to measure the bonding strength of the DN gel to the bone with different implantation periods. (A) Schematic illustration of peeling test. (B) Image showing HAp-patterned DN gel ( $20 \times 5 \times 1 \text{ mm}^3$ ) in the rabbit calvarial defect after 4 weeks implantation. (C) Image showing the peeling test for a sample after 4 weeks implantation. (D) Event probability of the peeling test. (E) Peeling force-displacement curves of HAp-patterned area after different implantation times. Binding force increased with implantation time. The HAp-patterned area was  $7 \times 5 \text{ mm}^2$ . (F) Peeling energy calculated from maximum peeling force and sample width for each sample. The peeling energy due to gel fracture indicates that the bonding strength was higher than the value shown and could not be measured in this study. The statistical results for each implantation period were from eight specimens.

We furthermore demonstrated *in vivo* bonding of HAp-patterned DN gel to bone tissue as the artificial ligament model. We created a HAp-patterned DN gel cord whose HAp at the middle part was selectively removed by acidic stamping (**Fig. 3.7A**) and inserted the two ends into the defects created in the rabbit femur (**Fig. 3.7B**). After 4-week implantation, the bone was harvested (**Fig. 3.7C**) and cut in the middle. The tensile test showed that the gel was not pulled out from the bone tunnel (**Fig. 3.7D**), and failure occurred within the middle section of the DN gel cord at a nominal stress of 0.2 MPa (**Fig. 7E, Supplementary Movie 3<sup>[1]</sup>**). The result indicated that developed HAp patterning method can regulate osteoconductive area like living soft tissues and that the osteoconductive adhesion of the HAp coated region was sufficiently stronger than that of the DN gel body.

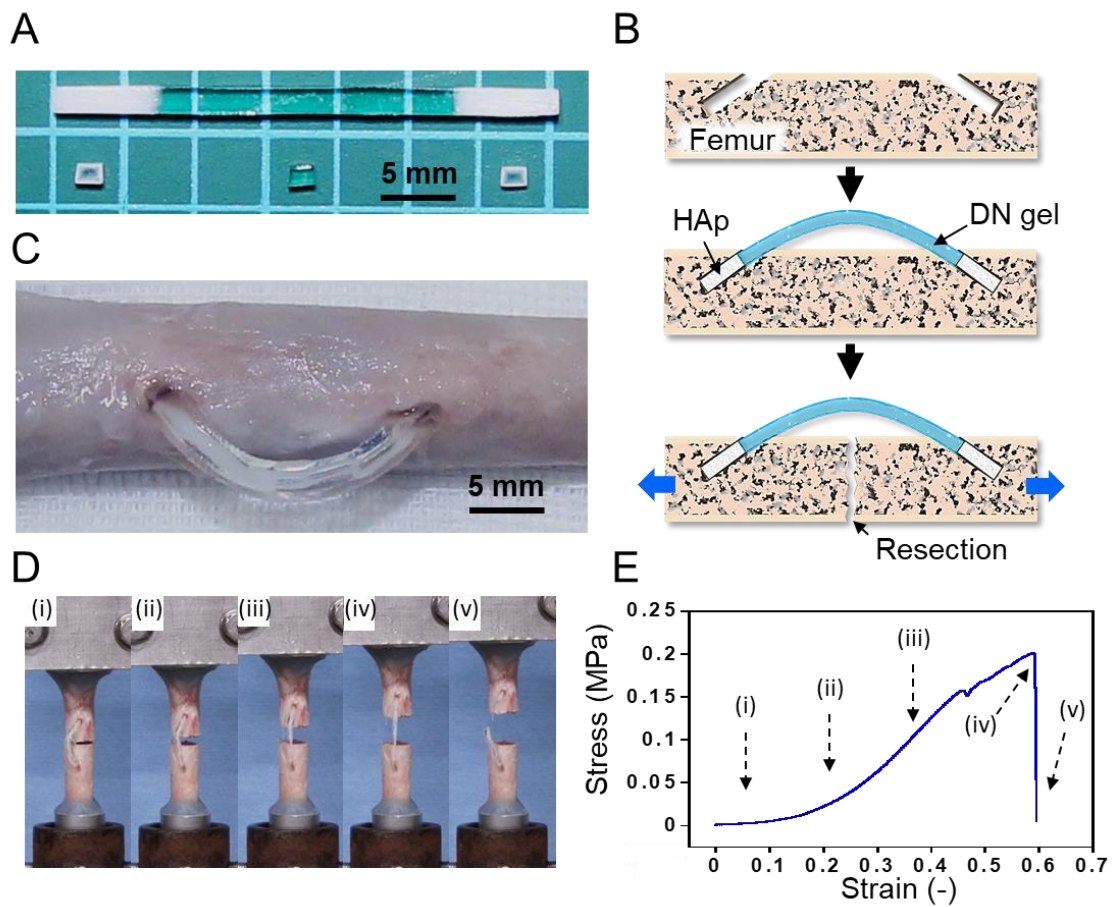


**Fig. 3.7** *In vivo* ligament model test. (A) DN gel cord in which a short part of each end was mineralized with HAp. (B) Illustration of DN gel insertion process to the two bone tunnels created in the rabbit femur. (C) Image of the harvested DN gel inserted into the bone after 4-week implantation. (D, E) Tensile test images and stress-strain curve of the DN gel bonded to the bone. The DN gel was not pulled out from the bone tunnel even at its fracture, indicating strong bonding of the gel to the bone.

### 3.4 Conclusions

We developed a simple and quick HAp lithography method, which could make a desirable

HAp pattern at the surface of the hydrogel without any damage, by using an acid-containing hydrogel as a stamp. This method allowed us to obtain the HAp pattern with fine resolution (~100  $\mu\text{m}$ ) on DN gel. The HAp-patterned DN gel exhibited cell adhesion selectively. Moreover, from the *in vivo* ligament model test, selective bone bonding of the tough hydrogel was also achieved. These results substantially promote the applications of hydrogel to various artificial tissues, which have complex-shaped interfaces with the bone. Furthermore, this work is applicable for developing complex-shaped scaffolds created with the HAp-patterned hydrogels for *ex vivo* cell culture studies. This technique has various applications in both tissue engineering and future tailor-made soft biomaterials.

### 3.5 References

- [1] R. Kiyama, T. Nonoyama, S. Wada, S. Semba, N. Kitamura, T. Nakajima, T. Kurokawa, K. Yasuda, S. Tanaka, J. P. Gong, *Acta Biomater.* **2018**, *81*, 60.
- [2] J. L. Drury, D. J. Mooney, *Biomaterials* **2003**, *24*, 4337.
- [3] K. Y. Lee, D. J. Mooney, *Chem. Rev.* **2001**, *101*, 1869.
- [4] F. Mano, R. L. Reis, R. M. P. Silva, *Trends Biotechnol.* **2007**, *25*, 577.
- [5] Y. S. Pan, D. S. Xiong, R. Y. Ma, *Wear* **2007**, *262*, 1021.
- [6] J. Gong, Y. Katsuyama, T. Kurokawa, Y. Osada, *Adv. Mater.* **2003**, *15*, 1155.
- [7] Y. Okumura, K. Ito, *Adv. Mater.* **2001**, *13*, 485.

- [8] K. Haraguchi, T. Takehisa, *Adv. Mater.* **2002**, *14*, 1120.
- [9] T. Sakai, T. Matsunaga, Y. Yamamoto, C. Ito, R. Yoshida, S. Suzuki, N. Sasaki, M. Shibayama, U. Chung, *Macromolecules* **2008**, *41*, 5379.
- [10] J. Saito, H. Furukawa, T. Kurokawa, R. Kuwabara, S. Kuroda, J. Hu, Y. Tanaka, J. P. Gong, N. Kitamura, K. Yasuda, *Polym. Chem.* **2011**, *2*, 575.
- [11] K. Yasuda, J. P. Gong, Y. Katsuyama, A. Nakayama, Y. Tanabe, E. Kondo, M. Ueno, Y. Osada, *Biomaterials* **2005**, *26*, 4468.
- [12] K. Arakaki, N. Kitamura, H. Fujiki, T. Kurokawa, M. Iwamoto, M. Ueno, F. Kanaya, Y. Osada, J. P. Gong, K. Yasuda, *J. Biomed. Mater. Res. Part A* **2009**, 1160.
- [13] K. Yasuda, N. Kitamura, J. P. Gong, K. Arakaki, H. J. Kwon, S. Onodera, Y. M. Chen, T. Kurokawa, F. Kanaya, Y. Ohmiya, Y. Osada, *Macromol. Biosci.* **2009**, *9*, 307.
- [14] T. Nonoyama, S. Wada, R. Kiyama, N. Kitamura, *Adv. Mater.* **2016**, *28*, 6740.
- [15] S. Wada, N. Kitamura, T. Nonoyama, R. Kiyama, T. Kurokawa, *Acta Biomater.* **2016**, *44*, 125.
- [16] L. Sun, C. C. Berndt, K. A. Gross, A. Kucuk, *J. Biomed. Mater. Res. Part A* **2001**, *58*, 570.
- [17] M. T. I. Mreda, N. Kitamura, T. Nonoyama, S. Wada, K. Goto, X. Zhang, T. Nakajima, T. Kurokawa, Y. Takagi, K. Yasuda, J. P. Gong, *Biomaterials* **2017**, *132*, 85.
- [18] S. N. Bhaskar, J. M. Brady, L. Getter, M. F. Grower, T. Driskell, *Oral Surgery, Oral Med.*



*Oral Pathol. Oral Radiol.* **1971**, 32, 336.

- [19] P. I. Branemark, *J. Prosthet. Dent.* **1983**, 50, 399.
- [20] L. L. Hench, R. J. Splinter, W. C. Allen, T. K. Greenlee, *J. Biomed. Mater. Res.* **1971**, 5, 117.
- [21] L. L. Hench, *J. Am. Ceram. Soc.* **1991**, 74, 1487.
- [22] T. Taguchi, A. Kishida, M. Akashi, *Chem. Lett.* **1998**, 711.
- [23] Y. Xia, G. M. Whitesides, *Annu. Rev. Mater. Sci.* **1998**, 28, 153.
- [24] C. J. Campbell, S. K. Smoukov, K. J. M. Bishop, E. Baker, B. A. Grzybowski, *Adv. Mater.* **2006**, 18, 2004.
- [25] B. A. Grzybowski, K. J. M. Bishop, *Small* **2009**, 22.
- [26] B. A. Grzybowski, K. J. M. Bishop, C. J. Campbell, M. Fialkowski, S. K. Smoukov, *Soft Matter* **2005**, 1, 114.
- [27] J. C. Elliott, *Rev. Mineral. Geochemistry* **2002**, 428.
- [28] C. T. McKee, J. A. Last, P. Russell, C. J. Murphy, *Tissue Eng. Part B Rev.* **2011**, 17, 155.

# CHAPTER 4

## Nano Scale Direct Imaging of a Rubber Elastic Hydrogel Network

### 4.1 Introduction

Network polymers with rubber elasticity, including hydrogels and elastomers, are widely used soft materials in society, such as biomaterials, stretchable electronics, tires, sealing, etc. [1-6] The network structure of this class of materials is not ideally homogeneous. Depending on the synthesis process, most of network polymers contain, genetically, a large distribution in molecular weight of polymer strands between crosslinking points as well as abundant of topological defects, including loops and dangling chains.[7-9] Due to rubber elasticity, the polymer chains take coiled conformation at relaxed state, which makes it difficult to identify the crosslinked strands from the loops and dangling chains by the existing structure analysis approaches, including X-ray/neutral/light scattering.[10-13] Furthermore, the topological structure of network polymers at surfaces is hardly studied. Developing suitable methods to directly observe nano scale topological network structure in real space will push forward the polymer material research and development.

Transmission electron microscopy (TEM) and atomic force microscopy (AFM) are the most widely used imaging techniques to directly observe the nanostructures of materials in real space.[14,15] Compared to AFM, TEM is more suitable for nano-scale observation of soft materials as the observation is performed at a state that the thermal motion of the elastic network is quenched by

using resin substitution or at cryogenic temperatures<sup>[16,17]</sup>. However, existing TEM observation methods, such as electron staining, phase contrast, and scanning TEM<sup>[18-21]</sup>, cannot produce a sufficient contrast for the target network polymers imbedded in resin matrix.

In this chapter, we report a method to image, for the first time, the topological network structure of a chemically crosslinked network polymer synthesized by free radical polymerization. In this method, we prestretch and hold the target polymer network into extended conformation using a double network technique<sup>[22,23]</sup>, and then selectively staining the target network by mineralizing nanoparticles to achieve sufficient electronic contrast. This method allows us to image network polymer over a wide length scale, from the network topological structure in tens nm to meso-scale heterogeneity in  $\mu\text{m}$ . This method also allows us to visualize, for the first time, the graft chains on the surface of the networks. These observations provide important insights for understanding the kinetics of network polymer formation, the mechanical behavior, the surface properties of hydrogels and elastomers.

## **4.2 Experiments**

### **4.2.1 Materials**

The 2-acrylamido-2-methyl propanesulfonic acid (AMPS) monomer was provided by Toagosei Co. Ltd, Japan. The dimethylacrylamide (DMAAm) monomer, *N, N'*-methylenebisacrylamide

(MBAA) crosslinker, 2-oxoglutaric acid ( $\alpha$ -keto) initiator, iron (III) chloride hexahydrate and 2-morpholinoethanesulfonic acid monohydrate (MES) buffer were purchased from Wako Pure Chemical Ind., Ltd., Japan. Osmium tetroxide ( $\text{OsO}_4$ ) was acquired from TAAB Laboratories Equipment Ltd., England. DMAAm monomer was purified by reduced pressure distillation before usage. The other chemicals were used as received.

#### *4.2.2 Network sample synthesis*

The precursor solution of PAMPS network was comprised of 1 M AMPS as the monomer, 1–8 mol% MBAA as the crosslinker, and 0.1 mol%  $\alpha$ -keto as the initiator in water. The precursor solution of PDMAAm network was comprised of 2 M DMAAm monomer, 0.1 mol% MBAA, and 0.1 mol%  $\alpha$ -keto in water. Each mol% is relative to the corresponding monomer. The plate-shaped PAMPS network was synthesized from the precursor solution in a mold made of a 2 mm thick silicone spacer sandwiched between two glass plates, by UV polymerization for 8 h in a chamber filled with inert Ar gas. Then, the PAMPS gel was removed from the mold and soaked in a PDMAAm network precursor solution for 1 day until reaching equilibrium. The PAMPS gel, substantially swelled in the PDMAAm network precursor solution, was sandwiched between two glass plates and irradiated with UV to form PDMAAm network for 6 h in Ar atmosphere<sup>[22]</sup>. The obtained samples were immersed in distilled water for one week to completely remove residual chemicals. All glass plates used in the molds were

heated in a 500 °C oven for 1 h to remove any residual organics before use. The samples were coded according to the PAMPS network crosslinker ratio  $C_{\text{MBAA}}$  (mol%), as PAMPS- $C_{\text{MBAA}}$ . PAMPS-4 micro-gels and supermacroporous PAMPS-0.5 gel were also prepared by suspension polymerization and cryogelation using the protocols reported.<sup>[24,25]</sup> The mesh size of the supermacroporous PAMPS-0.5 gel is less than that of conventional PAMPS-0.5 gel since the concentration of the precursor solution were increased by ice formation during freezing in the cryogelation. The PDMAAm network in these gels was introduced using the protocol described above.

#### ***4.2.3 Average mesh size estimation***

The average mesh sizes  $\xi_0$  of the PAMPS network and the PDMAAm network at their as-prepared state were estimated from the density of elastically effective strands  $\nu_0=1/\xi_0^3$  and the  $\nu_0$  was estimated from the Young's modulus  $E$  of the network samples at the as-prepared state as follows.

$$E=3\nu_0k_B T=3k_B T/\xi_0^3$$

where  $k_B$  and  $T$  are Boltzmann constant and temperature, respectively. The average mesh size of the PAMPS network in TEM observation state  $\xi$  was estimated from the thickness ratio  $\lambda_s$  of the resin-cured PAMPS sample relative to its as-prepared state. Assuming the affine deformation of the polymer strands between the crosslinkers with the macroscale deformation, the end-to-end distance of these strands were increased by a factor of  $\lambda_s$  in comparing with that in their relaxed state.

$$\xi = \lambda_s \times \xi_0$$

The compressive stress-strain curves of the PAMPS single network gel and PDMAAm single network gel in their as-prepared state were measured using a mechanical tester (Tensilon RTC-1310A, Orientic Co., Japan). The samples were cut into discs with 15 mm diameter using a cutting machine. The test was performed at a strain rate of  $1/600 \text{ s}^{-1}$ .  $E_{as-pre}$  was estimated from the initial slopes of the stress-strain curves. Each test was performed on five samples.

#### ***4.2.4 Mineral staining and transmission electron microscopy (TEM) observation***

For mineral staining, the hydrogels were immersed in a staining solution of 2.5 M  $\text{FeCl}_3$  for 1 day at 25 °C. Subsequently, the gels were immersed in pure water or 0.1 M MES buffer solution to increase pH and amorphous ferric oxide nanoparticles were mineralized on the PAMPS network. The specimens for TEM observations were prepared by freezing the hydrogels in liquid nitrogen and the water of the hydrogels was substituted with ethanol and then acrylic resin (London Resin white, medium) in the chamber of an automatic freeze substitution system (EM AFS2, Leica Microsystems, Germany). The sample thickness changes in these processes is shown in **Figure 4.1**. For all PAMPS samples with different formulations, the final thickness changes of the resin-cured specimen are within 10% relative to that of the PAMPS samples in water. Then, 100 nm thick resin-cured specimens were cut using an ultra-microtome knife (EM UC7i, Leica Microsystems, Germany) and then placed on a

carbon-supported copper mesh grid for TEM observation.

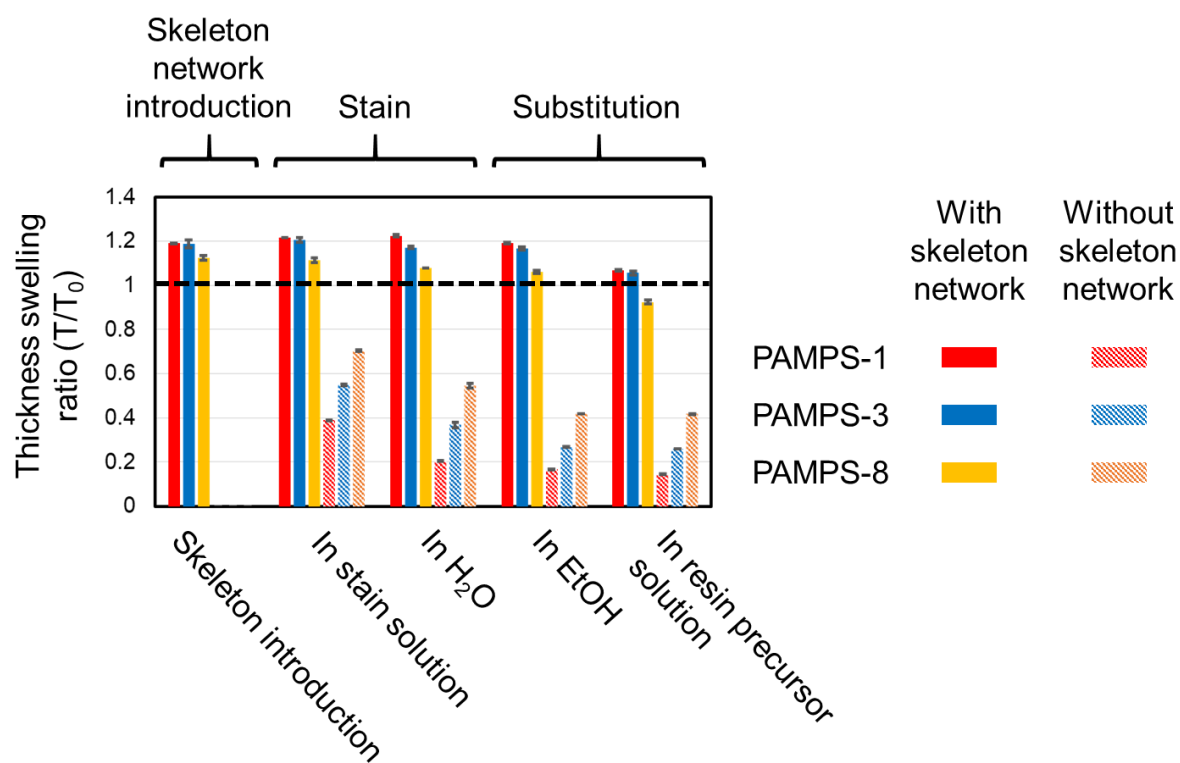


**Figure 4.1** Thickness swelling ratio of the PAMPS networks with different crosslinker density during staining and resin substitution.  $T_0$  is the thickness of the PAMPS single network swelled in water. The black dashed line in the graph indicates the constant size ( $T/T_0=1$ ). By introducing the PDMAAm skeleton, the samples swell slightly ( $T/T_0=1.1-1.2$ ). The samples without a skeleton network significantly shrink in staining solution and in resin precursor solution ( $T/T_0=0.1-0.4$ ). With the skeleton network, the change in the final thickness of the resin-cured specimen is within 10% ( $T/T_0=0.9-1.1$ ). The error bars indicate the standard deviation for five samples.

2D TEM observations (H-7650, Hitachi, Japan) were performed at an acceleration voltage of 100 kV

of the electron gun. 3D TEM and energy dispersive X-ray spectrometry were performed using a TEM tomographic system (JEM-1400 and EM-05500TGP, JEOL, Japan) and scanning electron microscope (JEM-F200, JEOL, Japan). The acceleration voltage of the electron guns was 120 and 200 kV, respectively. It should be mentioned that the conventional electron stain (Osmium (VIII) oxide) that labels one carbon–carbon double bond with one heavy atom does not provide enough contrast to the sparse and extremely thin network of hydrogels showing rubber elasticity.

#### **4.2.5 Data analysis**

The total apparent chain length in the 2D TEM images of PAMPS-1 samples was estimated using ImageJ software<sup>[26]</sup>. The original TEM images were skeletonised and the total pixels were measured in the images of five different position on same sample.

The theoretical network strand contour length could be calculated from the PAMPS concentration  $C = C_0/\lambda_s^3$  in the specimen after resin exchange, where  $C_0$  is the PAMPS monomer concentration at synthesis. The total contour length of PAMPS chain in a TEM view volume  $V$  is

$$L = b C N_A V = b C_0 N_A V / \lambda_s^3$$

Here  $b$  and  $N_A$  are the monomeric length of PAMPS and Avogadro number, respectively.

Because TEM shows three-dimensional object into two-dimensional flat image, we should calculate 2D apparent polymer length. When a three-dimensional straight line is projected in 2D, the



2D apparent length can be written by the original length multiplied by  $\cos\theta$ , where  $\theta$  is the angle of the line with respect to the projection plane. In the view field, there are polymers with various directions,  $0^\circ$  to  $180^\circ$ . The integral value of  $\cos\theta$  in the range of  $0^\circ$  to  $180^\circ$  is  $2/\pi$ . Thus, 2D apparent polymer contour length in the viewed field should be corrected as,

$$L=(2/\pi)bC_0N_A V/\lambda_s^3$$

For PAMPS-1 sample,  $\lambda_s=4.5$  and  $b=0.25$  nm. In this experiment, the view field has a volume of  $896\times 896\times 100\text{ nm}^3 = 8.0\times 10^{-20}\text{ m}^3$ . Thus, the theoretical network strand contour length, including the loops and dangling chains, is estimated as  $L=8.4\times 10^4$  nm.

## 4.3 Results and discussion

### 4.3.1. Strategy to Prepare TEM Samples of Network Polymers

We chose a negatively charged polyelectrolyte network as our target network for two purposes. One is that by large osmotic pressure of its counter-ions, a polyelectrolyte network swells in low ionic strength aqueous solution to spontaneously achieve the pre-stretched state of the polymer strands. The other is that the network can be selectively stained through inhomogeneous nucleation by ionic complexation between the negative charges of the polymer strands and multi-valent metal ions. To hold the pre-stretched state during ionic staining and the afterward sample preparation process, we introduce a neutral polymer network of dense concentration, using the double network technique<sup>[6,22,23]</sup>.

When the concentration of the neutral polymer introduced is high enough, it generates an osmotic pressure as high as that of the polyelectrolyte network. As a result, the neutral network works as a skeleton to fully prevent the shrinkage of the polyelectrolyte strands in ionic staining solution through topological interpenetration with the neutral network<sup>[27]</sup>. Thereby, we can preserve the topological structure feature of the target network at a length scale larger than the mesh size of the neutral network. On the other hand, we expect that the conformation changes of the polyelectrolyte strands at a length scale smaller than the mesh size of the neutral network is allowable, which favours complexation of the target polymer with multi-valent ions for staining (**Figure 4.2**).

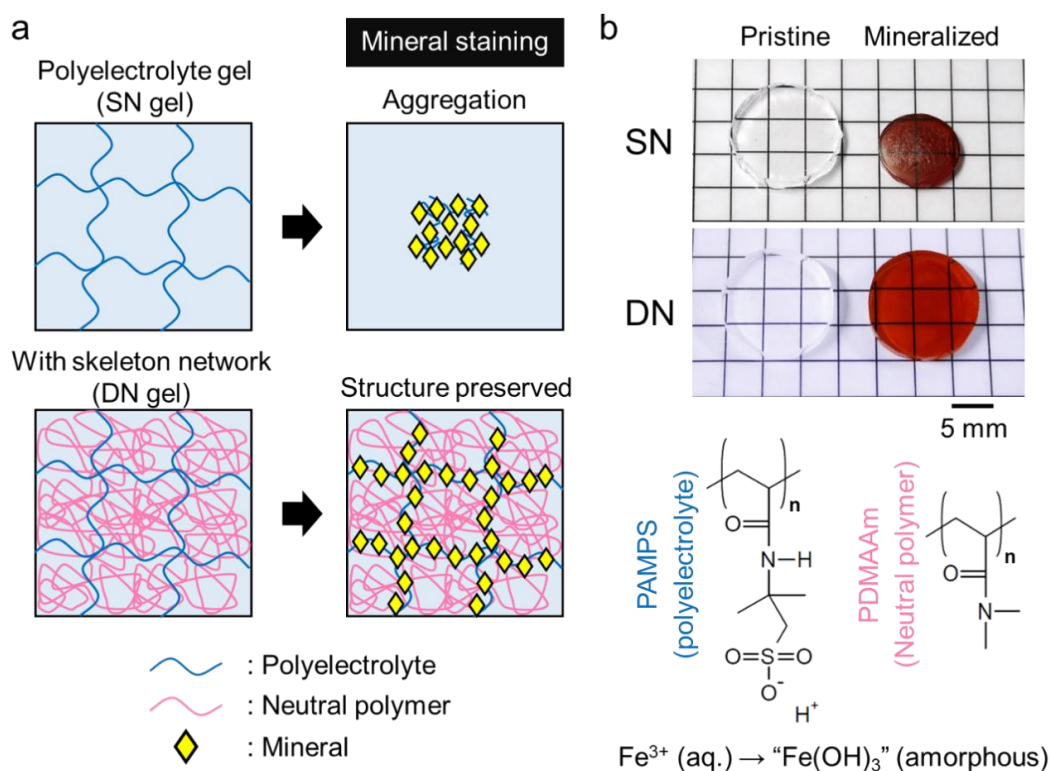


**Figure 4.2** (a) Schematic illustration of the double-network method to stain a polyelectrolyte hydrogel without causing a collapse of the polymer network strands. (b) Appearance of the PAMPS-4 single

network gel (SN) and double-network gel (DN) with poly(dimethylacrylamide) (PDMAAm) before and after mineral staining (upper), and chemical structure of PAMPS and PDMAAm, and the mineralization reaction during staining (lower).

Specifically, we adopted poly(2-acrylamido-2-methyl propanesulfonic acid) (PAMPS) network synthesized by free radical polymerization as the target network. For the neutral polymer network to hold the prestretched state of the target network, we adopted poly(dimethylacrylamide) (PDMAAm) since it maintains the sample size not only during the staining but also during the resin exchange process afterward. To selectively stain the target polyelectrolyte network with enough electronic contrast, we adopted  $\text{Fe}^{3+}$  that forms amorphous ferric oxide (AFO) nanoparticles through heterogeneous nucleation on the sulfonic acid groups of PAMPS chains [28].

The PAMPS networks exhibit an excess swelling in water and in the PDMAAm skeleton. Depending on the chemical crosslinking density, the sample thickness swelling ratio in relative to its initial thickness at synthesis is  $\lambda_s=4.5 \sim 1.7$ . By swelling, the PAMPS polymer weight fraction was as low as 0.3–5 wt.% in relative to water. Owing to the presence of the skeleton network PDMAAm, the shrinking of the PAMPS network during AFO staining is suppressed, as confirmed by the small change in sample size (**Figure 4.2b**). On the other hand, direct staining of AFO on a water swollen PAMPS network in the absence of the skeleton network caused the collapse and aggregation of the PAMPS

network (**Figure 4.2b**). PDMAAm can maintain approximately the same volume of the specimen even in the resin solution for substitution. As a result, the final thickness change in relative to their water swollen state is less than 10% for all PAMPS gel samples prepared with different formulations (**Figure 4.1**). Therefore, the prestretched state of the PAMPS network was almost maintained in the TEM specimen.

#### 4.3.2. Nanoscale TEM observation of the network

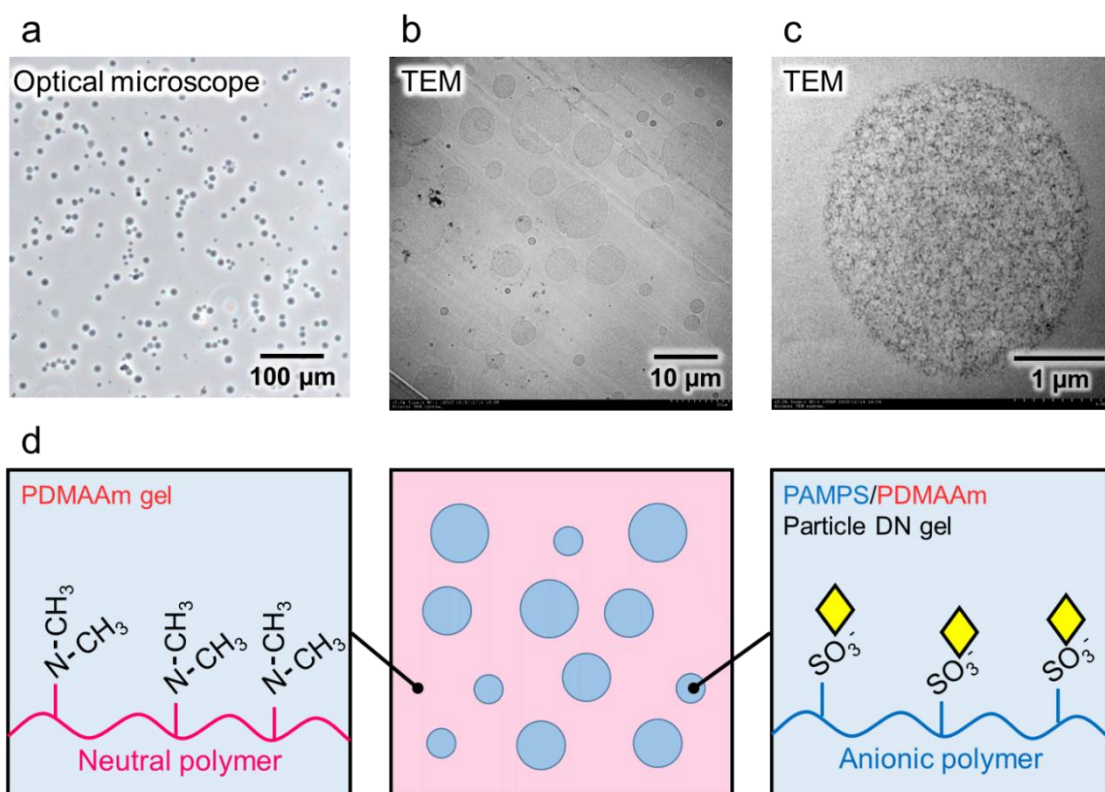


**Figure 4.3** TEM image of the PAMPS-4 micro particles swollen in the bulk PDMAAm gel. (a) Optical microscopy image of the pristine PAMPS micro-gel particles. (b) Low magnification ( $\times 300$ ) TEM image. (c) High magnification ( $\times 5000$ ) TEM image. (d) Schematic illustration of (b).

To confirm that AFO selectively mineralized only the PAMPS network, we first performed the TEM observation on the PAMPS micro-gels embedded in the bulk PDMAAm gel matrix [25]. **Figure 4.3** shows the optical microscopic image of the PAMPS micro-gels, TEM images of PAMPS micro-gels in the PDMAAm gel, and their corresponding schematic illustrations. The PAMPS micro-gels before mineralization (not shown in the figure) are unseen by TEM, while spherical micro-gels with several micrometer diameters are clearly identified after mineralization. This confirms that AFO selectively stained the PAMPS network, but not the PDMAAm network since the sulfonic group of PAMPS can catalyse the AFO deposition.

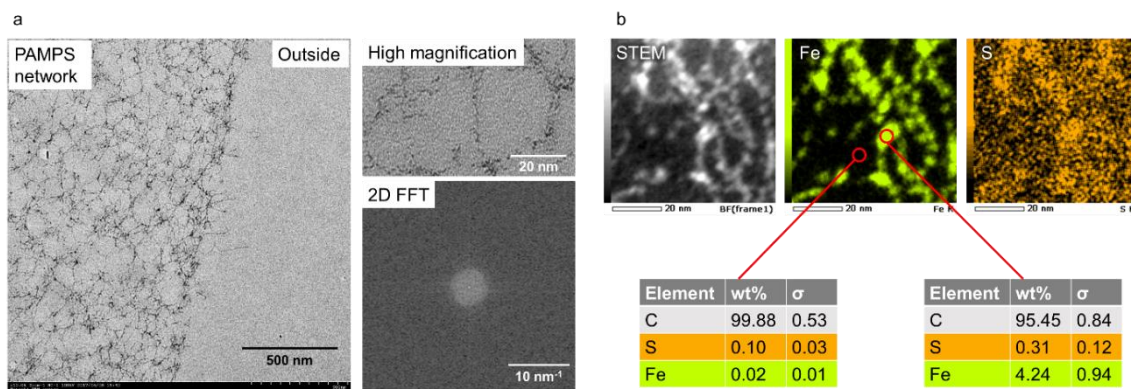


**Figure 4.4** (a) Low and high magnification TEM images of the PAMPS gel and 2D FFT from a single mineral nanoparticle. (b) STEM elemental mapping of the PAMPS gel. Fe and S shows the iron in the ferric oxide nanoparticles and sulphur in the PAMPS gel network, respectively. A supermacroporous PAMPS gel with a wall thickness of approximately 10  $\mu\text{m}$  was used for the observation.

We prepared a supermacroporous sponge-like PAMPS sample comprising an interconnected

porous structure with  $\sim 10 \mu\text{m}$  gel walls<sup>20</sup>. In this sample, iron ions were supplied faster than that for nonporous gel, thereby ensures sufficient mineral staining to the PAMPS network. The TEM micrograph shows the fine network morphology of the PAMPS (**Figure 4.4a**). Under high magnification, it is clearly observed that AFO nanoparticles with a diameter of several nanometers in network structure with a mesh size of several tens of nanometers.

The two-dimensional Fourier transform image of a single nanoparticle has no obvious peaks (lower right in **Figure 4.4a**), indicating its amorphous nature. Furthermore, 3D TEM was performed to observe the 3D network structure<sup>[29]</sup>. 3D connections of the network is clearly observed. To authors' knowledge, this is the first 3D nanoscale direct observation of network structure for synthetic polymers. To prove that only the PAMPS network was stained at the nanoscale, element mapping (STEM-EDS) was carried out (**Figure 4.4b**). The positions of sulphur of PAMPS and iron of AFO overlap with each other on the nanoscale, confirming that only the PAMPS network was selectively stained with ferric oxide.

Sample	$E_{\text{as-pre}}$ (MPa)	$\lambda_{s,w}(\frac{\dot{\gamma}}{T/T_0})$	$\xi$ (nm)
PAMPS-1	0.01	4.5	51
PAMPS-2	0.03	3.2	26
PAMPS-3	0.04	2.6	17
PDMAAm	0.02	-	8

**Table 4.1.** Thickness swelling ratio of PAMPS network in water ( $\lambda_{s,w}$ ) for TEM observation in relative to their as-synthesized state. The average mesh size  $\xi$  of PAMPS and PDMAAm network at TEM observation estimated from elastic modulus of networks.

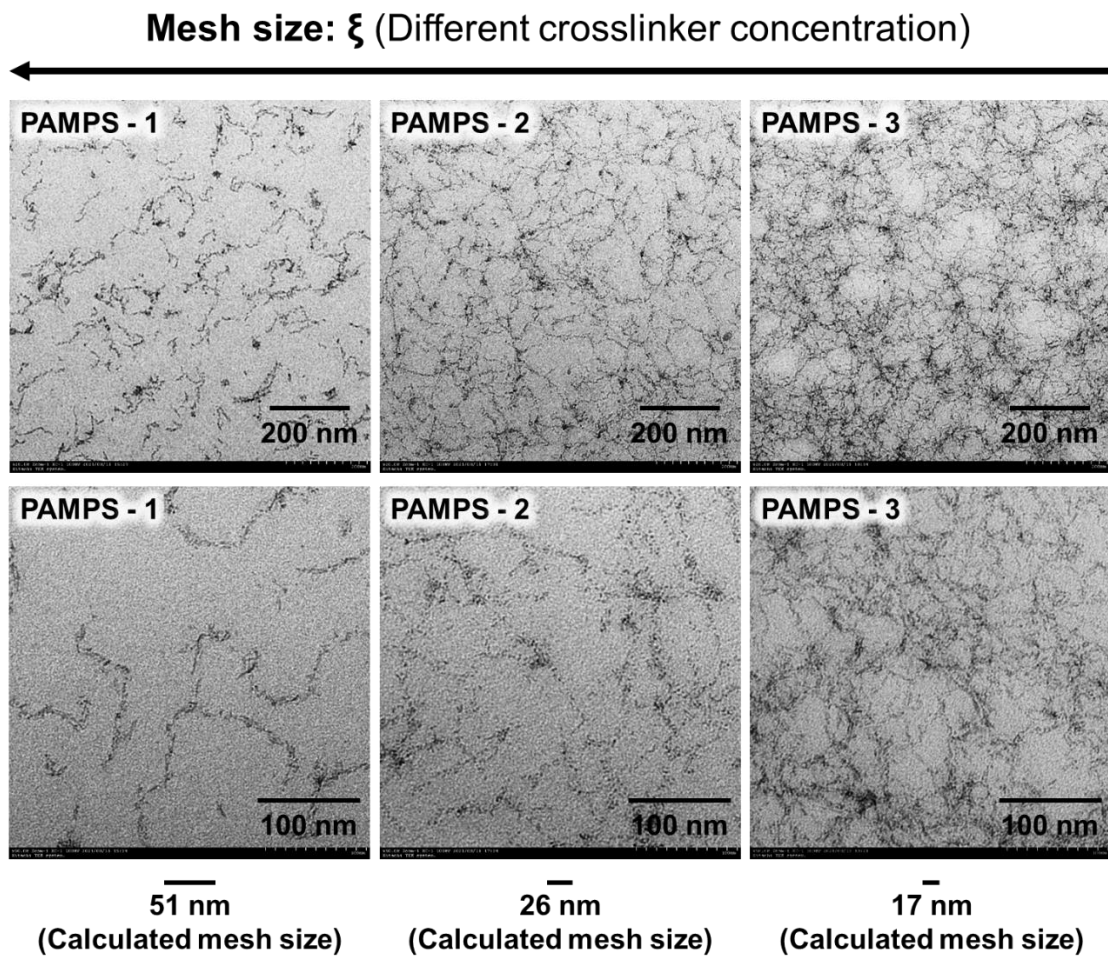


**Figure 4.5** Effect of crosslinker ratio of the PAMPS gels. Low magnification (Upper) and High magnification (Lower) TEM images. Lowest bars represent calculated mesh size from rubber elastic theory.

The TEM images of the PAMPS networks prepared with different crosslinker ratios are shown in **Figure 4.5**. The increase of the crosslinker ratio results in decrease of mesh size in TEM images, which is clearly seen. Here, we qualitatively compared the mesh size observed from TEM images with that calculated from Young's modulus of the bulk samples (**Table 4.1 and Figure 4.5**). The values estimated from the Young's modulus of the bulk samples represent the average mesh size of the elastically active strands<sup>[13]</sup>. The calculated mesh sizes at the pre-stretch state, assuming each elastically active strand has energy of  $k_B T$  in as-prepared state (**Table 4.1**), were almost half of the mesh size visible in TEM images. This result indicates that observed network structure was almost perfectly matched with rubber elastic theory prediction. We considered that the smaller mesh size estimated from rubber elasticity theory might indicate that each polymer strand has a larger energy than  $k_B T$  even at the as-prepared state since the PAMPS network was synthesized in water that is a good solvent. These results demonstrate that we achieved the direct observation of elastic network structure for the first time.

As discussed at the previous section, the conformation of the polymer strands should be maintained at a length scale larger than the mesh size of skeleton network by physical entanglement with the skeleton network, while the conformation at the scale smaller than the skeleton mesh size should be not true, due to aggregation during staining and later sample preparation process. Since the mesh sizes of these PAMPS networks (tens nm) are enough larger than that of skeleton network  $\xi_s$  (8



nm, **Table 4.1**), TEM images should represent unperturbed polymer strands conformation at a scale larger than 8 nm. Moreover, relatively short dangling chains which cannot entangle with skeleton network takes collapsed conformation and could not be observed. To discuss the latter aspect, we estimate the accumulate length of the polymer strands observed in TEM image, using PAMPS-1 sample as an example. The high magnification TEM observation of the PAMPS-1 is shown in **Figure**

4.6.

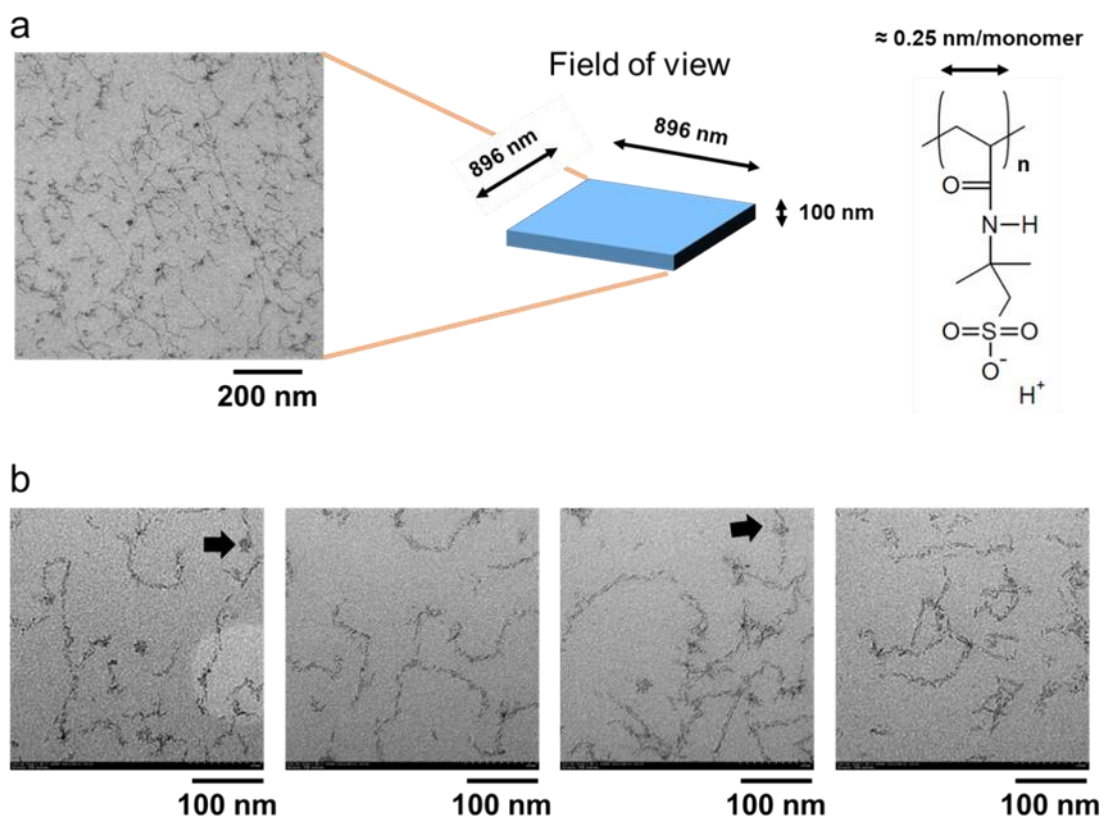


**Figure 4.6** (a) Calculation process of the polymer length in the field of view for the PAMPS-1 gel. (b)

High magnification TEM images of the PAMPS network at different locations. The mesh structures sized in tens to hundreds of nanometres were clearly observed. The black arrows indicate the apparent

aggregated dangling chains in the structure.

A fine PAMPS network morphology with the mesh sized in hundred nanometer is observed. The discontinuity of the network can be attributed to the mesh structure that is frequently larger than thickness of the specimen (100 nm). The accumulative strand length in the volume of the measured view ( $896 \times 896 \times 100 \text{ nm}^3$ ) is estimated as  $17700 \pm 2700 \text{ nm}$  from TEM images (See section 4.2.5). Since the polymer strands at scale smaller than the mesh size of the skeleton  $\xi_s$  should have been collapsed by staining, this accumulative strand length does not stand for the contour length of the crosslinked strands. Here we made corrections by estimating the ratio of skeleton mesh size  $\xi_s$  and the contour length before staining  $L_m$  in a skeleton mesh,  $\xi_s/L_m$ . The end-to-end distance  $R_m$  of the target strands in each skeleton mesh before staining equals to skeleton mesh size  $\xi_s$ :  $\xi_s = R_m$ . On the other hand, the corresponding value at the as-prepared state  $R_{m0}$  is  $R_m = \lambda_s R_{m0} = \lambda_s b N_m^{1/2}$ . Assuming that the contour length  $L_m = b N_m$  collapsed to mesh size of the skeleton  $\xi_s$  during staining, the ratio of skeleton mesh size  $\xi_s$  to the contour length of the target polymer in the mesh  $b N_m$  gives the fraction of shrinkage;  $\xi_s/L_m = \lambda_s^2 b / \xi_s$ . Using  $\lambda_s = 4.5$ ,  $b = 0.25 \text{ nm}$ ,  $\xi_s = 8 \text{ nm}$ , we have  $\xi_s/b N_m = 0.63$ . Using this factor, we have a correct accumulative strand length of  $17700 \pm 2700 \text{ nm} / 0.63$ . This value is approximately 1/3 of the total length of polymer  $8.4 \times 10^4 \text{ nm}$  calculated from the amount of PAMPS monomer unit in the viewing volume (Figure 4.6a). The result suggests that dangling chains are in collapsed state

and their size could not be observed by this method.

#### 4.3.3 Surface structure of network

The surface feature, such as low friction, adhesions, and permeability for small molecules and ions, is an important characteristic of hydrogel materials. In nature, hyaline cartilage exhibits both incredibly low friction property and semipermeability that allows nutrient diffusion<sup>[30,31]</sup>. The TEM observation of the specimen prepared by our method for the first time revealed the precise structure of the polymer strands at the hydrogel surface.

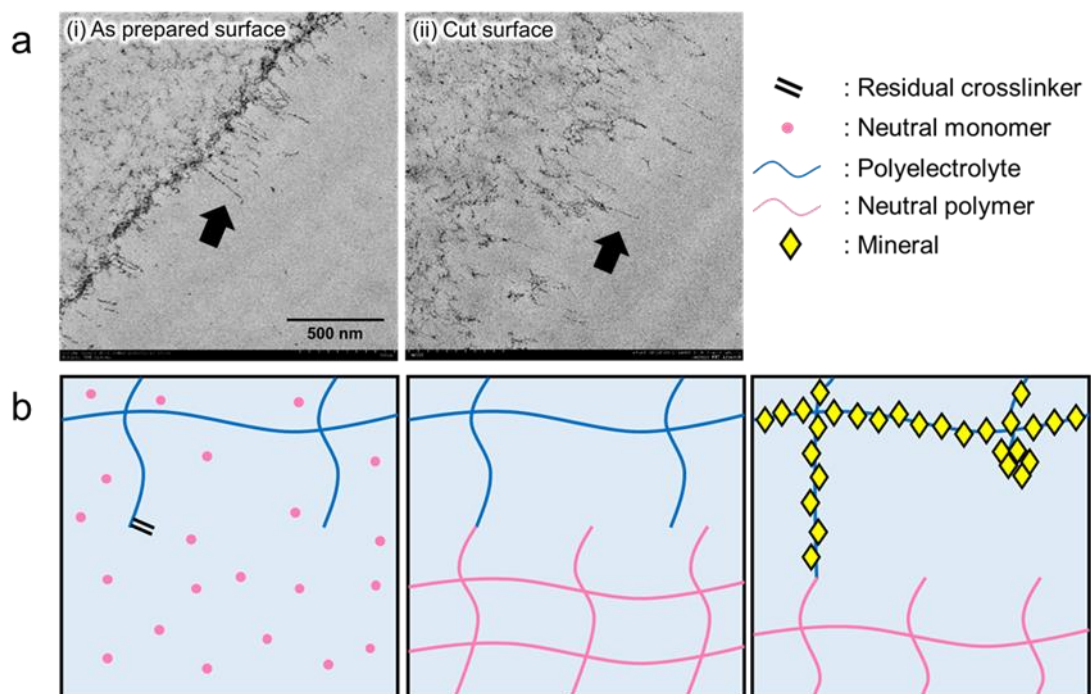


**Figure 4.7** Surface network structure of the PAMPS-4 gel. (a) (i) As-prepared gel surface synthesized on a flat glass mold; (ii) Surface cut with a microtome knife. The black arrows in the TEM images

indicate surface dangling chains. (b) Schematic of the surface dangling chain extension by the skeleton network. The PDMAAm network in the PAMPS gel was omitted for schematic visibility.

**Figure 4.7a(i)** shows the outermost as-prepared surface of a PAMPS-4 hydrogel synthesized on a flat glass mold. PDMAAm was induced by second polymerization with the method described in the previous section. Several hundred nanometer-sized dangling chains (indicated by the black arrows) in the fully elongated state from the bulk region are observed. These surface dangling chains do not collapse as they are covalently connected to the PDMAAm network and are stretched by its swelling (**Figure 4.7a(i)**). As illustrated in **Figure 4.7b**, the PAMPS network usually has a few unreacted vinyl groups after PAMPS polymerization<sup>[32]</sup>. During the polymerization of the second skeleton network, some dangling chains with remaining vinyl groups on the PAMPS gel surface are incorporated into the PDMAAm network. Furthermore, the chemical components in the topmost surface layers of DN hydrogels prepared by a two-step sequential polymerization depends on the mold used for the synthesis. In the case of a PAMPS network imbedded in the neutral second network prepared on glass molds, the sample surface is covered by a layer of the neutral second network of several micrometers-thick due to counter-ion osmotic repulsion between the PAMPS and glass that are both negatively charged in water.<sup>[33]</sup> In fact, the neutral PDMAAm layer is clearly seen on the topmost surface of PAMPS gel/PDMAAm specimen in a TEM image of low magnification (**Fig. S4**).

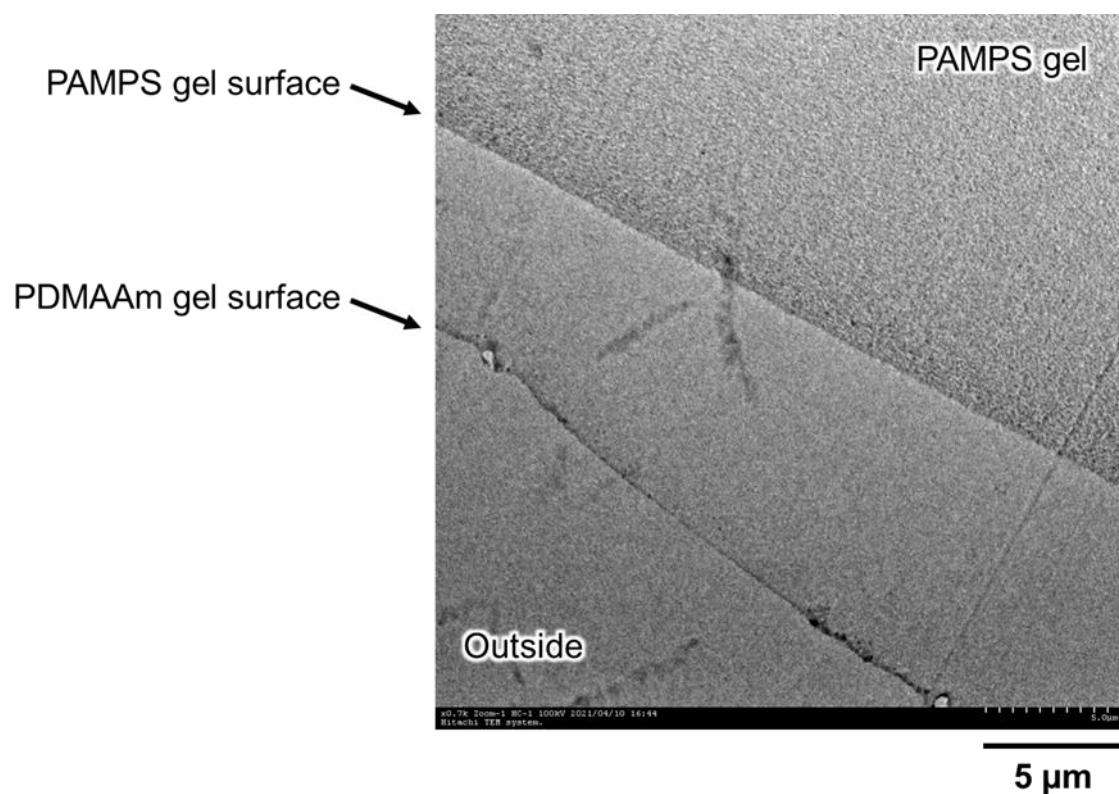


**Figure 4.8** Low magnification TEM image of PAMPS-3 surface. PAMPS network in swollen state is clearly stained by AFO. PDMAAm gel surface is also visible due to some AFO particles, which mineralized at outside of gel and precipitated on gel surface. The thickness of the PDMAAm network layer swollen in water varies depending on the location (usually layer thickness is 5 to 20  $\mu\text{m}$ ).

Therefore, the surface of the formed PAMPS/PDMAAm DN hydrogel is covered by the second PDMAAm network partially connected with the PAMPS dangling chains<sup>[34]</sup>. The immersion of the PAMPS/PDMAAm gel in water induces the swelling of the PDMAAm network surface layer towards the thickness direction since the lateral direction is confined by the already highly stretched PAMPS network. As a result, the PAMPS strands connected to the PDMAAm are stretched in the direction

vertical to the PAMPS network surface. In **Figure 4.7a(i)**, the approximate length of the dangling chains (several hundred nanometers) is approximately equal as that of the network mesh size in the bulk region. Therefore, these dangling strands can be assumed to be strands that could not find a cross-linking partner at one end. In addition, this result indicates that the length of the surface dangling chain of the chemically crosslinked network is comparable to the bulk network mesh size; thus, the length of the dangling chains of the gel surface can be estimated based on the mesh size of the bulk network. It should be noted that only dangling chains that are covalently connected to the second network are observed as elongated strands. As most dangling chains are not covalently connected to the second network, they collapsed into a globule conformation, as seen by the dark rough line on the gel surface, similar with the dangling chains inside the gel (**Figure 4.6b**).

We also observed the surface of the PAMPS gel cut using a fine microtome knife with an edge thickness of 76  $\mu\text{m}$ . The cut surface is significantly rougher than the as-prepared surface (**Figure 4.7a(ii)**). In addition, it has a disordered network structure approximately 1  $\mu\text{m}$  deep from the outermost surface, while the mesh structure is maintained in the inner region. The length of the created dangling chains at the surface is nearly equal to the bulk mesh size since these dangling chains are originated from the mesh. Considering that cutting creates two fracture surfaces, the damage zone has a total depth of approximately 2  $\mu\text{m}$ , suggesting that brittle hydrogel is fractured near the surface, despite the cutting edge thickness of 76  $\mu\text{m}$ . This observation can be used to estimate the relation

between the microscale damage zone and macroscopic fracture.

#### 4.3.4. Heterogeneity of the network

The characterisation of the defects or heterogeneity is vital in understanding the fracture of the material as it is governed by local structure, not by the average structure<sup>[35,36]</sup>. Particularly, fracture is always originated in the largest defect in a material. Here, we applied the developed method to directly observe the defects in hydrogels.

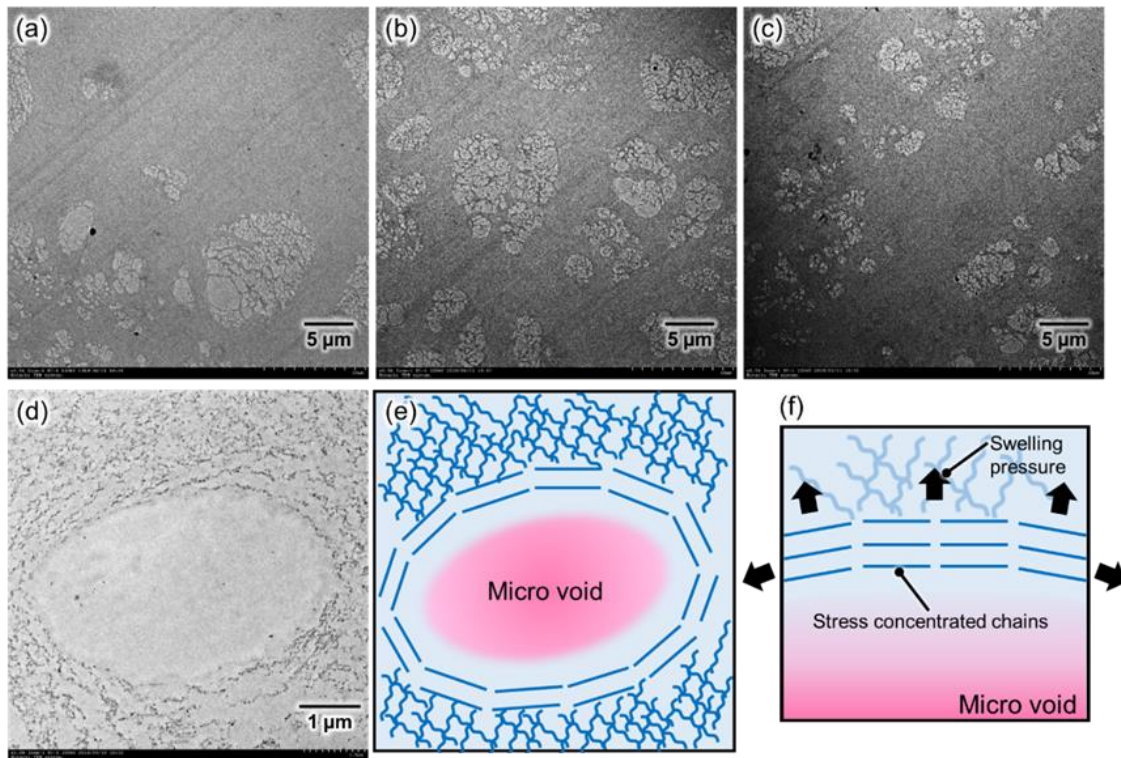


**Figure 4.9** Micro-scale network defects in the bulk PAMPS-4 gel. (a)–(c) Low magnification TEM images at different locations. The white areas are microvoids without a PAMPS network. (d)–(f) High

magnification TEM image around a microvoid and its schematic illustration.

**Figure 4.9** shows the TEM images of a bulk PAMPS-4 hydrogel with PDMAAm skeleton network and its schematic illustrations. The PAMPS hydrogel contains several local voids that are approximately 10  $\mu\text{m}$  (**Figure 4.9a–c**). These voids do not have a PAMPS network. The origin of defects is the nonhomogeneous formation of the micro-gels<sup>[8,37]</sup>. In the initial stage of hydrogel polymerization from the monomer and crosslinker, several micro-gels are instantaneously formed with non-uniform spacing. When these microgels grow and coalesce together to form the bulk gel, a void structure is formed where there are no micro-gels. These micro-scale defects are not observed in small particle gels with a diameter of several micrometers (**Figure 4.3**). Hence, a small gel is relatively homogeneous and free of large defects, while defect formation is inevitable for a bulk gel, thereby affecting its mechanical properties. TEM observation allows a simultaneous observation of the hydrogel structure at multiple scales. **Figure 4.9d–f** shows a high magnification image of a void and its schematic illustrations. Polymer strands around the void are oriented along the defect circumference, indicating that these strands are highly elongated than those farther from the voids. This result denotes that microscale heterogeneity, such as voids, induces nanoscale heterogeneity. Note that these micro voids are not always generate, depending on polymerization rate and gel composition.



#### 4.4 Conclusions

We demonstrated the combination of a novel staining method with DN technique to directly observe a rubber elastic polyelectrolyte hydrogel network at the nanoscale level. The molecular structure of rubber elastic hydrogel in bulk and on the surface was unveiled for the first time in real space. Observed mesh sizes were almost agreed with rubber elastic theory prediction. We clarified the presence of dangling chains on the surface of the as-prepared gels with a length on the same scale as the mesh size. These results are important in understanding the surface properties of hydrogels, including surface wetting–dewetting, sliding friction, adhesion, and bonding. Furthermore, numerous micro-scale defects noted in these gels can induce stress concentration of the nanoscale polymer strands. These results are essential in understanding the origin of the brittleness of hydrogels. This method has the potential to give wide knowledge not only for hydrogels but also for nano scale structure of rubbery materials.

#### 4.5 References

- [1] O. Erol, A. Pantula, W. Liu, D. H. Gracias, *Adv. Mater. Technol.* **2019**, *4*, 1.
- [2] J. P. Gong, *Soft Matter* **2006**, *2*, 544.
- [3] R. A. Green, S. Baek, L. A. Poole-Warren, P. J. Martens, *Sci. Technol. Adv. Mater.* **2010**, *11*, DOI 10.1088/1468-6996/11/1/014107.

- [4] A. S. Hoffman, *Adv. Drug Deliv. Rev.* **2012**, *64*, 18.
- [5] K. Y. Lee, D. J. Mooney, *Chem. Rev.* **2001**, *101*, 1869.
- [6] K. Yasuda, N. Kitamura, J. P. Gong, K. Arakaki, H. J. Kwon, S. Onodera, Y. M. Chen, T. Kurokawa, F. Kanaya, Y. Ohmiya, Y. Osada, *Macromol. Biosci.* **2009**, *9*, 307.
- [7] J. Bastide, L. Leibler, *Macromolecules* **1988**, *21*, 2647.
- [8] S. Seiffert, *Polym. Chem.* **2017**, *8*, 4472.
- [9] K. Nishi, M. Chijiishi, Y. Katsumoto, T. Nakao, K. Fujii, *J. Chem. Phys.* **2012**, *137*, 224903.
- [10] M. Shibayama, A. M. Shibayama, T. Norisuye, *Bull. Chem. Soc. Jpn* **2002**, *75*, 641.
- [11] M. Shibayama, *Bull. Chem. Soc. Jpn.* **2006**, *79*, 1799.
- [12] T. Tominaga, V. R. Tirumala, E. K. Lin, J. Ping, H. Furukawa, Y. Osada, W. Wu, *Polymer (Guildf)*. **2007**, *48*, 7449.
- [13] K. Fukao, T. Nakajima, T. Nonoyama, T. Kurokawa, T. Kawai, J. P. Gong, *Macromolecules* **2020**, *53*, 1154.
- [14] M. Iijima, M. Shinozaki, T. Hatakeyama, M. Takahashi, H. Hatakeyama, *Carbohydr. Polym.* **2007**, *68*, 701.
- [15] F. Gentile, M. Moretti, T. Limongi, A. Falqui, G. Bertoni, A. Scarpellini, S. Santoriello, L. Maragliano, R. P. Zaccaria, E. Fabrizio, **2012**, 10.
- [16] G. R. Newman, B. Jasani, E. D. Williams, *Histochem. J.* **1983**, *15*, 543.

- [17] N. A. Ranson, P. G. Stockley, *Emerg. Top. Phys. Virol.* **2010**, 1.
- [18] R. Vitali, E. Montani, *Polymer (Guildf)*. **1980**, 21, 1220.
- [19] H. Jinnai, T. Higuchi, X. Zhuge, A. Kumamoto, K. J. Batenburg, Y. Ikuhara, *Acc. Chem. Res.* **2017**, 50, 1293.
- [20] R. Aso, H. Kurata, T. Namikoshi, T. Hashimoto, S. W. Kuo, F. C. Chang, H. Hasegawa, M. Tsujimoto, M. Takano, S. Isoda, *Macromolecules* **2013**, 46, 8589.
- [21] M. Tosaka, R. Danev, K. Nagayama, *Macromolecules* **2005**, 38, 7884.
- [22] J. Gong, Y. Katsuyama, T. Kurokawa, Y. Osada, *Adv. Mater.* **2003**, 15, 1155.
- [23] J. P. Gong, *Soft Matter* **2010**, 6, 2583.
- [24] T. Sedlačik, H. Guo, T. Nonoyama, T. Nakajima, T. Kurokawa, J. P. Gong, *Chem. Mater.* **2020**, 32, 8576.
- [25] J. Hu, K. Hiwatashi, T. Kurokawa, S. M. Liang, Z. L. Wu, J. P. Gong, *Macromolecules* **2011**, 44, 7775.
- [26] C. A. Schneider, W. S. Rasband, K. W. Eliceiri, *Nat. Methods* **2012**, 9, 671.
- [27] T. Nakajima, T. Nakajima, T. Nakajima, T. Chida, K. Mito, T. Kurokawa, T. Kurokawa, J. P. Gong, J. P. Gong, J. P. Gong, *Soft Matter* **2020**, 16, 5487.
- [28] C. M. Flynn, *Chem. Rev.* **1984**, 84, 31.
- [29] H. Jinnai, R. J. Spontak, T. Nishi, *Macromolecules* **2010**, 43, 1675.

- [30] J. Katta, Z. Jin, E. Ingham, J. Fisher, *Med. Eng. Phys.* **2008**, *30*, 1349.
- [31] A. Jackson, W. Gu, *Curr. Rheumatol. Rev.* **2009**, *5*, 40.
- [32] T. Nakajima, H. Furukawa, Y. Tanaka, T. Kurokawa, Y. Osada, J. P. Gong, *Macromolecules* **2009**, *42*, 2184.
- [33] M. Frauenlob, D. R. King, H. Guo, S. Ishihara, M. Tsuda, T. Kurokawa, H. Haga, S. Tanaka, J. P. Gong, *Macromolecules* **2019**, DOI 10.1021/acs.macromol.9b01399.
- [34] M. Frauenlob, D. R. King, H. Guo, S. Ishihara, M. Tsuda, T. Kurokawa, H. Haga, S. Tanaka, J. P. Gong, *Macromolecules* **2019**, *52*, 6704.
- [35] A. A. Griffith, *Masinovedenie* **1995**, *C*, 163.
- [36] M. Marder, J. Fineberg, *Phys. Today* **1996**, *49*, 24.
- [37] N. Ide, T. Fukuda, *Macromolecules* **1999**, *32*, 95.

# CHAPTER 5

## Fractographic Analysis on Non-linear Elastic Hydrogels

### 5.1 Introduction

Non-linear elastic materials such as rubber, elastomer, and hydrogel, which show soft and stretchable feature, have been expected to apply widely for soft robotics, stretchable electronics, and tissue engineering<sup>[1-6]</sup>. Especially, robust and tough hydrogels, invented recent 20 years, are one of promising materials for load-bearing and high-tensile biomaterials due to comparable mechanical properties to tissues and well-biocompatibility<sup>[7,8]</sup>. For practical use, a fracture analysis of hydrogel is indispensable to evaluate the load limit of bioimplants. The fracture mechanism of hard materials like ceramics and metals has been well-understood as linear elastic fracture mechanics (LEFM) resulting that a computer precisely estimates stress distribution and deformation on complexly geometric structure based on finite element methods, while the fracture mechanism of soft and non-linear elastic materials is still challenging field, and many studies have been performed to establish models estimating realistic fracture behavior<sup>[9]</sup>. For example, crack length dependence of fracture stress, crack-tip opening displacement (CTOD), and crack instability<sup>[10-13]</sup>

The analysis of fracture surface of material, called as fractography, is also one of major methods on failure analysis. **Fig. 5.1A** shows typical brittle fracture process of hard material. In tensile deformation, crack begins to progress from initial defect and pass through the material while

accelerating by using strain energy. Once crack reaches the upper limit velocity which is comparable to sonic speed traveling the material, multiple crack surfaces (crack branching) are generated to compensate excess strain energy instead of crack acceleration, resulting that the fracture surface shows a characteristic geometry with smoothly circular face centered on the starting point of fracture and radially rough face on the outer side of the smooth circle. A smooth region before the crack branching is called mirror surface, and a rough region after crack branching is called mist-hackle surface. The radius of smooth circle is called “mirror radius”, considered as a characteristic parameter related to fracture mechanism<sup>[14-16]</sup>. For linear elastic materials, mirror radius is correlated to fracture stress ( $\sigma_F$ ) and critical stress intensity factor ( $K_{IC}$ ), representing the stress distribution in front of crack. X

For nonlinear elastic materials, they have different stress distribution from the linear elastic materials<sup>[11]</sup>. To investigate it, we decided to apply super tough hydrogel. The super tough Double Network (DN) hydrogel is the most suitable material for the mirror radius observation because it shows brittle fracture, negligible viscosity, and relatively high fracture stress among non-linear elastic materials<sup>[7,8]</sup>.

In this study, we confirmed semi-circular mirror region and mist-hackle region on the fracture surface of nonlinear elastic hydrogel. We also find the new semi-empirical power law of -1 between fracture stress and mirror radius ( $r$ ).

$$\sigma_F = A \cdot r^{-1}$$

In this equation, material constant ( $A$ ) has the same dimensions with the stress intensity factor

( $J$ ) of non-linear elastic material.

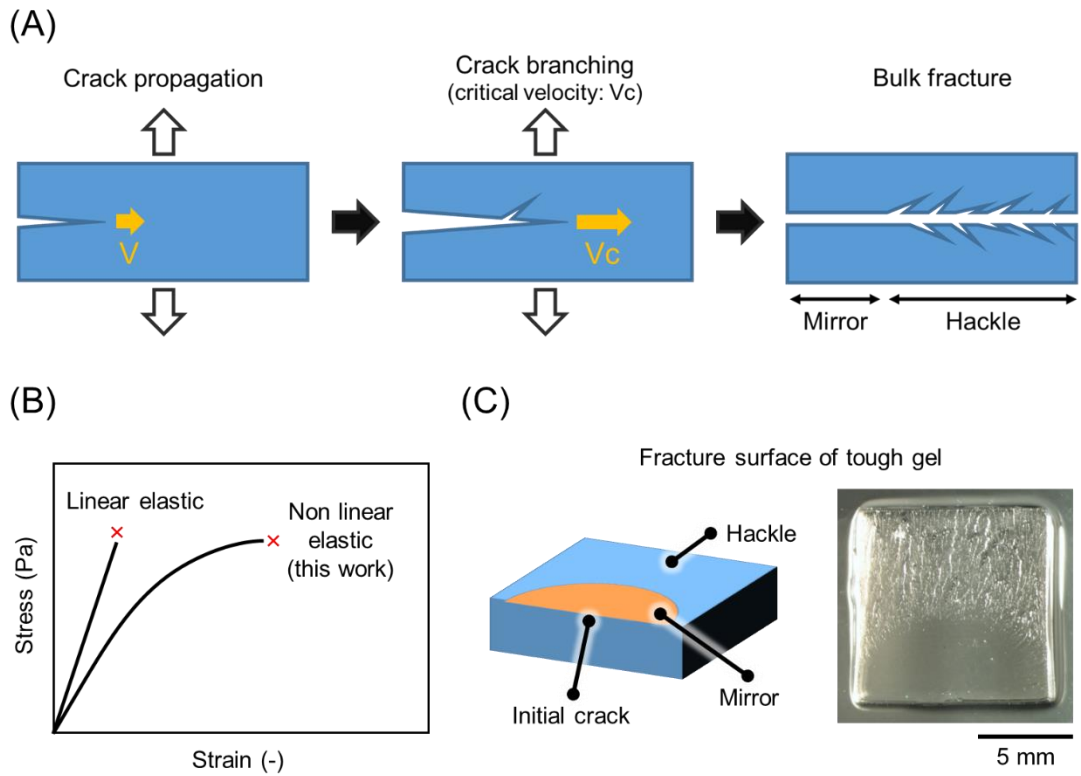


**Fig. 5.1** Brittle fracture process. (A) Schematic illustration of crack propagation process in brittle material under tensile deformation. (B) Stress-Strain curves of typical linear and non-linear elastic materials. (C) Schematic brittle fracture surface (left), and tensile fracture surface of tough DN hydrogel (1-8-0.1, 4-0.1-0.1) (right). This DN gel showed a typical brittle fracture surface.

## 5.2 Experiments

### 5.2.1 Materials

2-Acrylamido-2-methyl propanesulfonic acid (AMPS: monomer) was provided from Toagosei Co. Ltd, Japan. Dimethylacrylamide (DMAAm: monomer), *N, N'*-methylenebisacrylamide (MBAA: crosslinker), 2-oxoglutaric acid ( $\alpha$ -keto: initiator), and iron (III) chloride hexahydrate were purchased from Wako Pure Chemical Ind., Ltd., Japan. All chemicals were used as received.

### 5.2.2 Gel synthesis

The PAMPS/PDMAAm DN gel was synthesized following our previously reported protocol. First, PAMPS gel was synthesized by UV radical polymerization in a mold made from a silicone spacer sandwiched by two glass plates. UV irradiation time was 8 h and the mold was previously deoxidized overnight in an argon chamber. The composition of precursor solution was 1 mol/L AMPS as monomer, 2-8 mol% MBAA as a cross-linker, and 0.1 mol%  $\alpha$ -keto as an initiator. Then the PAMPS gel was removed from the mold and soaked into the PDMAAm network precursor solution containing 1-4 mol/L DMAAm, 0.1 mol% MBAA, and 0.1 mol%  $\alpha$ -keto until equilibrium for one day. We call gels as (1<sup>st</sup> monomer mol/L)-(1<sup>st</sup> crosslinker mol%)-(1<sup>st</sup> initiator mol%), (2<sup>nd</sup> monomer mol/L)-(2<sup>nd</sup> crosslinker mol%)-(2<sup>nd</sup> initiator mol%) like 1-8-0.1, 2-0.1-0.1. The PAMPS gel containing the PDMAAm network precursor solution was sandwiched between two glass plates, and irradiated with UV for the 2<sup>nd</sup> polymerization for 6 h in Ar atmosphere. After polymerization, the DN gels were immediately used for experiment without water absorbing. The thicknesses of the DN gels were



adjusted to about 1 cm by adjusting the spacer thickness of the PAMPS mold. PAMPS 1-4-0.1 and PDMAAm 4-0.1-0.1 single network gels were synthesized by the same way and used in the experiment in the swollen and non-swelled states, respectively.

### 5.2.3 Tensile test

The tensile mechanical property of DN gels was examined by using a mechanical tester (Tensilon RTC-1310A, Orientec Co., Japan). The samples were cut in dumbbell shape (JIS K 6251, Type 2) by a programmed laser cutter (ULR-60, Universal Laser Systems, US). Then, we introduced triangular initial crack by using a fine microtome knife, whose edge thickness is 76  $\mu\text{m}$  (**Fig. 2B (i)**). Tensile test was performed at a speed of 100 mm/min with taking movie. After sample fracture, we immediately observed the tensile fracture surface and determined the mirror radius by measuring the distance from the initial crack to the hackle region. Each test was run on more than 10 samples.

The true fracture stress and true mirror radius were calculated as follows. Because gel is an incompressible material, its Poisson's ratio is 0.5. In that case, when the gel is stretched to strain  $\varepsilon$ , the length of each side of the cross section becomes  $1 / \sqrt{\varepsilon}$  times the original length. We obtained fracture strain  $\varepsilon_F$  by comparing the sample width before tension and immediately before fracture in the video.

Finally, we calculated the true fracture stress:  $\sigma_F = \frac{\text{Nominal } \sigma_F}{\varepsilon_F}$  and the true mirror radius:  $r =$

$$\frac{\text{Nominal } r}{\sqrt{\varepsilon_F}}.$$

#### ***5.2.4 Roughness observation by 3D laser microscope***

The line scanning image of fracture surface was obtained by 3D laser microscopy (VK-9710, KEYENCE, Japan). The wavelength of the laser light source was 408 nm. The roughness scan was made by taking a simple moving average of nine data points from the original data.

#### ***5.2.5 Roughness observation by transmission electron microscopy (TEM)***

For staining, the DN gel was immersed in staining solution 2.5 M FeCl<sub>3</sub> for one day in room temperature, and after that the gels were immersed in pure water to increase pH, amorphous ferric oxide nanoparticles were mineralized in the PAMPS network, especially near bulk surface. To observe surface morphology of stained hydrogel, we carried out TEM observation (H-7650, Hitachi, Japan). To prepare the specimen for TEM observation, the hydrogel was frozen in liquid nitrogen, and water in the hydrogel was exchanged to ethanol and then acrylic resin (London Resin white, medium) in a chamber of an automatic freeze substitution system (EM AFS2, Leica Microsystems, Germany). The final thickness change of the resin-cured specimen was within 10% in relative to that of the DN gel in water. Then, 100-nm thick sections of the resin-cured specimen were cut by an ultra-microtome (EM UC7i, Leica Microsystems, Germany) and placed on a carbon supported copper mesh grid. The acceleration voltage of the electron gun for observation was 100 kV.

### 5.3 Results & Discussion

#### 5.3.1 Mirror region formed by crack branching

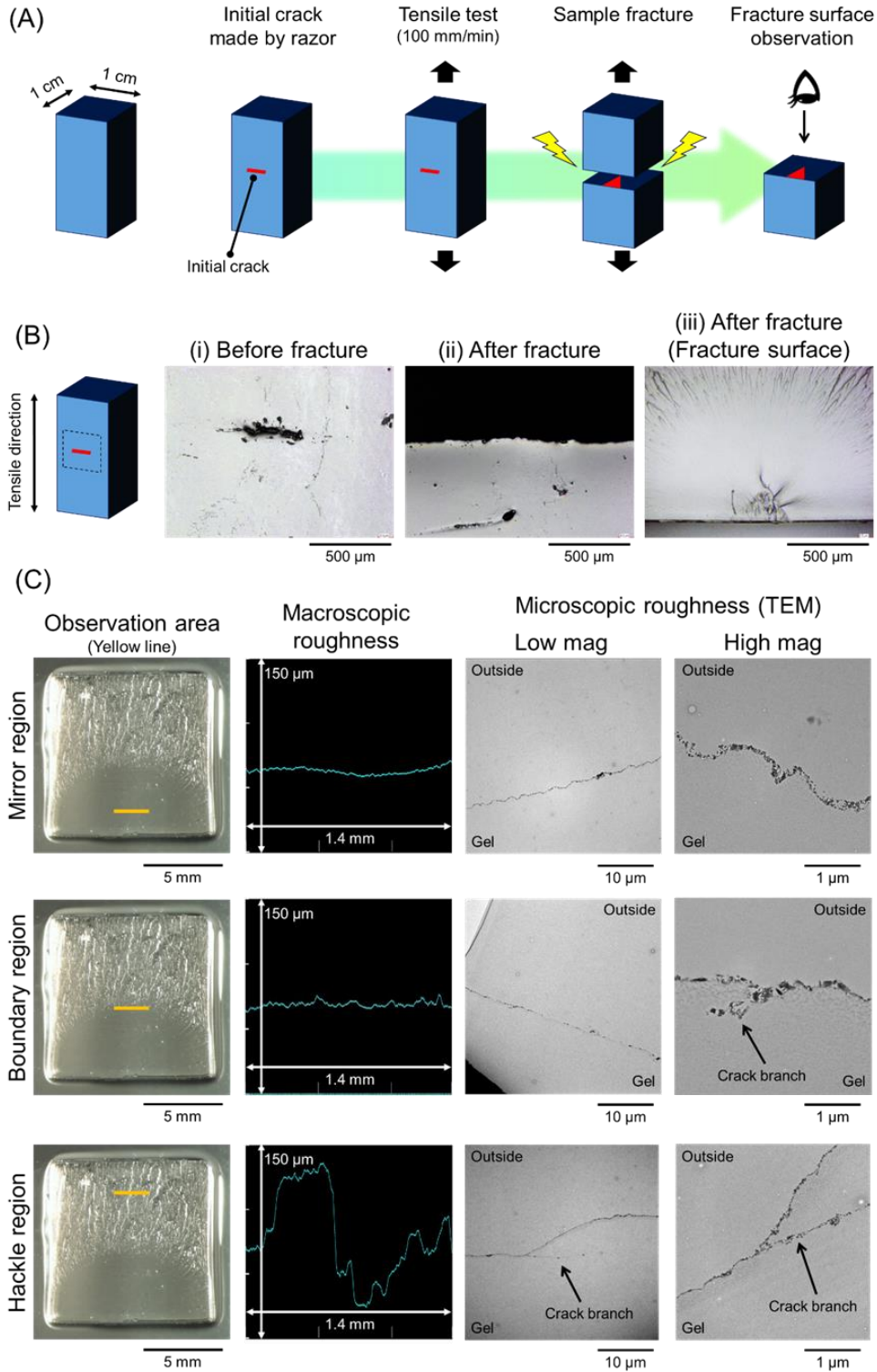


**Fig. 5.2** Fracture surface of tough DN gel. (A) Schematic diagram of the experimental method. (B) Appearance of tough gel. Side view of (i) before and (ii) after fracture. (iii) Fracture surface near initial crack. (C) Macro and micro roughness of fracture surface of tough gel. Macroscopic structure was observed by 3D laser microscope, and microscopic structure was observed by TEM. Yellow lines in the left photographs represent observation area of right pictures. Black arrows in the TEM images indicate branched crack.

**Fig. 5.2A** shows a schematic diagram of the experimental method. First, according to the procedure reported in the previous study, we synthesized conventional tough DN hydrogels consisting of poly(2-acrylamido-2-methyl propanesulfonic acid) as the brittle first network and poly(N,N-dimethylacrylamide) (PDMAAm) as the ductile second network, with different concentrations of 1<sup>st</sup> cross-linker and 2<sup>nd</sup> monomer. Other concentrations were fixed to 1 M 1<sup>st</sup> monomer, 0.1 mol% 1<sup>st</sup> and 2<sup>nd</sup> initiators, and 0.1 mol% 2<sup>nd</sup> cross-linker. The sample name was denoted as (1-C<sub>1</sub>-0.1, M<sub>2</sub>-0.1-0.1), whose C<sub>1</sub> and M<sub>2</sub> were concentrations of 1<sup>st</sup> cross-linker (mol% respect to 1<sup>st</sup> monomer concentration) and 2<sup>nd</sup> monomer (M), respectively. The sample was cut into a dumbbell shape with a central cross-section area of 1 cm × 1 cm, and an initial crack perpendicular to the tensile direction was introduced using a sharp knife. Then, tensile fracture was performed at 100 mm / min to generate fracture surface (Fig. 5.3). After fracture, the mirror radius of fracture surface was immediately measured by laser

microscope.

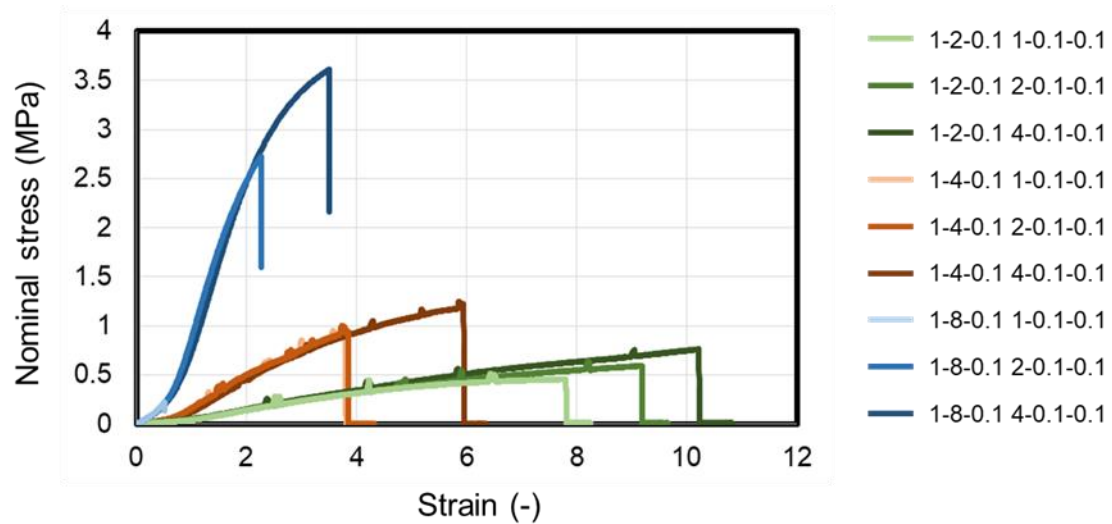


**Fig. 5.3** Stress-strain curves of PAMPS/PDMAAm DN gels.

In all gels, before fracture, the gel greatly deformed without crack growth, and once the crack began to grow, global fracture immediately occurred. Appearance of the sample side and fracture surface are shown in **Fig. 5.2B**. A smooth semi-circular mirror region was obviously formed centering on the initial crack, and a mist-hackle region with radial bumps was formed on the outer circumference. The boundary between the mist and the hackle was unclear and indistinguishable.

To confirm that the mist-hackle pattern on the fracture surface corresponds to crack branching, we observed microscopic structure of fracture surface of gel by using 3D laser microscope and transmission electron microscope (TEM) with interface staining (**Fig. 5.2C**). The mirror region near

the initial crack was flat in macro scale, and very small surface roughness was observed in TEM images. The boundary region was also flat in macro scale, but a shallow crack branching (black arrow in the TEM image) was observed. In the mist-hackle region, large crack branching from the main crack (black arrow in the TEM image) was observed, and on the macro scale, huge roughness formed by multiple crack branching.

From the above results, it was proved that brittle fracture with the crack branching occurred during fracture of tough DN gel, resulting that fracture surface formed mirror and mist-hackle regions.

### **5.3.2 Relationship between mirror radius and fracture stress**

Based on the tensile fracture tests, the relation between mirror radius and fracture stress was evaluated. **Fig. 5.4** shows the double logarithmic plot against the fracture stress ( $\sigma_F$ ) and the mirror radius ( $r$ ) of tough gel (1-8-0.1, 2-0.1-0.1). The variation using single composition of DN gel was obtained by changing size of initial crack. In this study, the true fracture stress and the true mirror radius were calculated by using cross sectional area of the sample just before the tensile fracture. The samples with higher  $\sigma_F$  show smaller mirror radius and samples with lower  $\sigma_F$  show bigger mirror radius. This relationship was well-approximated by a negative power law with a slope of about -1.2.

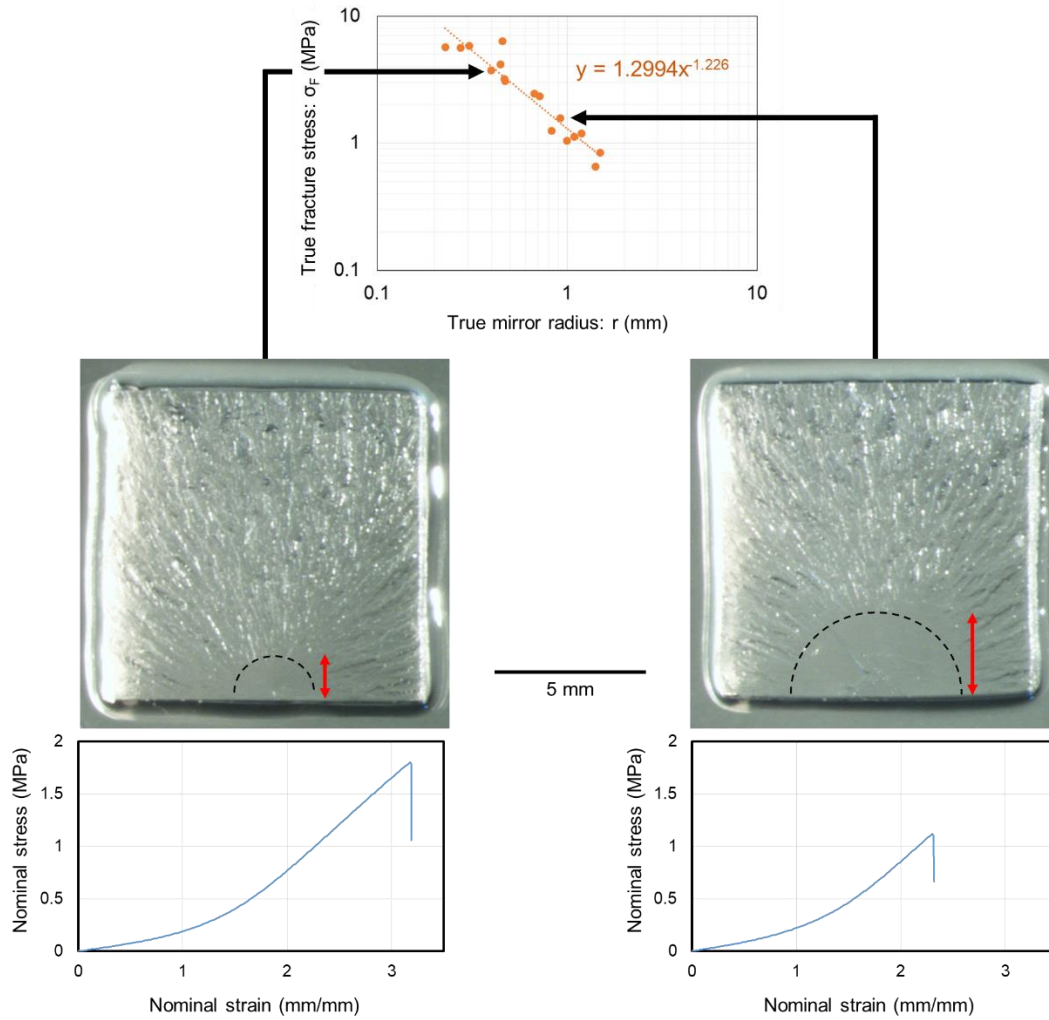


**Fig. 5.4** The relationship between true  $\sigma_F$  and true  $r$  for DN gel (1-8-0.1, 2-0.1-0.1). Fracture surface image and nominal stress-strain curve of two representative samples with small and large initial crack are shown. Red arrows in the images indicate nominal mirror radius.

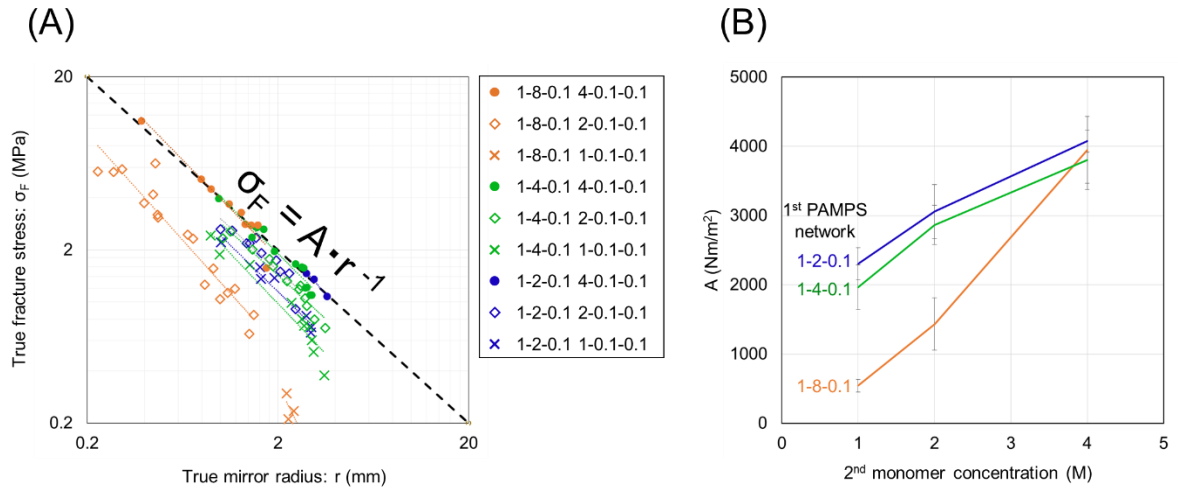


**Fig. 5.5** (A)  $\sigma_F$  versus  $r$  with various composition tough gels. The black dotted line in the graph indicates the slope of -1 power. (B) Material constant  $A$  with gel composition.

To investigate universality of the power-law correlation, the fracture analysis of various composition gels was conducted (**Fig. 5.5A**). All tough gels had power in the range of 0.95 to 1.25, which almost fitted by the following equation,

$$\sigma_F = A \cdot r^{-1}$$

where  $A$  ( $\text{Nm/m}^2$ ) is a material constant, whose dimension is same with stress intensity factor  $J$  ( $\text{Nm/m}^2$ ) of nonlinear elastic material<sup>[11]</sup>. The black dotted line in the graph indicates the slope of -1 power. To confirm that the  $A$  is a material-specific value independent from the experimental conditions, we evaluated  $A$  with different sample shape and tensile velocity of DN gel (**Fig. 5.6**). Even changing sample size and tensile speed, the  $A$  was almost constant to  $1,500 \text{ Nm/m}^2$ , resulting that  $A$  is a material constant only depending on the material composition. Therefore, the nonlinear elastic tough gel always



follows the above semi-empirical equation.

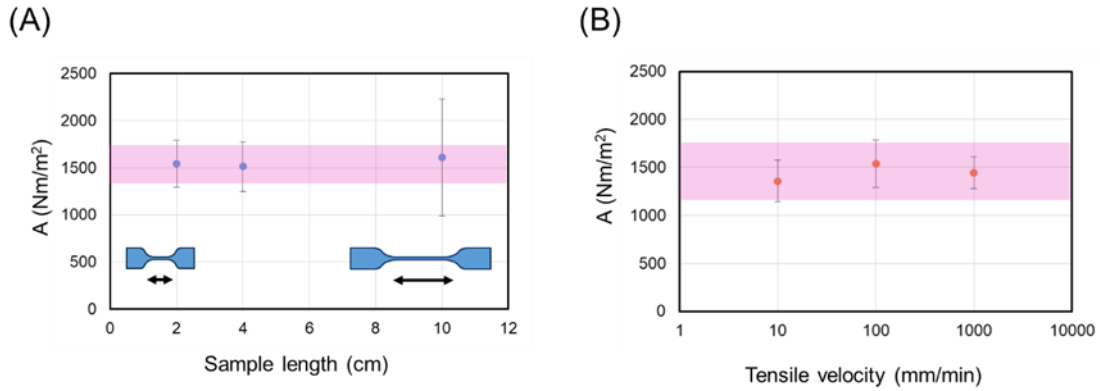


**Fig. 5.6** Material constants  $A$  under different experimental conditions. (a) Different sample gauge length. (b) Different tensile velocity. Sample composition is 1-8-0.1, 2-0.1-0.1.

In the previous studies on ceramics that are linear elastic and brittle materials, a following semi-empirical formula was established, X

$$\sigma_F = A_{linear} \cdot r^{-0.5}$$

where  $A_{linear}$  (Nm<sup>0.5</sup>/m<sup>2</sup>) is a material constant, whose dimension is same as stress intensity factor  $K$  (Nm<sup>0.5</sup>/m<sup>2</sup>) of linear elastic material. Moreover, some studies pointed out that  $A_{linear}$  is directly proportional to  $K_{IC}$ .

Considering the similarity between the two equations of the linear elastic material and the non-linear elastic material, we assume that  $A$  obtained in this study is corresponding to an index of material toughness correlated to  $J$ . In the DN gel, it is known that high 1<sup>st</sup> crosslinker and low 2<sup>nd</sup> monomer

concentrations result mechanically weak gel<sup>[17]</sup>. In this study, the gel of such compositions (1-8-0.1, 2-0.1-0.1 and 1-8-0.1, 1-0.1-0.1) showing low  $A$  is consistent with above fact. Typically, the  $J$  of rubber materials, which is a tough nonlinear elastic material like tough gel, is  $10^3$  to  $10^6$  J/m<sup>2</sup><sup>[18]</sup>. That of weak elastomer is well-comparable to the  $A$  (500 - 5000 J/m<sup>2</sup>) of DN gel in this study (**Fig. 5.5B**). This is reasonable because DN gels contain less than 10 wt% polymer compared to elastomer consisted 100 wt% polymer. Currently, the strict relation between  $A$  and  $J$  is not clear yet, while the  $A$  measured by the fracture surface analysis is useful to evaluate  $J$  that there have been no study in tough gels. We hope that the correlation between  $J$  and  $A$  will be clarified in the future.

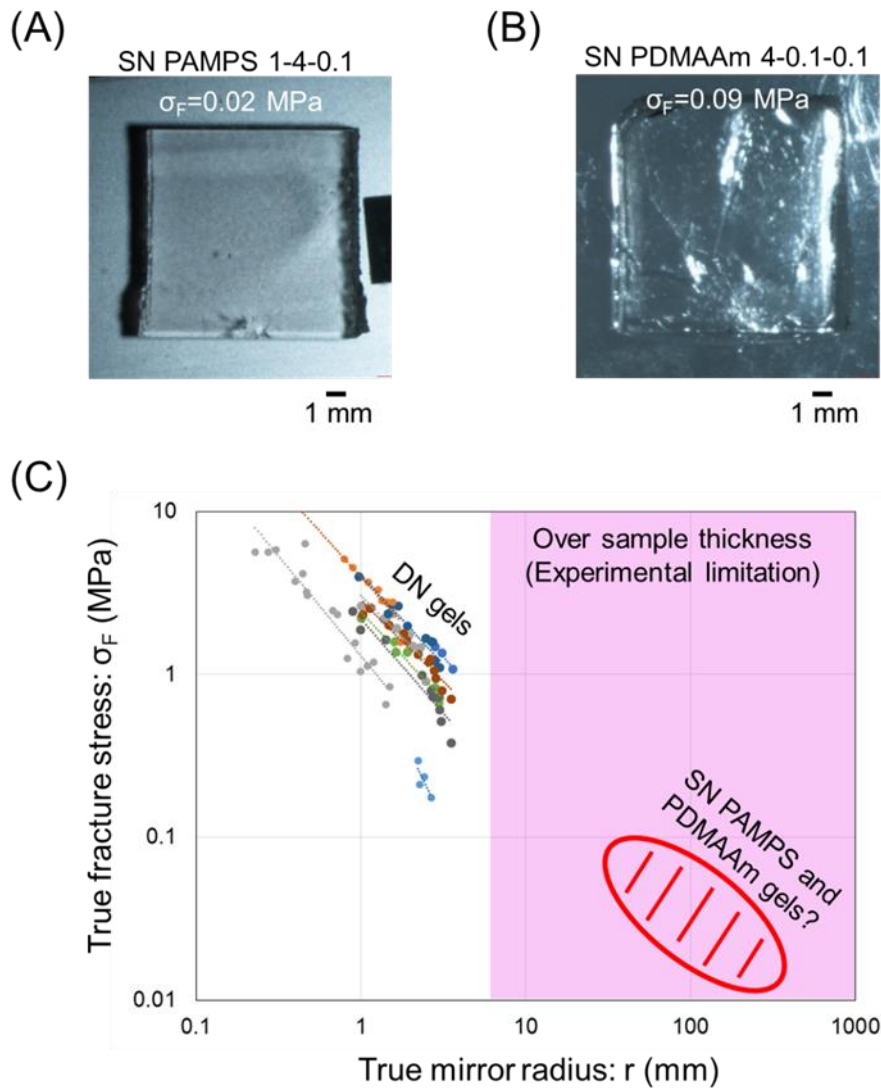


**Fig. 5.7** Fracture surface of single network (SN) gels, which are constituent materials of DN gel. (A) Equilibrium swollen SN PAMPS 1-4-0.1 gel. (B) Non-swollen SN PDMAAm 4-0.1-0.1 gel. (C) Fracture stress and mirror radius relation. These SN gels break with smaller fracture stress (10-100 kPa) than DN gels (0.2-10 MPa). Therefore, we considered that mirror radius greatly exceeds the sample size (1 cm  $\times$  1 cm) used in this study.

Additionally, we performed mirror radius observation for other hydrogels which is brittle and not tough (**Fig. 5.7**). The samples were SN PAMPS gel and SN PDMAAm gel, which are the constituent materials of the DN gel. Unfortunately, only a smooth mirror region was observed, and no mist-hackle region was seen on the fracture surface. This is because the mirror radius exceeded sample cross section ( $1\text{ cm} \times 1\text{ cm}$ ), since the mirror radius is inversely proportional to the fracture stress and these non-tough gels shows relatively small fracture stress (10-100 kPa) than tough gels (0.2-10 MPa). If we prepare larger size sample, mirror radius measurement could be applied to any brittle material.

#### **5.4 Conclusion**

In non-linear elastic hydrogel, it was confirmed that there is a -1 power law between the mirror radius and fracture stress. This new semi-empirical formula is different from that of previous linear elastic material, because they probably reflect the difference in stress distribution at the crack tip. Unfortunately, at present, we cannot show the physical meaning of material constant in the equation. Thus, in the future, we should measure gel toughness and clarify about what relationship exists between A and toughness.

#### **5.5 References**

- [1] O. Erol, A. Pantula, W. Liu, D. H. Gracias, *Adv. Mater. Technol.* **2019**, *4*, 1.
- [2] J. P. Gong, *Soft Matter* **2006**, *2*, 544.
- [3] R. A. Green, S. Baek, L. A. Poole-Warren, P. J. Martens, *Sci. Technol. Adv. Mater.* **2010**, *11*,  
DOI 10.1088/1468-6996/11/1/014107.
- [4] A. S. Hoffman, *Adv. Drug Deliv. Rev.* **2012**, *64*, 18.
- [5] K. Y. Lee, D. J. Mooney, *Chem. Rev.* **2001**, *101*, 1869.
- [6] K. Yasuda, N. Kitamura, J. P. Gong, K. Arakaki, H. J. Kwon, S. Onodera, Y. M. Chen, T.  
Kurokawa, F. Kanaya, Y. Ohmiya, Y. Osada, *Macromol. Biosci.* **2009**, *9*, 307.
- [7] J. P. Gong, *Soft Matter* **2010**, *6*, 2583.
- [8] J. Gong, Y. Katsuyama, T. Kurokawa, Y. Osada, *Adv. Mater.* **2003**, *15*, 1155.
- [9] T. L. Anderson, *Fracture Mechanics, Third Edition Fundamentals and Applications*,  
Taylor&Francis Group, LLC., **2005**.
- [10] E. Bouchbinder, T. Goldman, J. Fineberg, *Reports Prog. Phys.* **2014**, *77*, DOI 10.1088/0034-  
4885/77/4/046501.
- [11] R. Long, C. Y. Hui, J. P. Gong, E. Bouchbinder, *Annu. Rev. Condens. Matter Phys.* **2021**, *12*, 71.
- [12] Y. Zhou, J. Hu, P. Zhao, W. Zhang, Z. Suo, T. Lu, *J. Mech. Phys. Solids* **2021**, *153*, 104483.
- [13] I. Kolvin, J. M. Kolinski, J. P. Gong, J. Fineberg, *Phys. Rev. Lett.* **2018**, *121*, 135501.
- [14] R. C. Bradt, *J. Eur. Ceram. Soc.* **2014**, *34*, 3255.

- [15] J. J. MECHOLSKY, R. W. RICE, S. W. FREIMAN, *J. Am. Ceram. Soc.* **1974**, *57*, 440.
- [16] B. Shand, *J. Amerimn Ceram. Soc.* **1952**, *42*.
- [17] S. Ahmed, T. Nakajima, T. Kurokawa, M. Anamul Haque, J. P. Gong, *Polymer (Guildf)*. **2014**, *55*, 914.
- [18] Y. Morishita, K. Tsunoda, K. Urayama, *Polymer (Guildf)*. **2017**, *108*, 230.

## CHAPTER 6

### Fracture mechanism of pure elastic gel

#### 6.1 Introduction

Hydrogel is polymer network material containing water. Polymer network is soft and reversible due to entropic elasticity comes from thermal motion. To connect network, there are two types of crosslinking points. One is permanent chemical bond made by covalent bond, and another is transient physical bond made by various weak bonds such as ionic interaction, hydrogen bond, hydrophobic bond, or physical entanglement. An ideal pure elastic hydrogel without physical bond is brittle and easily broken from small crack.<sup>[1,2]</sup> Such kind of fracture is called brittle fracture, in the case of ceramics, crack propagates weakest route in the micro structure.<sup>[3]</sup> However, unfortunately, there are no study to investigate the micro fracture pathway of hydrogel. This is because surface tension collapse fracture surface structure of soft hydrogels.<sup>[4,5]</sup> In addition, hydrogel's low modulus makes contact mode AFM impossible.

We resolve this problem by using pure elastic polyelectrolyte gel. The polyelectrolyte gel shows high Young's modulus (0.1 to 1 MPa) and high swelling ratio due to its extremely high ionic osmotic pressure.<sup>[6-8]</sup> High modulus enables keeping non-deformed structure against surface tension, and large swelling makes structure easier to observe. Still slightly deformation remained, but it was removed by surface tension correction equation reported by Hui.<sup>[9]</sup>

In pure elastic hydrogel, we confirmed inter-microgel fracture. In the chain polymerization process for gel synthesis, submicron sized microgels form firstly and later they connect to make bulk gel.<sup>[10,11]</sup> Like inter-granular fracture of ceramics, in the case of a pure elastic gel, inter-microgel is the weakest route for fracture (**Fig. 6.1a**).

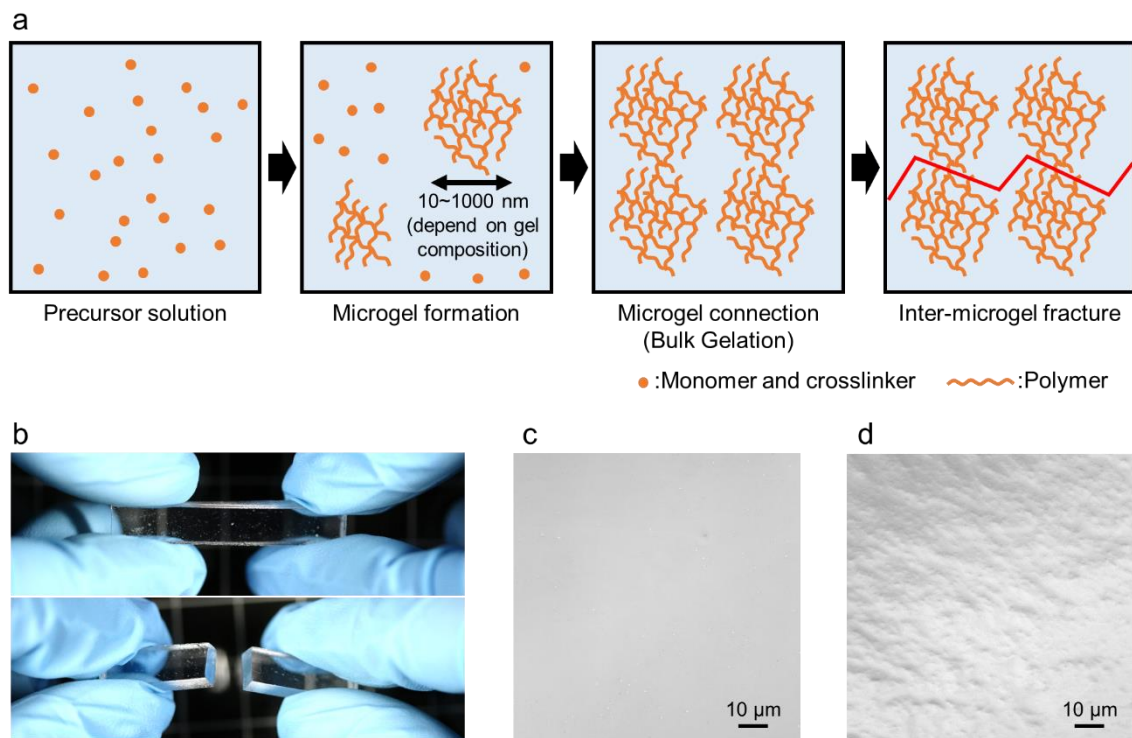


**Figure 6.1** Fracture mechanism of pure elastic hydrogel. (a) Gelation process (chain polymerization) and Fracture process of pure elastic gel. (b) Appearance of pure elastic hydrogel (PAMPS-4), before and after fracture. (c) As synthesized surface of pure elastic gel. (d) Tensile fracture surface of pure elastic gel.



## 6.2 Experiments

### 6.2.1 Materials

2-Acrylamido-2-methyl propanesulfonic acid (AMPS: monomer) was provided from Toagosei Co. Ltd, Japan. *N, N'*-methylenebisacrylamide (MBAA: crosslinker), 2-oxoglutaric acid ( $\alpha$ -keto: initiator), Sodium Chloride (NaCl), and iron (III) chloride hexahydrate were purchased from Wako Pure Chemical Ind., Ltd., Japan. All chemicals were used as received.

### 6.2.2 Gel synthesis

PAMPS gel was synthesized by UV radical polymerization in a mold made from a 2 mm silicone spacer sandwiched by two glass plates. UV irradiation time was 6 h and the mold was previously deoxidized overnight in the inert argon atmosphere. The composition of precursor solution was 1 mol/L AMPS as monomer, 2-10 mol% MBAA as a cross-linker, and 0.1 mol%  $\alpha$ -keto as an initiator. Then the PAMPS gel was removed from the mold and soaked into solvents (pure water or 1 M NaCl) until equilibrium for one day and used for experiments. As prepared state samples are used for experiments immediately after removal from the mold.

### 6.2.3 Tensile test

The tensile mechanical property of PAMPS gels was examined by using a mechanical tester

(Tensilon RTC-1310A, Orientec Co., Japan). The samples were cut into dumbbell shape by a programmed laser cutter (ULR-60, Universal Laser Systems, US). Then, we introduced triangular initial crack for samples by using a fine microtome knife, whose edge thickness is 76  $\mu\text{m}$ . Tensile test was performed at a speed of 100 mm/min. After sample fracture, we immersed all sample in pure water for two days until equilibrium and observed fracture surface in equilibrium state.

The PAMPS network mesh size at the each swelling degree ( $\zeta$ ) was estimated from the Young's modulus  $E_{as-pre}$ , as follows.

$$E_{as-pre} = 3G_{as-pre} = \frac{3k_b T}{\xi_0^3}$$

where  $k_b$ ,  $T$  and  $\xi_0$  are Boltzmann constant, measurement temperature, mesh size at as-prepared state, respectively. The mesh size of the swelled PAMPS gel ( $\xi$ ) was estimated from the volume swelling ratio  $Q$  of the swollen PAMPS gels relative to its as-prepared state as follows.

$$\xi^3 = Q \times \xi_0^3$$

#### **6.2.4 Roughness observation by transmission electron microscopy (TEM)**

For TEM observation, we followed previous chapter. Skeleton PDMAAm network introduction into tensile fractured PAMPS gel and mineral staining were performed. For staining, the PAMPS/PDMAAm gels were immersed in 2.5 M  $\text{FeCl}_3$  staining solution for one day in room temperature. Then the gels were immersed in pure water to increase pH for mineralization of

amorphous ferric oxide nanoparticle in the PAMPS gel network, especially near bulk surface.

To observe surface morphology of stained hydrogel, we carried out TEM observation (H-7650, Hitachi, Japan). To prepare the specimen for TEM observation, the hydrogels were frozen in liquid nitrogen, and water in the hydrogel was exchanged to ethanol and then acrylic resin (London Resin white, medium) in a chamber of an automatic freeze substitution system (EM AFS2, Leica Microsystems, Germany). The final thickness change of the resin-cured specimen was within 10% in relative to that of the PAMPS gel in water. Then, 100-nm thick sections of the resin-cured specimen were cut by an ultra-microtome (EM UC7i, Leica Microsystems, Germany) and placed on a carbon supported copper mesh grid. The acceleration voltage of the electron gun for observation was 100 kV.

#### ***6.2.5 Roughness observation by 3D laser microscopy***

The two dimensional height scanning of tensile fracture surface of PAMPS gel was performed by 3D laser microscopy (VK-9710, KEYENCE, Japan). Before measurement, we gently wiped surface water of gel. The wavelength of the laser light source was 408 nm. Z-axis resolution is 50 nm (one step of machine motor). X and Y-axis resolutions are 138 nm. Each samples were measured more than six times in different position.

#### ***6.2.6 Roughness observation by atomic force microscopy (AFM)***

To evaluate in water roughness, not deformed by surface tension, we performed high speed AFM (BL-AC10DS-A2, Olympus, Japan) measurement. PAMPS-8 was fixed on sample stage by using glue (Super X). Then, tapping mode measurement, which resonance frequency is 500 to 700 kHz and measurement area is  $9 \times 9 \mu\text{m}$ , was performed in the pure water.

### **6.2.7 Power spectrum density (PSD) analysis**

2D height images were analyzed by calculating their two dimensional power spectrum density. To calculate 2D PSD, we followed previous report.<sup>[9,12]</sup> We calculated 2D PSD of  $141 \mu\text{m} \times 141 \mu\text{m}$  area ( $1024 \times 1024$  pixel, one pixel: 138 nm) by using radial Hann window.<sup>[12]</sup> For 3D laser microscope data, we removed surface tension effect by Hui's equation.<sup>[9]</sup> Since fracture surface of PAMPS gel shows self-affine nature in line with the crack propagation direction, we take the radial average in the range of  $\pm 10$  degrees for parallel to the crack direction and perpendicular to the crack direction. Obtained  $\pm 10$  degrees radial average 2D PSD were used for analysis. All PSD shows similar trend, decreasing at low wave vector, and plateau at high wave vector. This plateau is comes from resolution limit of microscopy. Because the height resolution of 3D laser microscope is 50 nm and we confined that there are no structure larger than 100 nm on fracture surface of gel by TEM image, this decreasing-plateau transition point is nearly same with lower cut-off point of PSD. Wave vector at lower cut-off comes from smallest structure in the observation window. That is, reciprocal number of wave vector

at transition point indicates smallest roughness width (smallest structure size) in gel fracture surface.

In all sample, parallel direction 2D PSD follows with power law. Hurst index (H) describes raggedness of crack propagation.  $H$  is calculated by slope of 2D PSD in log-log graph.<sup>[12]</sup>

$$H = \frac{-2 - (\text{Slope of PSD})}{2}$$

Perpendicular direction 2D PSD of PAMPS-8, 10 agreed with exponential. Memory length ( $\lambda$ ) of them is calculated by slope of PSD in semi-log graph.

$$y = Ae^{-\frac{x}{\lambda}}$$

## 6.3 Results and discussion

### 6.3.1 Inter-microgel fracture of pure elastic gel

We ascertain inter-microgel fracture of various gels, having different network structure and mechanical property by controlling crosslinker concentration. For polyelectrolyte gel synthesis, we use 1 M AMPS as monomer, 2~10 mol% MBAA as crosslinker, and 0.1 mol%  $\alpha$ -keto as initiator. Each mol% is relative to the monomer. We call gel containing x-mol% crosslinker as PAMPS-x. Synthesized gels are immersed in pure water until equilibrium. After that, we fractured samples by uniaxial extension (**Fig. 6.1b**). As-synthesized surface is flat (**Fig. 6.1c**), but fracture surface is rough (**Fig. 6.1d**).

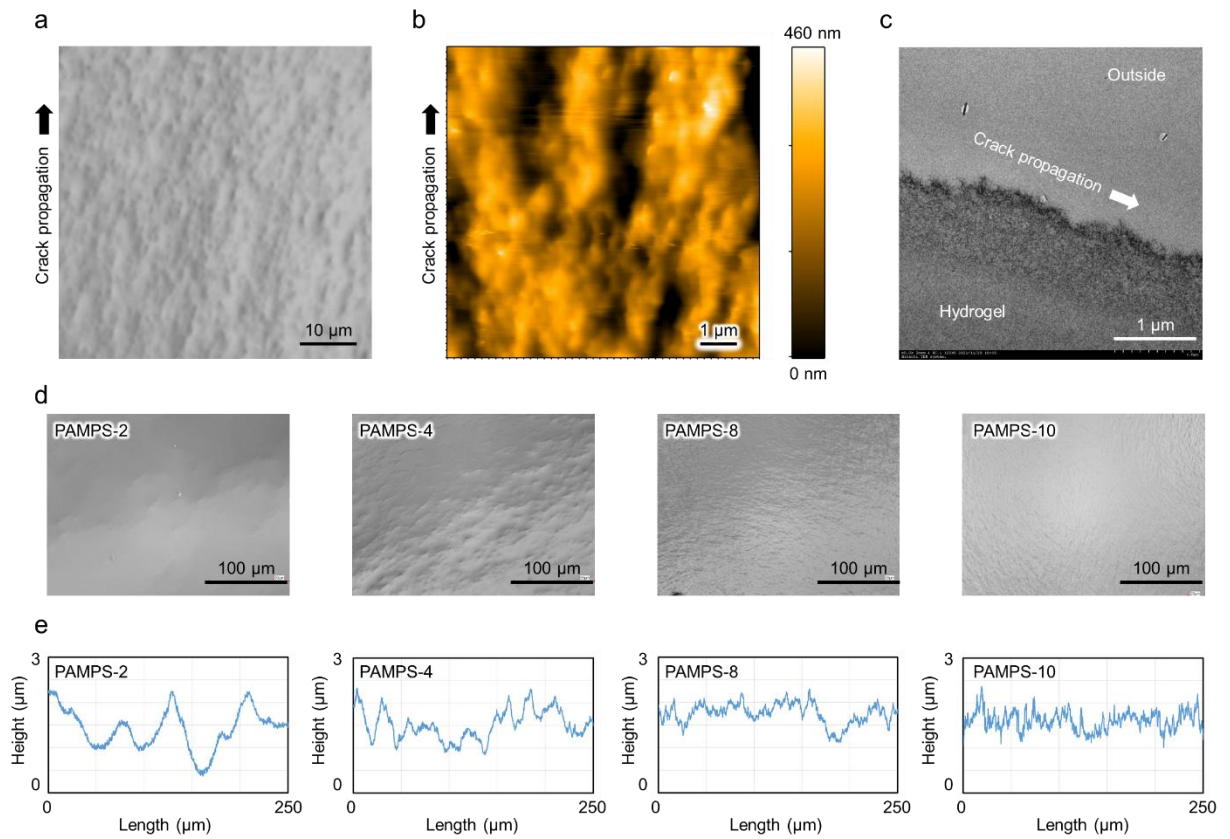


**Figure 6.2** Fracture surface of pure elastic hydrogel (PAMPS-8) in various observation methods. (a) 3D laser microscopy image. (b) Atomic force microscopy image. (c) Transmission electron microscopy image of cross section of fracture surface. (d) Fracture surface of various crosslinker concentration gels. (e) 1D height images of (d).

For further analysis, we measure the high magnification fracture surface image of PAMPS-8 gel by various method (**Fig. 6.2a~c**).<sup>[13]</sup> The crack progress radially from initial defect, and fracture roughness exhibit anisotropy with respect to the crack propagation direction. In TEM image, we can recognize the minimum roughness size of about 1  $\mu\text{m}$  (**Fig. 6.2c**) and there are no other characteristic

structure smaller than it. This size is much larger than calculated mesh size of PAMPS-8 (11 nm) (**Fig. 6.3c**), indicating existence of huge inhomogeneous structure. Inter-microgel fracture is an only reasonable answer given such structure. This fracture mechanism is a common phenomenon also in thermosetting plastics.<sup>[14,15]</sup> Furthermore, we measure the fracture surface of various PAMPS-x gels (**Fig. 6.2d~e**). As crosslinker increase, fracture surface become fine and smallest roughness size decrease. This is consistent with microgel formation process, in which high crosslinker suppress wide spreading of polymer and results small microgel.

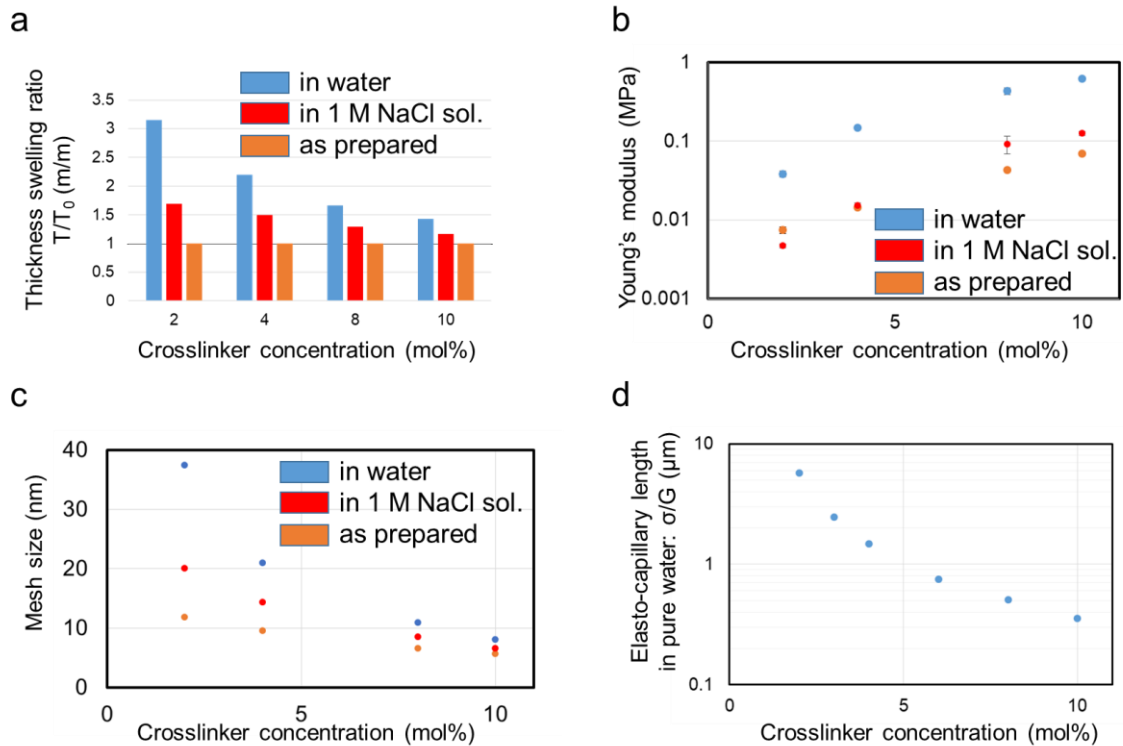


**Fig. 6.3** Mechanical properties of PAMPS gels in different swelling degree and crosslinker concentration. (a) Thickness swelling ratio of PAMPS gels.  $T_0$  is a as-prepared thickness immediately

after polymerization. (b) Young's modulus of PAMPS gels equilibrium in different solvents. (c) Mesh size of PAMPS gels calculated from swelling ratio and Young's modulus. (d) Elasto-capillary length of water-swollen PAMPS gels. We assume surface tension  $\sigma$  is same with water (72.75 mN/m).

If fracture mechanism is inter-microgel fracture, the same network structure should exhibit same fracture surface, regardless of swelling degree and mechanical property at fracture. We change the swelling degree of PAMPS-x gel (as-prepared, equilibrium in 1 M NaCl, equilibrium in pure water). The modulus was varied over one order magnitude (**Fig. 6.3a, b**). After tensile fracture in different swelling degree, we immersed all sample into pure water until equilibrium, to observe fracture surface in same fully swelling state. To quantitatively analyze surface roughness, we performed Fourier transfer for two dimensional height images obtained by 3D laser microscope.<sup>[12]</sup> The two dimensional power spectrum density (2D PSD) of PAMPS-x are shown in **Fig. 6.4**.



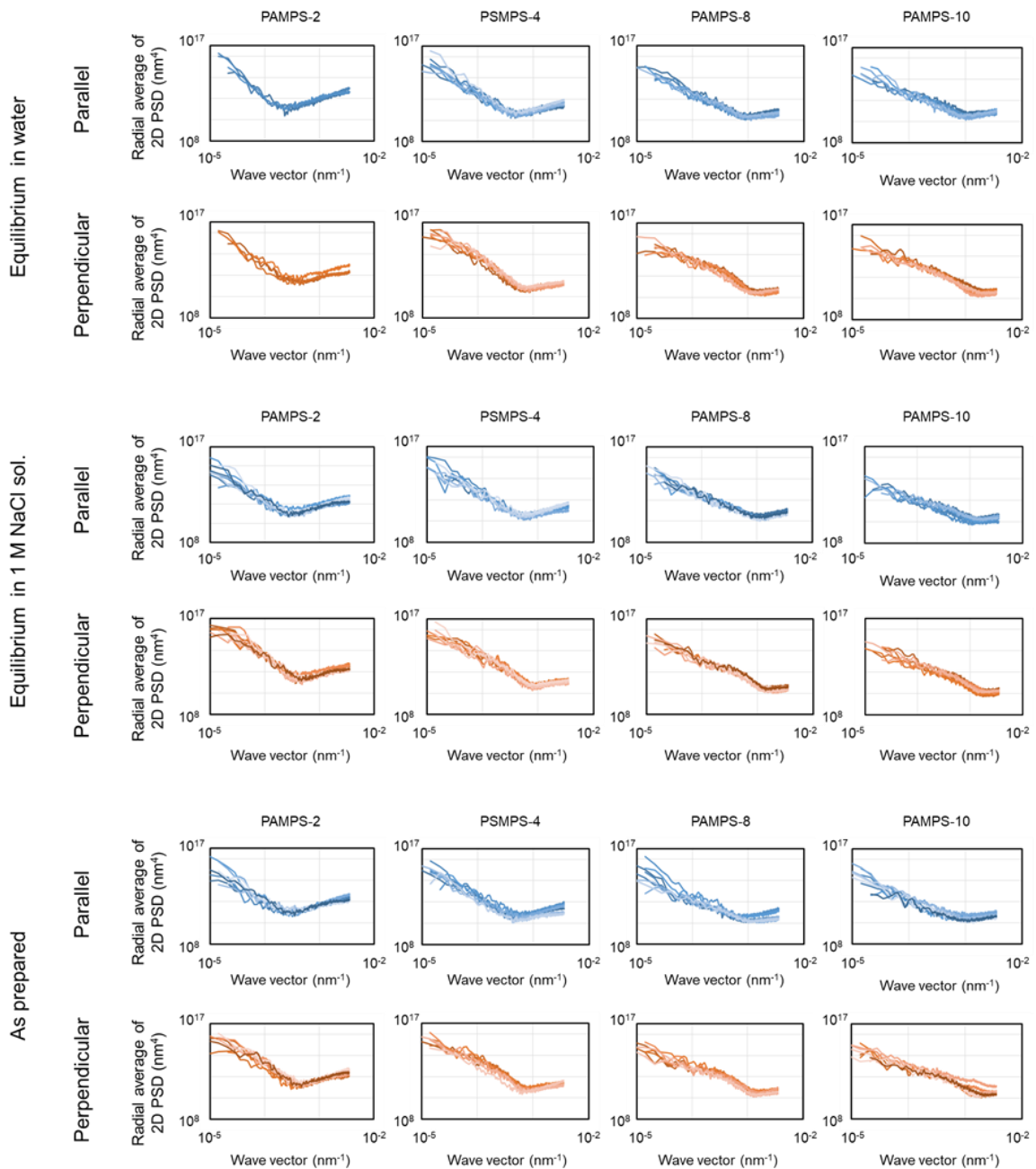


**Fig. 6.4** Log-log graph of 2D PSD law data. These PSD are  $\pm 10$  degrees radial average in parallel and perpendicular direction of crack propagation direction. Each samples are measured more than 4 times.

They are  $\pm 10$  degree average of each direction, parallel to the crack, and perpendicular to the crack.

From 2D PSD, we calculate the smallest roughness size on the fracture surface. Despite the fact that the mechanical property changed greatly depending on the swelling degree (**Fig. 6.5a**), all PAMPS-x gels show same smallest roughness size (microgel size) regardless of swelling degree at fracture (**Fig. 6.5b, c**). For these gels, in as-synthesized state, mesh size are range of 5~11 nm (**Fig. 6.3c**), and microgel size are range of 500~1000 nm. That is, microscale fracture pathway is two order magnitude rougher than the mesh size.

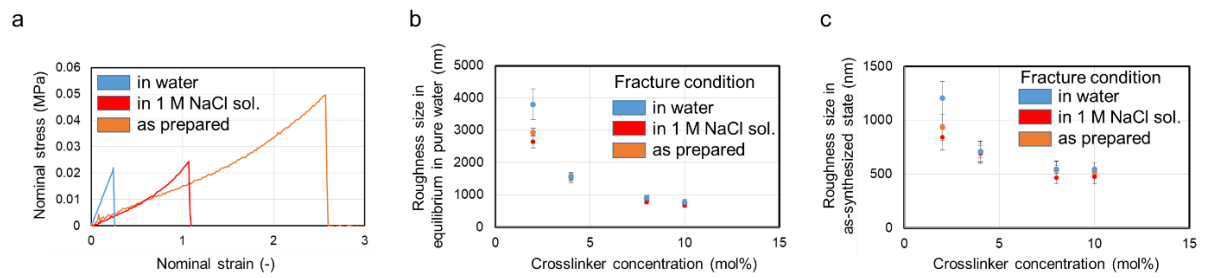


**Fig. 6.5** Fracture surface similarity for various swelling degree at fracture. (a) Tensile stress-strain curve of PAMPS-4 gel in different swelling ratio. (b) Smallest roughness size in the fully swelled state in the pure water. (c) Smallest roughness width in as-synthesized state. Smallest roughness size only depend on gel composition, but not swelling ratio and modulus.

Whether this inter-microgel fracture is due to lack of polymer network (space inhomogeneity), or lack of crosslinking point (connectivity inhomogeneity)?<sup>[11]</sup> We answer this question by observing fracture surface of semi-dried gel. In dry gel fracture, connectivity inhomogeneity should disappear

because of van der Waals interaction between microgels overcome covalent crosslinking, so that if the fracture origin is connectivity inhomogeneity, dry gel exhibit flat fracture surface. On the other hand, if the fracture origin is space inhomogeneity, dry gel and swollen gel should have same rough fracture surface. Semi-dried gel shows clear transition between inter-microgel fracture in water-rich side and flat fracture in dried side (**Fig. 6.6**). Thus, inter-microgel fracture occurs, because crosslinking density between microgels is less than crosslinking density inside microgels.

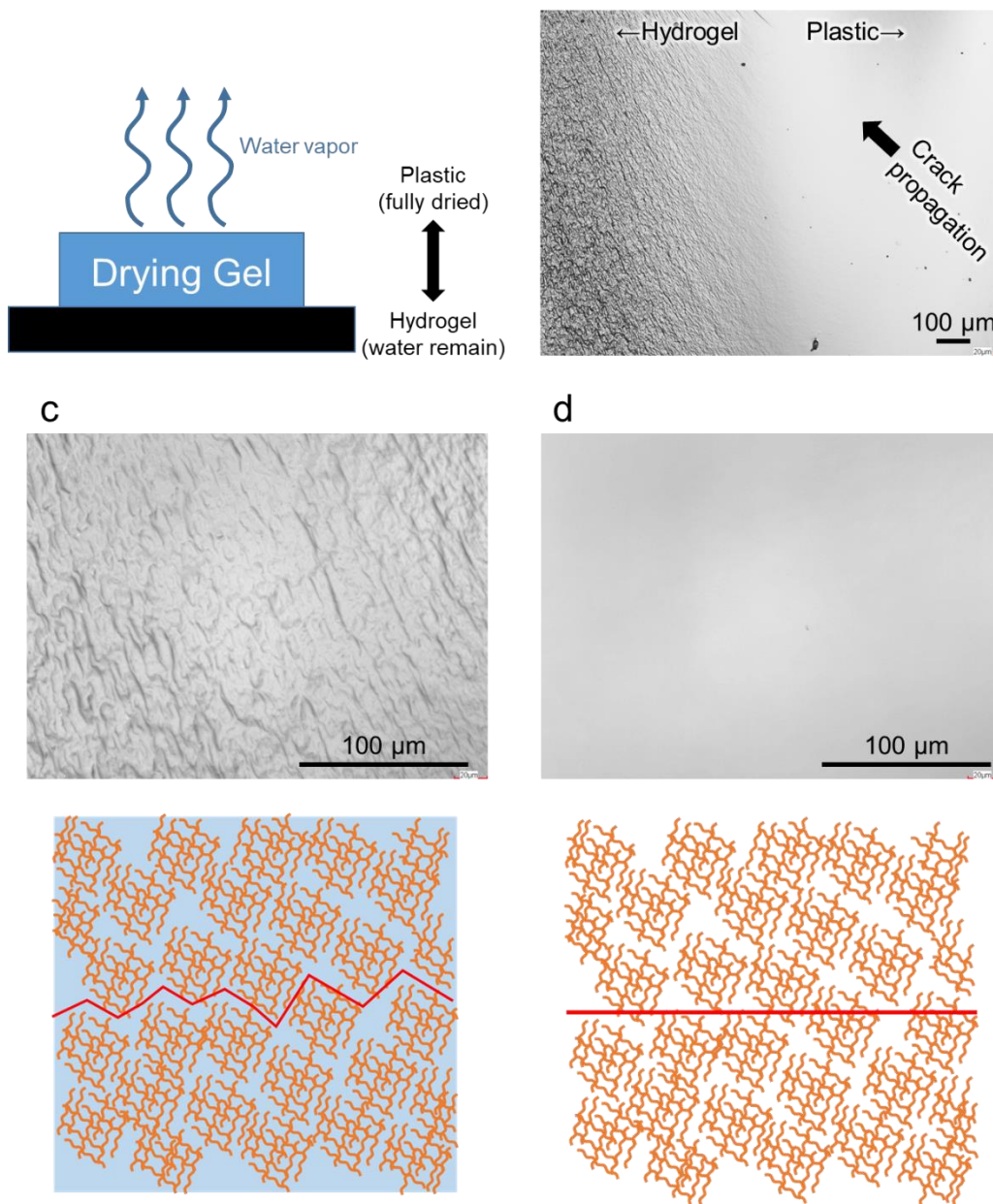


**Fig. 6.6** Fracture surface images of semi-dried PMAPS-4 gel. (a) Schematic non-uniform drying procedure. (b) Fracture surface around hydrogel-plastic transition point. (c) High magnification Image of hydrogel part of (b). (d) High magnification Image of plastic part of (b). This sample was tensile fractured in semi-dried state, then immersed into pure water two days until equilibrium. Fracture surface was observed by 3D laser microscope.

### ***6.3.2 Microscale fracture mechanism of pure elastic gel***

The fracture surface of materials often exhibit self-affine property, because crack propagation is anisotropic process.<sup>[16-18]</sup> Pure elastic PAMPS hydrogel also shows self-affine nature. When we focus on the 2D PSD parallel to the crack propagation direction, all sample shows single power law until machine limitation (in this samples, same with lower cut off by microgel size), meaning roughness is fractal. Crack pathway is completely determined by fracture mechanism in microgel scale, and there are no other factor affecting crack propagation. From 2D PSD slope in **Fig. 6.4**, we calculate Hurst index (H), which describes raggedness of crack propagation. H takes range of 0 to 1. If  $H < 0.5$ , the process is anti-persistent. If  $H = 0.5$ , the process is random walk. If  $H > 0.5$ , the process is persistent. In PAMPS gel, the Hurst index decreases from  $H = 0.5$  to  $H = 0$  as the crosslinker concentration increasing (**Fig. 6.7**).

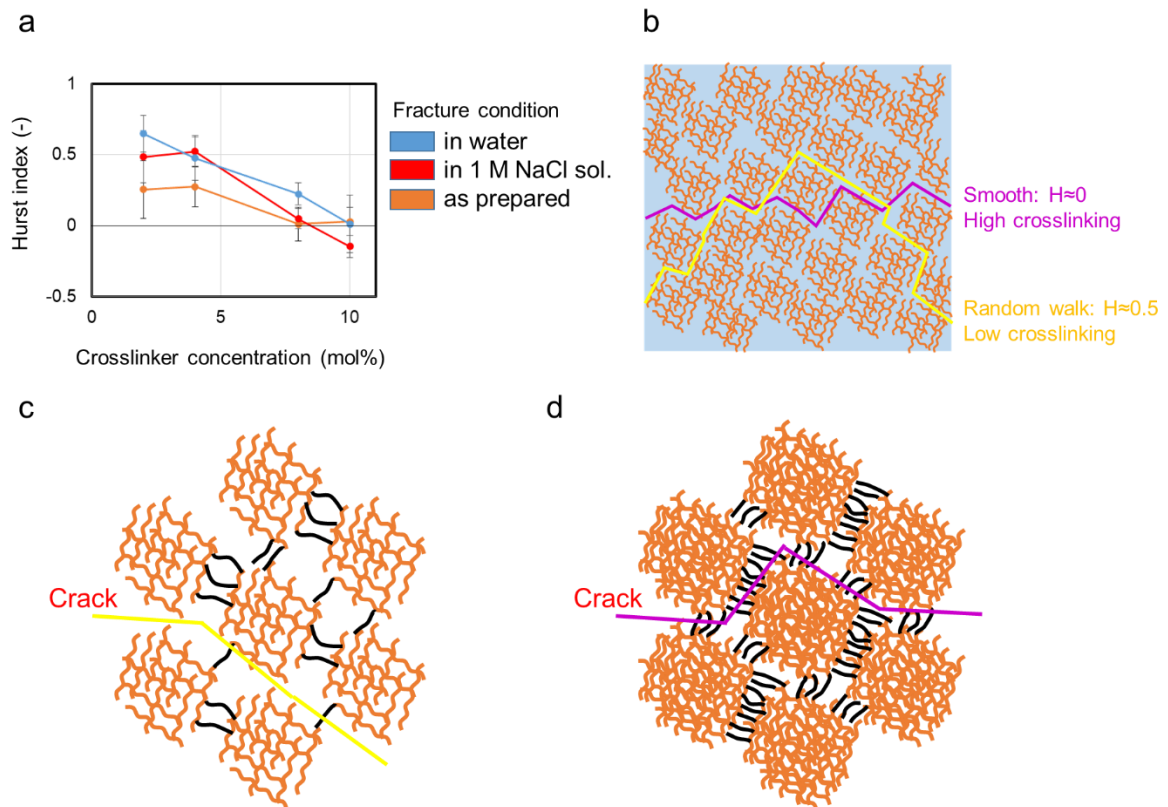


**Fig. 6.7** Crack roughness and micro-scale fracture mechanism. (a) Hurst index of various PAMPS gels.

(b) Schematic image of crack pass way in the case of  $H \approx 0$  and  $H \approx 0.5$ . (c) Micro-scale fracture process of low crosslinking gels. The crack follows weakest link in the gel. Since the path is determined by which route has few inter-microgel crosslinking in micro scale, total pass way becomes random walk. (d) Micro-scale fracture process of high crosslinking gels. Since there is almost no difference between routes, the stress field becomes dominant and the entire path goes straight. The black lines in the figure indicate inter-microgel crosslinking.

For low crosslinking gel ( $H = 0.5$ ) the number of inter-microgel crosslinking is also small. Thus,

variations in inter-microgel crosslinking per route are probably large. When the crack propagates in the gel of low crosslink density, the crack selects and proceeds between the inter-microgel with fewer number of crosslink (weakest path) (**Fig. 6.7b, c**). Since the probability of whether the upper side of the microgel or the lower side of the microgel has few inter-microgel crosslinking is half and half, crack propagation eventually become a random walk ( $H = 0.5$ ). On the other hand, high crosslinking gel ( $H = 0$ ) has large number of inter-microgel crosslinking. It results negligible difference between routes, and crack only receives the influence of the stress field that attempts to proceed straight (**Fig. 6.7b, d**). Interestingly, PAMPS-2, 4 with low swelling degree (as-prepared) exhibit relatively anti-persistent crack propagation ( $H \approx 0.25$ ) compared with high swelling samples. In the gel with low swelling degree, the distance between microgels gets close, so the physical entanglement could form and act as additional inter-microgel crosslinking.

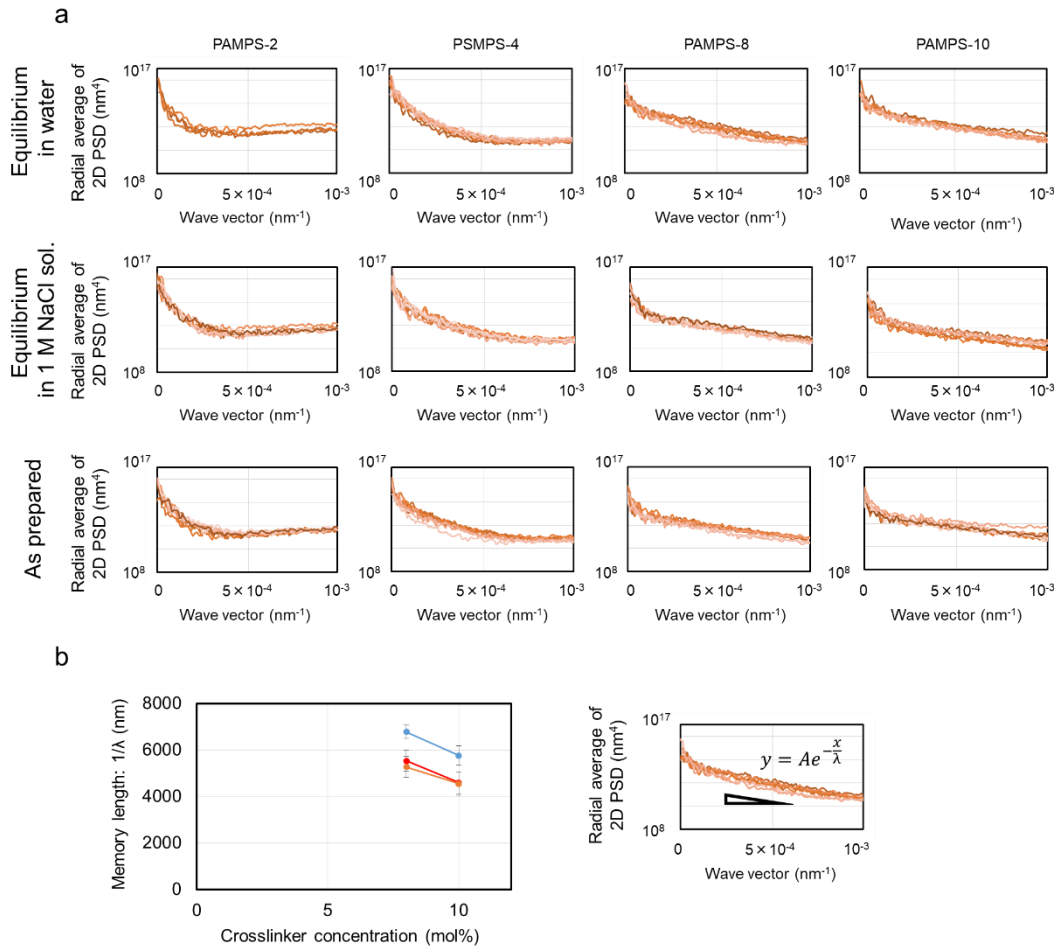


**Fig. 6.8** (a) Semi-log graph of 2D PSD law data. (b) Memory length measured by 2D PSD. These PSD are  $\pm 10$  degrees radial average in perpendicular direction of crack propagation direction. PAMPS-8 and PAMPS-10 are well fitted with exponential function in the wave vector range of 0.0001 to 0.001 nm<sup>-1</sup>. Each samples are measured more than 4 times.

We next analyze about 2D PSD perpendicular to the crack propagation direction. Like parallel direction, the perpendicular direction of PAMPS-2, 4 follow single power law. However, PAMPS-8, 10 do not agree with power law, but they agree with exponential, meaning the presence of short-term



memory up to a certain distance (**Fig. 6.8**). The calculated memory lengths are 4~7  $\mu\text{m}$  and this is consistent with a large scale structure visible on the microscopy images (**Fig. 6.2b**). We consider the difference between PAMPS-2, 4 and PAMPS-8, 10 comes from their crack propagation mechanism. Low crosslinking density gels (PAMS-2, 4), in which cracks follow by random walk, can be randomly also in perpendicular direction. On the other hand, in high crosslinking gels (PAMPS-8, 10), since the stress field constraint also exists in the perpendicular direction, the crack cannot ignore adjacent crack pathway. Some distance (memory length) are required to forget neighbors.

#### **6.4 Conclusions**

Chain polymerized hydrogel has connectivity inhomogeneity at inter-microgel. In pure elastic gel fracture, fracture mechanism is inter-microgel fracture. Crack pathway is influenced by crosslinking density. By utilizing the finding in this chapter, we will understand fracture mechanics of hydrogel more deeply. For example, dissipation energy per chain at gel fracture should determine accurately by considering inter-microgel crosslinking density and true fracture surface area.<sup>[19]</sup>

There are some unsolved questions. It would be necessary to develop a method of separately evaluating the properties of inter-microgel crosslinking and intra-microgel crosslinking. This problem has never been considered so far in gel science that assumed network close to uniform. We have to know which crosslinking density mainly contribute to the mechanical properties of bulk gel. In

addition, it is necessary to evaluate the effect of viscosity for the gel fracture. In this work we use pure elastic hydrogel without viscosity, but most of gels, including PAAm gel, have velocity dependent components in addition to chemical crosslinking.

## 6.5 References

- [1] J. Kim, G. Zhang, M. Shi, Z. Suo, *Science* (80-. ). **2021**, 374, 212.
- [2] C. Chen, Z. Wang, Z. Suo, *Extrem. Mech. Lett.* **2017**, 10, 50.
- [3] T. L. Anderson, *Fracture Mechanics, Third Edition Fundamentals and Applications*, Taylor&Francis Group, LLC., **2005**.
- [4] A. Jagota, D. Paretkar, A. Ghatak, *Phys. Rev. E - Stat. Nonlinear, Soft Matter Phys.* **2012**, 85, 1.
- [5] X. Xu, A. Jagota, S. Peng, D. Luo, M. Wu, C. Y. Hui, *Langmuir* **2013**, 29, 8665.
- [6] M. Rubinstein, R. H. Colby, A. V. Dobrynin, J. F. Joanny, *Macromolecules* **1996**, 29, 398.
- [7] M. Quesada-Pérez, J. A. Maroto-Centeno, J. Forcada, R. Hidalgo-Alvarez, *Soft Matter* **2011**, 7, 10536.
- [8] N. A. Peppas, A. R. Khare, *Adv. Drug Deliv. Rev.* **1993**, 11, 1.
- [9] C. Y. Hui, Z. Liu, N. Bain, A. Jagota, E. R. Dufresne, R. W. Style, R. Kiyama, J. P. Gong, *Proc. R. Soc. A Math. Phys. Eng. Sci.* **2020**, 476, DOI 10.1098/rspa.2020.0477.
- [10] S. Seiffert, *Polym. Chem.* **2017**, 8, 4472.

- [11] M. Shibayama, A. M. Shibayama, T. Norisuye, *Bull. Chem. Soc. Jpn* **2002**, *75*, 641.
- [12] T. D. B. Jacobs, T. Junge, L. Pastewka, *Surf. Topogr. Metrol. Prop.* **2017**, *5*, aa51f8.
- [13] T. Ando, T. Uchihashi, T. Fukuma, *Prog. Surf. Sci.* **2008**, *83*, 337.
- [14] C. M. Sahagun, S. E. Morgan, *ACS Appl. Mater. Interfaces* **2012**, *4*, 564.
- [15] J. Mijović, J. A. Koutsky, *Polymer (Guildf)*. **1979**, *20*, 1095.
- [16] P. Du, B. Xue, Y. Song, S. Lu, J. Yu, Q. Zheng, *Polym. Bull.* **2010**, *64*, 185.
- [17] M. A. Issa, M. A. Issa, M. S. Islam, A. Chudnovsky, *Eng. Fract. Mech.* **2003**, *70*, 125.
- [18] B. B. Mandelbrot, D. E. Passoja, A. J. Paullay, *Nature* **1984**, *308*, 721.
- [19] S. Wang, S. Panyukov, M. Rubinstein, S. L. Craig, *Macromolecules* **2019**, *52*, 2772.

## CHAPTER 7

### Summary of dissertation

In this dissertation, I have focused two things: developing direct observation method for hydrogel's nano-scale structure and investigating fracture mechanism of hydrogel. By combination of essence of organic science and inorganic science, I successfully developed the useful direct observation method for hydrogel. It helped unravel the long-mysterious hydrogel fracture mechanism.

The following conclusions were given:

**In chapter 4**, we developed the novel direct observation method for hydrogel network. The hints of this method were discovered through the previous study **in chapter 3**. High resolution (about 10 nm) and wide range (nm to several hundred  $\mu\text{m}$ ) observation was achieved without network structure deformation. Inhomogeneous mineralization on the hydrogel network enhanced the contrast in TEM observation, and interpenetrated polymer networks in DN gel enabled to keep its unperturbed structure even in the high concentrated staining solution. Through this technique, several local structures (surface dangling chains, micro void, etc.) of hydrogel were observed in the first time.

**In chapter 5**, I demonstrated the crack branching during brittle fracture of hydrogel. By measuring the mirror radius on the fracture surface, I successfully obtained the -1 power law between fracture stress and mirror radius. I found that this result is related with stress concentration field before fracture.

**In chapter 6**, Inter-microgel fracture in pure elastic gel was revealed by observing fracture surface in nm to mm wide range. This study is innovative because it clarified the microscale fracture mechanism of hydrogels for the first time. Moreover, the gel composition effect on micro-scale fracture was clarified by using fractal analysis technique.

Our study gave some important insights for simple elastic hydrogel science. Beyond the limitation of ideal model, next challenge is to clarify structure and fracture mechanism of real hydrogels, which usually shows strong viscoelastic property. To establish real hydrogel science based on the direct observation, I believe this dissertation will be the guideline for future researchers.

## List of Publications

### 7.1 Original papers

1. Ryuji Kiyama, Takayuki Nonoyama, Susumu Wada, Shingo Semba, Nobuto Kitamura, Tasuku Nakajima, Takayuki Kurokawa, Kazunori Yasuda, Shinya Tanaka, Jian Ping Gong: "Micro patterning of hydroxyapatite by soft lithography on hydrogels for selective osteoconduction" *Acta Biomaterialia*, **81**, 60-69 (2016)

2. Ryuji Kiyama, Takayuki Nonoyama, Masahiro Yoshida, Tomas Sedlacik, Hiroshi Jinnai, Jian Ping Gong: "Nano Scale Direct Imaging of a Rubber Elastic Hydrogel Network" **in**

#### **Preparation**

3. Ryuji Kiyama, Takayuki Nonoyama, Daniel R. King, JianPing Gong: "Fracture Mirror Radius of Non-Linear Elastic Hydrogel" **in Preparation**

4. Ryuji Kiyama, Takayuki Nonoyama, Kazuki Fukao, Tsutomu Indei, Takayuki Uchihashi, Feng Yueh Chan, Zezhou Liu, Chung Yuen Hui, Jian Ping Gong: "Fracture mechanism of Hydrogel  
①Pure elastic gel" **in Preparation**

## 7.2 Other papers

1. Takayuki Nonoyama, Susumu Wada, Ryuji Kiyama, Nobuto Kitamura, Md.Tarifur Islam Mredha, Xi Zhang, Takayuki Kurokawa, Tasuku Nakajima, Yasuaki Takagi, Kazunori Yasuda, and Jian Ping Gong: "Double-Network Hydrogels Strongly Bondable to Bones by Spontaneous Osteogenesis Penetration", *Adv. Mater.*, **28**, 6740–6745 (2016)
2. Susumu Wada, Nobuto Kitamura, Takayuki Nonoyama, Ryuji Kiyama, Takayuki Kurokawa, Jian Ping Gong, Kazunori Yasuda: "Hydroxyapatite-coated double network hydrogel directly bondable to the bone: Biological and biomechanical evaluations of the bonding property in an osteochondral defect", *Acta Biomaterialia*, **44**, 125–134 (2016)
3. Kazuki Fukao, Takayuki Nonoyama, Ryuji Kiyama, Kazuya Furusawa, Takayuki Kurokawa, Tasuku Nakajima, and Jian Ping Gong: "Anisotropic Growth of Hydroxyapatite in Stretched Double Network Hydrogel", *ACS NANO*, **11**, 12103-12110 (2017)
4. Kazuki Fukao, Kazuki Tanaka, Ryuji Kiyama, Takayuki Nonoyama and Jian Ping Gong: "Hydrogels toughened by biominerals providing energy-dissipative sacrificial bonds" , *Journal of Materials Chemistry B*, **8**, 5184-5188 (2020)

5. Honglei Guo, Yuto Uehara, Takahiro Matsuda, Ryuji Kiyama, Long Li, Jamil Ahmed, Yoshinori Katsuyama, Takayuki Nonoyama and Takayuki Kurokawa: "Surface charge dominated protein absorption on hydrogels", *Soft matter*, **16**, 1897–1907 (2020)
  
6. Tomáš Sedláčik, Takayuki Nonoyama, Honglei Guo, Ryuji Kiyama, Tasuku Nakajima, Yoshihiro Takeda, Takayuki Kurokawa, and Jian Ping Gong: "Preparation of Tough Double- and Triple-Network Supermacroporous Hydrogels through Repeated Cryogelation" , *Chemistry of Materials*, **32**, 8576-8586 (2020)
  
7. Chung-Yuen Hui<sup>1</sup>, Zezhou Liu, Nicolas Bain, Anand Jagota, Eric R. Dufresne, Robert W. Style, Ryuji Kiyama and Jian Ping Gong: "How surface stress transforms surface profiles and adhesion of rough elastic bodies" , *Proc. R. Soc. A*, **476**, 20200477 (2020)
  
8. Takayuki Nonoyama, Lei Wang, Masumi Tsuda, Yuki Suzuki, Ryuji Kiyama, Kazunori Yasuda, Shinya Tanaka, Kousuke Nagata, Ryosuke Fujita, Naoya Sakamoto, Noriyuki Kawasaki, Hisayoshi Yurimoto, and Jian Ping Gong: "Isotope Microscopic Observation of Osteogenesis Process Forming Robust Bonding of Double Network Hydrogel to Bone" , *Adv. Healthcare*



*Mater.*, **10**, 2001731 (2021)

9. Zezhou Liu, Chung-Yuen Hui, Anand Jagota, Jian Ping Gong and Ryuji Kiyama: “A surface flattening method for characterizing the surface stress, drained Poisson’s ratio and diffusivity of poroelastic gels” , *Soft Matter*, **17**, 7332-7340 (2021)
  
10. Takayuki NONOYAMA, Lei WANG, Ryuji KIYAMA, Naohiro KASHIMURA, Kazunori YASUDA, Shinya TANAKA, Takayuki KUROKAWA and Jian Ping GONG: “Fast in vivo fixation of double network hydrogel to bone by monetite surface hybridization”, *Journal of the Ceramic Society of Japan*, **129**, 584-589 (2021)
  
11. Yong Zheng, Ryuji Kiyama, Takahiro Matsuda, Kunpeng Cui, Xueyu Li, Wei Cui, Yunzhou Guo, Tasuku Nakajima, Takayuki Kurokawa, and Jian Ping Gong: “Nanophase Separation in Immiscible Double Network Elastomers Induces Synergetic Strengthening, Toughening, and Fatigue Resistance”, *Chemistry of Materials*, **33**, 3321-3334 (2021)

### 7.3 Presentation in scientific meetings

1. **Ryuji Kiyama**, Takayuki NONOYAMA, Tasuku NAKAJIMA, Takayuki KUROKAWA, JianPing GONG: “Selective HAp patterning of DN gel surface for osteoconduction”, The Ceramic Society of Japan The 29th Fall Meeting (September, 2016, Hiroshima) (**Best poster presentation award**)
2. **Kiyama Ryuji**, Nonoyama Takayuki, Wada Susumu, Kitamura Nobuto, KUROKAWA Takayuki, Nakajima Tasuku, Yasuda Kazunori, Gong, Jian Ping: “*In vivo* osteoconductive property of HAp composite tough DN hydrogel”, Bioceramics 28 (October, 2016, US)
3. **Kiyama Ryuji**, Nonoyama Takayuki, Wada Susumu, Kitamura Nobuto, KUROKAWA Takayuki, Nakajima Tasuku, Yasuda Kazunori, Gong, Jian Ping: “HAp 複合化高強度 DN ハイドロゲルの骨伝導機構の解明”, 6<sup>th</sup> CSJ Chemistry Festa (November, 2016, Tokyo) (**Best poster presentation award**)
4. **Kiyama Ryuji**, Nonoyama Takayuki, Wada Susumu, Kitamura Nobuto, KUROKAWA Takayuki, Nakajima Tasuku, Yasuda Kazunori, Gong, Jian Ping: “Osteoconduction mechanism of HAp composite tough DN hydrogel”, 4<sup>th</sup> ILSS (November, 2016, Sapporo)

5. **Kiyama Ryuji**, Nonoyama Takayuki, Wada Susumu, Kitamura Nobuto, KUROKAWA Takayuki, Nakajima Tasuku, Yasuda Kazunori, Gong, Jian Ping: “In vivo osteoconductive property of HAp composite DN gel”, HU-YZU joint symposium (November, 2016, Sapporo)
  
6. **Kiyama Ryuji**, Nonoyama Takayuki, Wada Susumu, Kitamura Nobuto, KUROKAWA Takayuki, Nakajima Tasuku, Yasuda Kazunori, Gong, Jian Ping: “Investigation of bone bonding structure of osteoconductive HAp/DN gel”, Gel symposium (March, 2017, Chiba) (**Best poster presentation award**)
  
7. **R. Kiyama**, T. Nonoyama, T. Nakajima, T. Kurokawa, J.P. Gong: “Direct Observation of Hydrogel Polymer Network using TEM”, ImPACT symposium (August, 2017, Sapporo)
  
8. **R. Kiyama**, T. Nonoyama, T. Nakajima, T. Kurokawa, J.P. Gong: “TEM observation of single polymer strand of hydrogel”, 5<sup>th</sup> ILSS (November, 2017, Sapporo)
  
9. **R. Kiyama**, T. Nonoyama, T. Nakajima, T. Kurokawa, J.P. Gong: “Direct observation of

hydrogel nano-scale network structure”, 29<sup>th</sup> 高分子ゲル研究討論会 (January, 2018, Tokyo)

10. **R. Kiyama**, T. Nonoyama, T. Nakajima, T. Kurokawa, J.P. Gong: “Novel hydrogel polymer network staining method based on organic-inorganic composition”, The Ceramic Society of Japan Annual Meeting 2018 (March, 2018, Sendai)

11. **R. Kiyama**, T. Nonoyama, T. Nakajima, T. Kurokawa, J.P. Gong: “DIRECT OBSERVATION OF SINGLE POLYMER STRAND BASED ON DOUBLE NETWORK STRATEGY”, 82<sup>nd</sup> Prague Meeting on Macromolecules (June, 2018, Prague)  
**(Best poster presentation award)**

12. **R. Kiyama**, T. Nonoyama, T. Nakajima, T. Kurokawa, J.P. Gong: “TEM Observation of Nano-Scale Hydrogel Network Structure”, 4DMS Gel symposium (August, 2018, Yonezawa) **(Best poster presentation award)**

13. **R. Kiyama**, T. Nonoyama, T. Nakajima, T. Kurokawa, J.P. Gong: “Surface structure of hydrogel measured by novel polymer network direct observation method”, 67<sup>th</sup>

Symposium on Macromolecules (September, 2018, Sapporo)

14. **R. Kiyama**, T. Nonoyama, T. Nakajima, T. Kurokawa, J.P. Gong: “Fractography of DN hydrogels”, ImPACT Young researchers meeting (October, 2018, Kobe)
15. **R. Kiyama**, T. Nonoyama, T. Nakajima, T. Kurokawa, J.P. Gong: “Direct observation of nano-scale hydrogel network”, 6<sup>th</sup> ILSS (November, 2018, Sapporo)
16. **R. Kiyama**, T. Nonoyama, T. Nakajima, T. Kurokawa, J.P. Gong: “Nano Scale TEM Observation of Hydrogel Surface”, 28<sup>th</sup> MRSJ (December, 2018, Fukuoka)
17. **R. Kiyama**, T. Nonoyama, T. Nakajima, T. Kurokawa, J.P. Gong: “ハイドロゲル網目直接観察法の開発”, TEIJIN Forum 2019 (February, 2019, Tokyo) (**Best poster presentation award**)
18. **R. Kiyama**, T. Nonoyama, T. Nakajima, T. Kurokawa, J.P. Gong: “Direct observation of hydrogel network”, 68th Symposium on Macromolecules (September, 2019, Fukui)
19. **R. Kiyama**, T. Nonoyama, J.P. Gong: “Hydrogel templated mineralization for nano

scale TEM observation of hydrogel network”, The 13<sup>th</sup> Pacific Rim (October, 2019, Okinawa)

20. **R. Kiyama**, T. Nonoyama, T. Nakajima, T. Kurokawa, J.P. Gong: “Novel hydrogel/mineral composite material for visualizing hydrogel network”, Gordon conference (January, 2020, US)

21. **R. Kiyama**, T. Nonoyama, Daniel R. King, J.P. Gong: “Mirror radius and fracture stress relation on DN hydrogel”, 69<sup>th</sup> Annual Meeting on Macromolecules (May, 2020, Fukuoka)

22. **R. Kiyama**, T. Nonoyama, Daniel R. King, J.P. Gong: “Fracture mirror radius of highly stretchable hydrogel”, 70<sup>th</sup> Annual Meeting on Macromolecules (May, 2020, Online)

## Acknowledgement

Firstly, I would like to say a big thank you to my supervisor, **Professor Jian Ping Gong**. She is really grateful to me for always being interested and listening to me when I started something new. I often come up with new experiments, and every time she said “it is interesting!!” It always motivated me. I also respect her friendly character. She always take care each student.

I also greatly thanks to **Associate Professor Takayuki Nonoyama**. He taught me everything about study including experiment, paper, how to enjoy sightseeing in between conference schedule. Also, I really like his fair personality. By the way, congratulations on your marriage. Be happy with your new family.

**Professor Takayuki Kurokawa** has been kindly gave me advices since I was bachelor student and member of the group meeting of the Biology Group. He always thinks about research deeply. I respect his thoughtfulness.

**Associate Professor Tasuku Nakajima** not only discuss about research with me, but also enjoy playing board games in the luncheon time. I was very much looking forward to those times, but

recently he spend almost all time with his family. I really want to play again.

I feel like **Assistant Professor Daniel R. King** is a friend in same age. I remember he first came to Japan as PhD student when I am bachelor student. Even now, I always enjoy funny talk with him. I also respect his talent on research. His comment is always essential, and he can find interesting phenomenon from any boring presentation.

Many thanks also to **assistant Professor Tao Lin Sun, assistant Professor Kunpeng CUI, assistant Professor Tsutomu INDEI, and assistant Professor Hailong FAN** for their help.

I am grateful to research assistants and staffs, **Yukiko Hane, Yoshinori Katsuyama, Miyuki Matsumoto, Miku Matsushita, Eiko Hasegawa, Saeko Iseya, Yuki Ookubo, and Yuri Kamada.** They helped my experiments and paperwork.

I learn a lot about study and daily life from senior students, especially **Mr. Riku Takahashi, Mr. Takahiro Matsuda, and Mr. Shunsuke Otake.** Thank you. I learned very little about research from **Mr. Yuki Shibata,** but he is my Smash Bros. teacher.



I greatly appreciate international students and Japanese junior students for studying and playing with me. Especially, I would like to thanks to **Kazuki Fukao, Masahiro Yoshida** for their support in my study.

I want to acknowledge the JSPS providing me Research Fellowships for Young Scientists, and Ambitious Leader's program. Their financial support encouraged me to go PhD course, and their program broadened my horizons.

Of course, I am most grateful to my family, they always support my life.

Finally, once again thank all the members of LSW. Thanks to their cooperation, my six years have been wonderful.

*Ryuji Kiyama*

Laboratory of Soft & Wet Matter

Graduate School of Life Science

Hokkaido University

Sapporo, Japan

March, 2022